NATIONAL INSTITUTE FOR FUSION SCIENCE

Conceptual Design of a Heavy Ion Inertial Fusion Reactor Based on Circular Induction Accelerators

Edited by Jun Hasegawa and Tetsuo Ozaki

(Received - Mar. 26, 2024)

NIFS-PROC-127

May. 29, 2024

Conceptual Design of a Heavy Ion Inertial Fusion Reactor Based on Circular Induction Accelerators

Edited by Jun Hasegawa and Tetsuo Ozaki

March 11, 2023
National Institute for Fusion Science
Toki, Gifu, Japan

ABSTRACT

This is a compilation of papers presented at the symposium "Conceptual Design of Heavy Ion Inertial Fusion Reactor Based on Circular Induction Accelerators" held online on March 11, 2023, supported by the National Institute for Fusion Science.

Keywords

heavy-ion inertial fusion, driver accelerator, induction synchrotron, direct-drive scheme, driver efficiency, target gain, illumination nonuniformity, massive beams, reactor recovery, liquid wall, dry wall, particle management, active evacuation, laser ion source, laser ablation, beam loss, charge exchange, ion impact ionization, blanket, liquid loop, vacuum vessel, exhaust system, target manufacturing, target injection, final focus, steam cycle, intermediate heat exchanger, facility, maintenance, fuel pellet material, expansion dynamics, free–molecular flow, reactor radius, pumping speed, heavy-ion beam transport, residual gas pressure, fast ignition, electron/ion energy spectrometer, hot electron polystyrene deuteride shell target

Preface

The symposium entitled “Conceptual Design of Heavy Ion Inertial Fusion Reactor Based on Circular Induction Accelerators” was organized as a part of the General Collaborative Research of National Institute for Fusion Science (NIFS) and held online on March 11, 2023.

In the symposium, 12 papers were presented, of which 11 papers are reported in this proceeding. The total number of participants was 18 including researchers from universities and research institutes.

The purpose of this symposium was to share the results of the engineering feasibility study of a heavy-ion inertial confinement fusion reactor based on circular induction accelerators, which has been conducted by a group of volunteers over the past several years, with researchers in related fields, and to identify issues to be solved to realize a fusion reactor based on this new accelerator technology.

We would like to express our sincere thanks to all of the participants, the authors and the staff of NIFS.

Jun Hasegawa
Tokyo Institute of Technology

Tetsuo Ozaki
National Institute for Fusion Science

Contents

List of Participants

Takuya Goto	(National Institute for Fusion Science)
Jun Hasegawa	(Tokyo Institute of Technology)
Kazuhiko Horioka	(Tokyo Institute of Technology)
Weihua Jiang	(Nagaoka University of Technology)
Yoshihiro Kajimura	(National Institute of Technology, Akashi College)
Takashi Kikuchi	(Nagaoka University of Technology)
Mayuko Koga	(University of Hyogo)
Kotaro Kondo	(National Institutes for Quantum Science and Technology)
Yoshitaka Mori	(The Graduate School for the Creation of New Photonics Industries)
Sadatsugu Muto	(National Institute for Fusion Science)
Makoto Nakamura	(National Institute of Technology, Kushiro College)
Yoshiyuki Oguri	(Tokyo Institute of Technology)
Tetsuo Ozaki	(National Institute for Fusion Science)
Toru Sasaki	(Nagaoka University of Technology)
Kazumasa Takahashi	(Nagaoka University of Technology)
Fumihiro Tamura	(National Institute of Technology, Nagaoka College)
Yuki Uchida	(National Institute of Technology, Nagaoka College)
Yosuke Yuri	(National Institutes for Quantum Science and Technology)

Direct Fast Ignition Experiment in Gekko XII-LFEX Laser

Tetsuo Ozaki

Laser Group, National Institute for Fusion Science, Japan

Abstract— **Polystyrene deuteride shell targets with two holes were imploded by the Gekko XII laser and additionally heated by the LFEX laser in a direct fast ignition experiment. In general, when an ultra-intense laser is injected into a blow-off plasma created by the imploding laser, electrons are generated far from the target core and the energies of electrons increase because the electron acceleration distance has been extended. The blow-off plasma moves not only to the vertical direction but to the lateral direction against the target surface. In a shell target with holes, a lower effective electron temperature can be realized by reducing the inflow of the implosion plasma onto the LFEX path, and high coupling efficiency can be expected. The energies of hot electrons and ions absorbed into the target core were calculated from the energy spectra using three electron energy spectrometers and a neutron time-of-flight measurement system, Mandala. The ions have a large contribution of 74% (electron heating of 5.5 J and ion heating of 8.4 J) to target heating in direct fast ignition.**

Keywords—fast ignition, electron/ion energy spectrometer, hot electron, ion, neutron, polystyrene deuteride shell target

I. Introduction

Fast ignition[1] has been performed by additionally heating an imploded core using an ultra-intense laser. It produces a relativistic electron beam. The core is additionally heated by three mechanisms, electron/ion drag heating, Joule heating by the return current and diffusive heating from the laser-plasma interaction region. Electron/ion drag heating is the most essential mechanism. At an early stage, the heating laser had been injected directly on the imploded core. In general, when an ultra-intense laser is injected into a blow-off plasma, electrons are generated far from the target core and the energies of electrons increase. It was found that dense blow-off plasma disturbed the penetration of the heating laser and sufficient energy coupling efficiency could not be obtained. Therefore, the current mainstream in fast ignition[2,3] is to attach a cone along the path of the heating laser to prevent the invasion of the blow-off plasma. However, it is difficult to accept a target with a cone in a future fusion reactor because this target is very complicated. For this reason, research into direct fast ignition[4-6] has also been continued.

The hot electron effective temperature (T_{eff}) should be maintained lower in order to obtain the high coupling efficiency because the ratio of the deposited energy to the electron energy into the core becomes large at lower T_{eff}. Here, the T_{eff}, which is evaluated by the slope of the energy spectrum, is equivalent to the average electron energy if the Maxwellian distribution of the electron energy spectrum is assumed. If the laser energy is the same, the lower T_{eff} means that larger numbers of electrons are generated. In order to achieve the lower T_{eff}, the pre-formed plasma before the main pulse of the heating laser on the laser path should be suppressed. One of the pre-formed plasmas is the blow-off from the imploding plasma. Another is created by the pre-pulse of the heating laser itself. An electron acceleration takes place around the critical density region in those pre-formed plasmas. If the scale length of the pre-formed plasma is long, the T_{eff} becomes high. The distance between the laser plasma interaction and the core is also important. In general, hot electrons have a divergence angle. When the distance is large, the irradiation efficiency of the electrons against the core decreases.

Direct fast ignition had not been adopted because the blow-off from imploding plasma is unavoidable. However, this problem may be reduced by using a target with holes[7] along the heating laser path. The shell target is cylindrically imploded, and a heating laser is injected at the implosion timing. Since the amount of blow-off plasma is small on the heating laser path, the electron acceleration will be decreased, and the position of the laser plasma interaction can be close to the core. Therefore, high irradiation efficiency can be expected. The holes may be able to reduce pre-pulse of the heating laser. If the main pulse is adjusted to the maximum compression timing of the imploding core, the pre-pulse can pass through the holes and omit the pre-formed plasma by the pre-pulse. Therefore, the laser energy can be effectively injected even by the heating laser with a poor contrast. For those reasons, the shell with holes has the conditions for lower T_{eff}.

In direct heating, ion heating cannot be ignored. In an intense laser, the ponderomotive acceleration (and/or Coulomb explosion) and target normal surface acceleration (TNSA)-like, are occurred. We use the expression "TNSA-like" here because the target surface is covered with plasma (not vacuum). But it can be regarded as TNSA as a whole. Here, we call TNSA "TNSA-like" because it is accelerated by the sheath electric field created by hot electrons. The ponderomotive acceleration etc. seems to contribute to the core heating because many ions are oriented to the laser direction. On the other hand, TNSA-like acceleration is mechanism with the target behind it. Therefore, the contribution of the core heating is considered to be small.

The electron-ion energy spectrometer (ESM)[8] and the Mandala neutron time-of-flight analyzer (Mandala)[9] are used to estimate the deposited energy of electrons and ions, which contribute to the heating. The results are compared with the absorbed energy obtained from areal density (ρR) and X-ray measurement[10]. The details of the diagnostics are explained in section 2.

Here, we focus on the results of transverse irradiation[11] by adding the simulation results. The details of the simulation are explained in section 3.1.

II. Experimental Setup

The experiment was performed using the Gekko XII (GXII)-LFEX[12] facility in the Institute of Laser Engineering of Osaka University. The GXII (wavelength of 0.53 μm) and the LFEX (1.054 μm) were used for target implosion and for additional heating, respectively. As a target, spherical shells of deuterium polystyrene, which have a diameter of 500 μm in diameter and a thickness of 7 μm were used. There are two holes of 100 μm in diameter in this target at a position 180 degrees apart. The LFEX is injected along a line connecting the centers of two holes. Cylindrical implosion is performed using six beams (named each as B04, 07, 09, 10, 11 and 12) in twelve beams, which are almost perpendicular in direction against the LFEX beam (transverse irradiation). FIGs. 1(a), (i)/(iii) and (ii)/(iv) show the irradiation arrangement of the GXII seen from the LFEX axis, and the irradiation coordination seen from the side, respectively. Three beams are irradiated to the target at equal intervals, as seen from the LFEX direction. The remaining three beams are irradiated from the counter side of the LFEX. The angle between the GXII and LFEX is 79.2 degrees in the transverse irradiation. The blow-off plasma is sufficiently far from the LFEX axis. Since there are holes on the LFEX axis, the ablation plasma is further reduced.

In the experiment, three different injection timings of the implosion laser and the heating laser were chosen. The energy of the implosion laser was (246-301) J×6 beams = 1.545-1.738 kJ with 1.1-1.3 ns with Gaussian shape. The LFEX laser consisted of two rectangular beams with 1-1.8 ps, about (202-287)×2 beams×60% (irradiation efficiency) =243-343 J on target. 60% means the efficiency through the optical components after the last monitoring system[13]. The focus diameter was estimated to be 50 μm in diameter. The irradiation intensity was over 10^{19} W/cm^2, which was in the relativistic region. Therefore, the generation of the energetic electrons and ions could be expected. For comparison, another experiment was also conducted in which the GXII was irradiated in a parallel direction to the LFEX (axial irradiation, B01, 02, 08, 03, 05, 06). The arrangement is shown in FIGs. 1(a)(iii) and (iv). The angle between GXII and LFEX is 37.4 degrees. In this arrangement, the ablation plasma invades easily in the cone angle of the LFEX beam. FIGs. 1(b) and (c) are the arrangements of the diagnostics and the target, respectively.

The behaviors of hot electrons and ions are measured using the ESM and Mandala. Three ESMs are installed at 0 degrees, 21 degrees, and 70 degrees from the LFEX forward direction. Electrons measured by the ESM are those that can be emitted by shaking off the potential near the target. Electrons with energies below this potential are not observed by the ESM. Therefore, the amount of particles observed by it is much smaller than that of generated particles. The electron energy distribution is observed with the shape unchanged and shifted by the potential. Assuming Maxwell distribution, the T_{eff} will be the average energy if the T_{eff} = the slope of the distribution is known. The installation position is on the chamber 0.89 m from the target. ESMs can measure hot electrons (measurable energy range: 0.5 MeV to 120 MeV) and protons (up to 7 MeV) or deuterium ions (up to 3.5 MeV), at the same time, by using a permanent magnet. The ESM has a very low leakage magnetic field because the magnetic circuit is suitably designed. Therefore, a large energy dynamic range can be achieved. Unfortunately, there is no ability to distinguish ion species. However, we can estimate the proton/deuteron ratio roughly by using the aluminum filter method[14].

The Mandala is located on 13.55 m from the target at 125.3 degrees from the LFEX forward direction. The Mandala consists of an array of 600 photomultipliers. The energies of neutrons can be obtained from the flight times. For the DD reaction between the deuterium target and the deuteron beam generated by the LFEX laser acceleration, backscattered neutrons with mainly lower than 2.45 MeV are measured. The advantage of the Mandala is that it can accurately observe the spectrum of neutrons of 10^6, even in a strong gamma ray environment during LFEX operation. In addition, CR-39 was used to measure ρR at implosion shots without the LFEX injection. ρR can be estimated by the energy loss of knock-on protons between the target and thermal DD neutrons. The X-rays come.

III. Experimental Results

The energy spectra of electrons and ions can be obtained from ESMs. In the experiment, the GXII irradiates to the target and the LFEX is injected into the core at two different timings. Electron and ion drag heatings are evaluated from their energy spectra and neutron results. FIG. 2(a) shows the pulse waveform of the GXII and T_{eff}. FIG. 2(b) shows the soft X-ray generation time history[15] from the imploding plasma obtained by the simulation (STAR2D[16,17]) and the injection timing of the LFEX. The peak time of soft X-rays seems to be the maximum compression time. A total of three shots were conducted. The LFEX was incident 200 ps before (twice) and 300 ps after the maximum compression time.

A. Electron

FIG. 3(a) shows a comparison of typical electron energy spectra measured in the counter direction of the LFEX for transverse and axial irradiations. The T_{eff} in transverse irradiation is clearly lower than that in axial irradiation because the blow-off from the imploding plasma is smaller in the former than in the latter. In transverse irradiation, it is difficult that the GXII irradiates the shell near the LFEX axis, and there is no ablation plasma because there are holes. Furthermore, the pre-pulse has passed during implosion through the holes in the imploding shell. The LFEX irradiates the core if we can adjust its injection timing to the maximum compression timing. The only wraparound of the explosive plasma from its surroundings blocks the LFEX path in transverse irradiation. Therefore, the T_{eff} remains low in transverse irradiation.

Rough spatial distributions of hot electrons can be obtained from the three ESMs. Comparisons of the spatial distribution of the electron spectra in transverse and axial irradiations have been performed. FIGS. 3(b) and (c) show those contour plots. In axial irradiation, electrons with a high T_{eff} at 0 degrees are observed, whereas in transverse irradiation, the T_{eff} remains low at 0 degrees. The low T_{eff} is convenient for fast ignition. It should be noted here that the absolute value of the number of electrons measured by the ESM is not proportional to the number of generated electrons. Since the electrons generated around the target are suppressed by the self-electromagnetic field and do not reach the position of ESM, the number of particles observed by it depends on the T_{eff}. Therefore, we focus more on the spectral shape than on the absolute amount of the signal.

In FIG. 4, the simulation results of the core plasma behavior at −200 ps (FIG. 4(a)) and +300 ps (FIG. 4(b)) are also plotted. Implosion characteristics were investigated using the 2D radiation-hydrodynamic simulation code STAR2D in a cylindrical coordinate. 3D distribution of the laser intensity was averaged around the symmetrical axis, and converted to 2D distribution. The simulation was conducted for a cylindrical geometry. It was originally developed for modeling extreme ultraviolet light source plasmas. We deal with laser-produced plasmas by solving propagation by laser ray-tracing, laser absorption by inverse bremsstrahlung, heat conduction, radiation transport, and temperature relaxation between ions and electrons. The sound velocity is calculated from the equation of state, and the flow velocity is calculated using the fluid solver HLLC (Harten-Lax-van Leer contact wave) [18] method, based on the sound velocity. The radiation transport was solved by a multi-group diffusion model with 40 groups, in which the maximum photon energy was 8 keV. The electron and ion heat conduction were calculated based on the flux limited Spitzer-Harm model[19] with a flux-limiter of 0.1.

The hot electron generation point is the interaction region between the LFEX laser and the ablation plasma. Ideally, the generation point should be close to the core, but according to computer simulation, the blow-off plasma partially invades the LFEX path at this timing, even in transverse irradiation. It can be that the electrons of the solid angle Ω, that see the target from the generation point, hit the target. Even the laser intensity is in the relativistic region, and there are primary interaction regions at 220 μm (−200 ps) and 240 μm (+300 ps) from the core center. Ωs are 4π×0.082 (−200ps) and 4π×0.017 (+300ps), respectively. Average T_{eff} ($=T_{eff\_ave}$) in which spatial uniformity is considered, are 1.06 MeV at −200 ps and 1.05 MeV at +300 ps, respectively. The reflection of the LFEX laser has been measured on a variety of targets in other experiment[20]. Many researchers have argued about the efficiency of laser-to-electron conversion. C.D. Chen[21] calculated the number of hot electrons passing through the target from the line intensity of Kα and estimates the conversion rate to be 20-40%. P.A. Norreys[22] showed that the energy coupling to the forward hot electron beam is in the range of 15-30%. The discussion here is not far from these results. The reflection mainly depends on laser intensity. The remaining 75% of the 25% of the laser reflection is assumed here to transfer energy to the electrons. Actually some energies are directly transferred to ions (ponderomotive acceleration etc.), but they are relatively small. Energies transferred to ions in TNSA and converted to electromagnetic waves such as X-rays are first transferred to electrons, and energies are transferred to ions and X-rays. The initial number of generated hot electrons can be obtained by dividing the un-reflected laser energy E_L by the T_{eff_ave}. There is also the energy that goes directly to ions, but we will discuss that in Sec. 3.2. It is estimated that 25% is reflected in this laser intensity region, and the remaining 75% is converted to electrons. The number of electrons, N_{elec_total}, can be estimated by

$$N_{elec\_total} = E_L \times 75\% \div T_{eff\_ave}. \quad (1)$$

Here we assume that the momentum is preserved.

$$(momentum\_of\_the\_light) \approx \int \{dN_{elec}(\Omega)/d\Omega\} p(\Omega)\, d\Omega + (ion\_contribution) + (reflection\_of\_the\_light), \quad (2)$$

where $p(\Omega)$ is the momentum vector $(|p(\Omega)| = m_e c \sqrt{(1+T_{eff}(\Omega)/m_e c^2)^2-1})$, c is the light velocity, me is the electron mass, respectively. Ponderomotive accelerated ions remain as the ion contribution in Eq. (2), although the ion distribution is almost uniform, as mentioned in Sec. 3.2. $N_{elec}(\Omega)$ becomes large in the direction of lower $T_{eff}(\Omega)$. $dN_{elec}/d\Omega$ is determined as satisfying $N_{elec\_total} = \int \{dN_{elec}/d\Omega\}\, d\Omega$. $4\pi\{dN_{elec}/d\Omega\}$ are plotted as a function of angle in FIG. 4.

The deposited energies of electrons to the target are almost the same as the stopping energy, $E_{\rho R}$, for the target's ρR, if the energies are higher than the $E_{\rho R}$. Total deposited electron energy becomes large if the number of electrons becomes large. ρR is 12.2 mg/cm^2 at the maximum compression by the recoil proton method using CR-39. We assume that the value has not changed significantly before and after the maximum compression. Therefore, the $E_{\rho R}$ is 0.0079 MeV. Bethe's classical formula is used about the value. Since the energy of the electron is so large, only the energy corresponding to the target, ρR, is lost. ρR is too small in this experiment. The value of the $E_{\rho R}$ is almost same if the electron energy is large compared to the range of ρR. The viewing areas $\omega/4\pi$ from the electron emission region are estimated to be 0.082 (−200 s) and 0.017 (+300 ps), respectively (FIG. 4). The total electron number which irradiates the target N_{elec_target} is $\{dN_{elec}/d\Omega\}\times\omega$. Therefore, total electron drag is $E_{\rho R} \times N_{elec\_target}$ are 5.5 J and 2.2 J at −200 ps and +300 ps, respectively.

B. Ions

The advantage of direct fast ignition is that the ions can be used for heating. Ion acceleration consists of ponderomotive acceleration etc.[23] and the TNSA-like type. These ions mainly contain deuterons and protons. Proton sources are water molecules adsorbed on the surface of the target. The ESM cannot distinguish particle species. Ponderomotive acceleration etc. is the main contributor to heating, but it is difficult to distinguish them by the ESM. FIG. 5 (a) shows typical ion spectra. Fig. 5(b) shows the contour plot of the ion spatial distribution. It can be seen that they are relatively isotropic. At early implosion time, holes of the shell are not completely closed yet. Also, even if the LFEX is injected at a late time of implosion, some ponderomotive accelerated ions can be observed by the ESM at 0 degrees because of an ion path through the gap of ablation plasma. However, the ion distribution seems to be uniform. Here we assume that the energy spectra of ponderomotive accelerated ions and TNSA-like ions are the same. Since the ion stopping range is short, it is assumed that each ion that collides with the high-density part of the target core gives all the energy.

The deposited energy of the ion heating can be estimated from neutron measurement. In nuclear fusion, it is generally produced by a thermonuclear reaction. However, in this experiment, beam fusion neutrons are overwhelmingly larger than thermonuclear neutrons. Here we consider ponderomotive acceleration etc. and TNSA as deuterium acceleration mechanisms. If deuterium is accelerated, it will hit the target deuterium and neutrons will be observed. Since TNSA is not oriented in the direction of the target, it is not a contribution of neutron generation because deuterium ions accelerated by TNSA do not collide with the deuteron in the target. Also, thermal neutrons are relatively small in proportion, so they are ignored here. The ponderomotive acceleration etc. is the main acceleration mechanism for deuterium (related to neutron generation). Ponderomotive acceleration etc. and TNSA assume that the deuterium ratio is the same here. From other experiments[14], the proportion of deuterium among the ions is about 80%, and the rest is primarily protons. Therefore, for ion heating, the value obtained from the neutron measurement caused by deuterium ions may be divided by 0.8. The amount of neutrons, Ny, is larger before the maximum compression than after it[23]. Other neutron sources such as $C(d,n)$, photo nuclear (γ,n) and (p,n) etc. can be negligible.

The number of D beams N_{Dbeam} is estimated by,

$$N_{Dbeam} = N_y / \{ \sigma_{DD} \times N_D \times l_{Range} \} \quad \propto 1 / \{ \rho \times l_{Range} \}, \tag{3}$$

where σ_{DD}, N_D, ρ and l_{Range} are the DD nuclear reaction cross-section, the number density of the deuterons in the target, the mass density, and the stopping range, respectively. The mass density at the maximum implosion time ρ_{max} can be estimated from $\rho_{max}R_{max}$, obtained by the CR-39 knock-on proton method and R_{max} obtained from the XPHC. Its value is 1.9 g/cm^3. The target radius R and ρ at −200 ps, are larger than R_{max} and smaller than ρ_{max} because the implosion is still continued, as shown in FIG. 3. ρ at −200 ps is estimated to be 1.67 g/cm^3.. However, the product of ρ and l_{Range} in Eq. (3) at −200 ps is only 5% different from that at the maximum implosion time. Therefore, $\rho_{max}R_{max}$, is adopted as ρl_{Range} at +300 ps because it is difficult to evaluate ρl_{Range} at +300 ps. The average energy of the ions, T_{ion}, can be estimated to be 0.46 MeV (−200 ps) and 0.33 MeV (+300 ps) by approximating the Maxwell distribution of the ion spectrum in FIG. 4(a). l_{Range} at T_{ion} can be calculated by using the SRIM[24] code (solid) and the range difference of 0.6 between solid and hot plasma. ls are 2.25 μm (−200 ps) and 1.38 μm (+300 ps).

σ_{DD} at T_{ion} can be obtained to be 0.1 b (−200 ps) and 0.076 b (+300 ps). On the other hand, N_y are 2.47×10^8 (−200 ps) and 0.268×10^8 (+300 ps) from the Mandala[25]. N_{Dbeam} can be calculated from Eq. (3). Since l_{Range} is too short compared to the target size, it is assumed that all the ion energies are deposited on the target. As the ratio of deuterium is 80% of the total ions, the number of all ions that irradiate the target can be calculated. Finally, the deposit energy $N_{Dbeam}\times T_{ion}$,÷0.8, can be estimated to be 8.5 J (−200 ps) and 1.2 J (+ 300 ps).

In this experiment, the injection timing of the LFEX was slightly early compared to the implosion timing, so that the ions were irradiated to a large target viewing angle, although the ion generation point was far from the core. Therefore, considerable neutrons were observed before the implosion than afterwards. It is important to increase the solid angle of irradiation by preventing the blow-off plasma and adjusting to the implosion timing.

IV. Discussion

The deposited energy by additional heating was evaluated from the ESM results for transverse irradiation. The T_{eff} is kept sufficiently low, and the difference between the three T_{eff} is simply proportional to the incident energy (intensity). In Sec. 3, the energy added by the LFEX energy of 343 J could be estimated to be 5.5 J for electrons and 8.5 J for ions. The ions have a large contribution against target heating in direct fast ignition. The results of the electron and ion heatings are listed in Tables I and II, respectively.

The electron and ion drags can be also estimated to be 2.3 J and 1.2 J by the same procedure in axial irradiation, respectively; then total amount is 3.5 J. On the other hand, we could succeed in estimating the increment of the internal energy of 6.7 J by using an optical technique in axial irradiation[26]. Those values are closed from each other.

If the internal energy of implosion without additional heating is to be 45 J, the same as that in axial irradiation and the increase of the internal energy is 13.9 J in transverse irradiation, the magnification of the internal energy is 1.28 times. Assuming that the ion temperature before the additional heating is 0.85 keV, the same as that in axial irradiation, it becomes 1.09 keV, which increases the nuclear reaction rate 4.1 times. However, since the amount of neutrons without additional heating is 3.47×10^6, it becomes only 1.44×10^7 by additional heating. Therefore, the thermal neutron signal could not be observed because it was hidden behind the beam neutron signal (2.47×10^8).

V. Summary

In order to increase the efficiency of the additional heat, it is important to close the laser plasma interaction region to the imploded core. According to the simulation, considerable blow-off plasma still invades to the LFEX path, even if in transverse irradiation. If we put a fin around the hole (see Fig 1(d)), the invasion of the blow-off can be suppressed considerably. According to another simulation, which imitates the configuration without invasion of the blow-off plasma, the laser plasma interaction region can be approached up to 110 μm from the center of the core. As a result, the solid angle of irradiation can be improved to be $4\pi\times0.5$, and a heating efficiency of 2.3 times can be expected, even if at current low ρR. Attaching the fin around the hole is simpler than attaching a conventional cone, and is realistic for a future fusion reactor.

Acknowledgements

This work is supported by NIFS14KUGK120, KUGK129, NIFS-URSX302, URSX305, IIHH001 and The Graduate School for the Creation of New Photonics Industries.

The author thanks Y. Abe, Y. Arikawa, Y. Sentoku, J. Kawanaka, S. Tokita, N. Miyanaga, T. Jitsuno, Y. Nakata, K. Tsbakimoto (Institute of Laser Engineering, Osaka Univ.), A. Sunahara (Purdue University), T. Jhozaki (Hiroshima Univ.), E. Miura (National Institute of Advanced Industrial Science and Technology), O. Komeda (Toyota Motor Corporation), A. Iwamoto, H. Sakagami (National Institute for Fusion Science), S. Okihara, K. Ishii, R. Hanayama, Y. Mori and Y. Kitagawa (The Graduate School for the Creation of New Photonics Industries).

References

[1] M. Tabak, *et al.*, Phys. Plasmas **1** (1994) 1626.

[2] R. Kodama, *et al*., Nature **418** (2002) 933.

[3] S. Sakata, *et al*., Nature Com.,**9** (2018) 3937.

[4] Y. Kitagawa, *et al*., Phys. Rev. E, **71** (2005) 016403.

[5] Y. Kitagawa, *et al*., Plasma Fus. Res., **6** (2011) 1306006.

[6] Y. Kitagawa, *et al*., Phys. Rev. Lett, **114** (2015) 195002.

[7]T. Ozaki, *et al.*, Physica Scripta **2014 T161** (2014) 014025.

[8] T. Ozaki, *et al*., Rev. of Sci. Instrum. **83** (2012) 10D920-1.

[9] Y. Abe, *et al.*, Rev. of Sci. Instrum. **89** (2018) 110I114.

[10] E. Miura, *et al.*, High Ene. Dens. Phys., **36** (2020) 100890.

[11] T. Ozaki, *et al*., Plasma and Fusion Res. **16** (2021) 2404076.

[12] H. Shiraga, *et al.*, Plasma Phys. Cont. Fus. **53** (2011) 124029.

[13] Y.Arikawa, private communication.

[14] T.Ozaki, *et al.*, Plasma and Fusion Res., **17** (2022) 2404084.

[15] T. Jhozaki, private communication.

[16] A. Sunahara, *et al.*, J. of Phys.**717(1)** (2016) 012055.

[17] A. Sunahara, *et al*., Plasma Fusion Res. **3** (2008) 043.

[18]K.F.Gurski, https://doi.org/10.1137/S1064827502407962.

[19] R.C. Malone, et al., Phys. Rev. Lett. **34** (1975) 721.

[20] T. Ozaki, *et al*., J. Phys. **717** (2016) 012043.

[21] C.D. Chen, *et al*., Phys. of Plasma, **16**（2009) 082705.

[22] P.A. Norreys, *et al*., Nucl. Fusion **49**（2009) 104023.

[23] N.M. Bulgakova, *et al.*, Applied Physics **A 81** (2005) 345.

[24] http://www.srim.org/

[25] Y. Abe, *et al*., High Ene. Dens. Phys., **36** (2020) 100803.

[26] Y. Kitagawa, *et al*., Rev Laser Eng., **49** (2021) 149 (in Japanese).

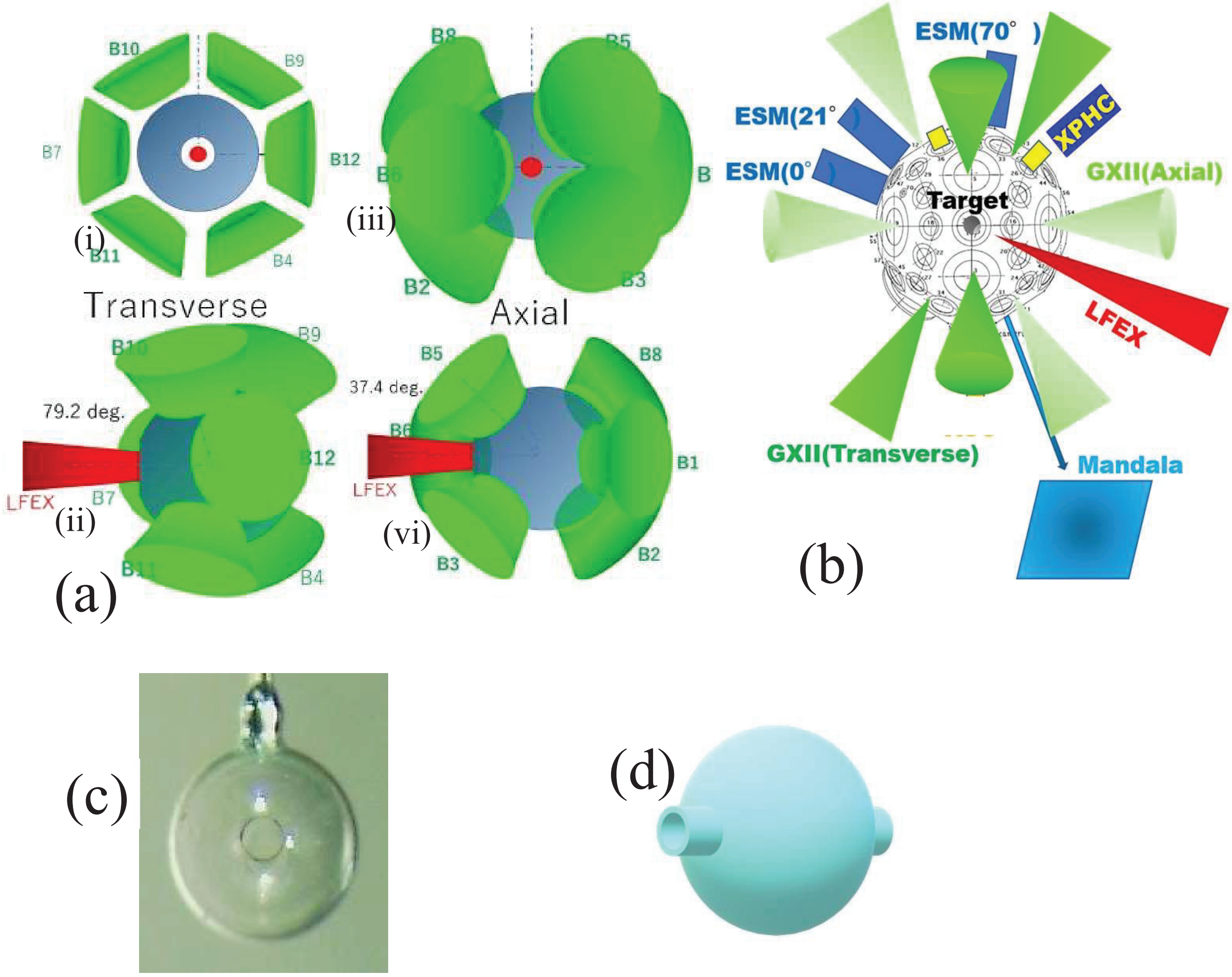

FIG. 1. Laser and diagnostics arrangements.

(a) The GXII (green) and LFEX (red) laser arrangements,

The GXII and the LFEX are used for compression and additional heating, respectively. B1, B2, B3 etc. (Dark green) means the names of the GXII beams. The GXII is tilted 79.2 degrees with respect to the LFEX for transverse irradiation, and 37.4 degrees for axial irradiation.

(i) and (ii) show sight and side views from the LFEX axis in transverse irradiation, respectively.

(iii) and (iv) show sight and side views from the LFEX axis in axial irradiation, respectively.

Polystyrene targets (blue) with and without holes are used in transverse and in axial irradiations, respectively.

(b) Diagnostics arrangements,

Three ESMs are installed at 0 and 21 and 70 degrees against the counter direction of the LFEX. XPHCs are installed at 125 and 70 degrees from the LFEX laser counter direction. The Mandala is located 13.55 m from the target at 125.3 degrees from the LFEX counter direction.

(c) Photograph of the target.

(d) Target with fins(ideal).

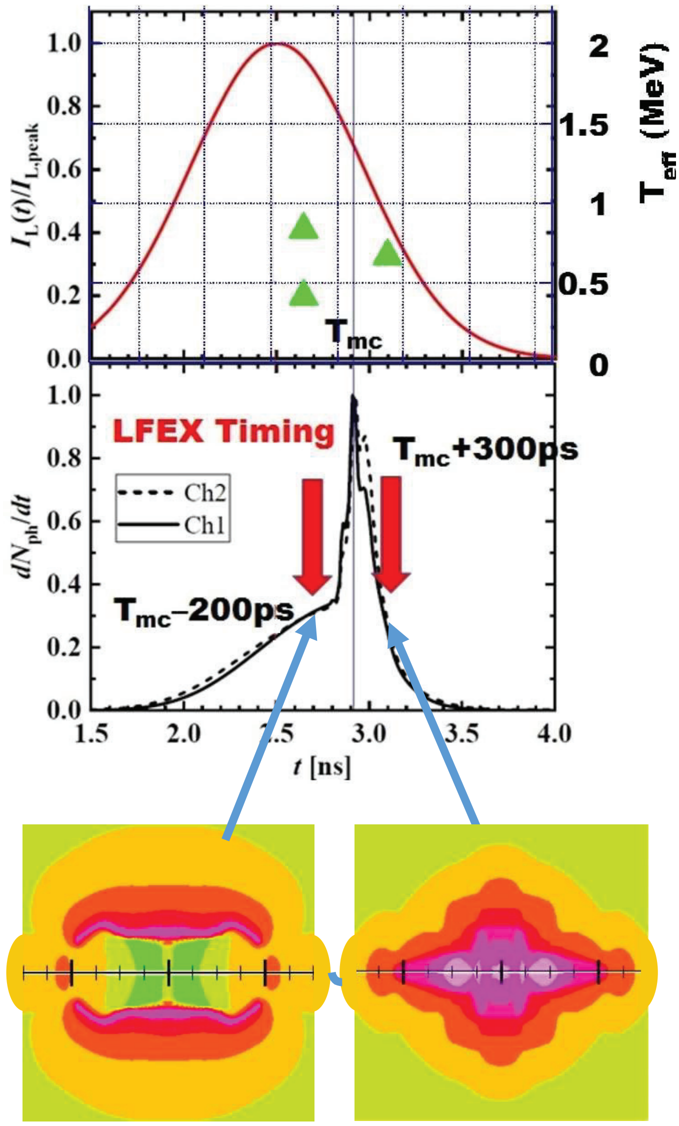

FIG.2. GXII waveform and LFEX injection timing.
The intensity waveform of GXII has a Gaussian profile with a pulse width of 1.1-1.3 ns. The beam energy is an average 250 J/beam. Teff is also plotted on the same figure. The LFEX injection timings are also shown in a lower figure.
(upper) The GXII waveform and the T_{eff} in a counter direction to the LFEX laser (green triangles).
Mainly hard X-rays are generated when hot electrons collide with targets and other structures. Error bars come from the comparison of two different ways of hard X-ray noise reduction. However, error bars are hidden in the symbols because they are within ±0.03 MeV.
(lower) X-ray emissions from the core in simulation.
The X-rays come from the imploded core. They show a comparison with laser injection timing. Red arrows show the LFEX injection timings. The photon energy range corresponds to an imaging plate (IP) used in the experiment. The signal is the integral of the sensitivity of the IP (400-800 nm). The unit of X-ray emission is the number of photons per second. It is normalized by the peak because an absolute value is not necessary here. T_{mc} means the maximum compression time. The details of the simulation are described in 3.1.

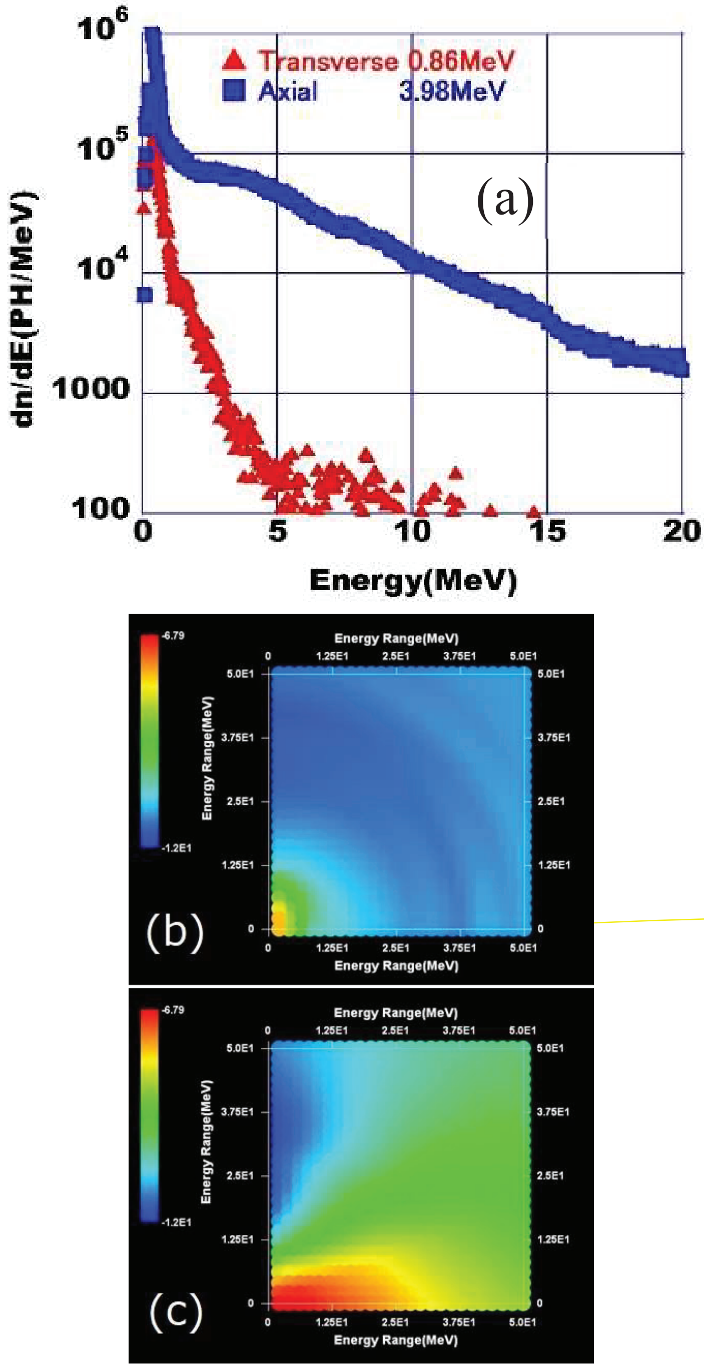

FIG.3. Electron energy spectra.
The spectra of hot electrons were compared under transverse and axial irradiation. Transverse irradiation is clearly optimal for fast ignition. An angular contour plot was prepared to express the spatial distribution of the spectrum. It can be seen that the transverse irradiation is almost isotropic.
(a) Comparison of electron spectra at 0 degree between in transverse and in axial irradiations.
T_{eff}s are written on the upper part of the graph,
(b) Contour plot in transverse irradiation,
(c) Contour plot in axial irradiation. In (b) and (c), it will be the same energy if concentric circles are drawn from the origin since it is a polar coordinate. Rotating the horizontal axis by θ around the origin, the electron energy spectrum at the observation direction θ can be obtained.
from the imploded core. X-ray pinhole cameras (XPHC) were used to measure the size of the core plasma.

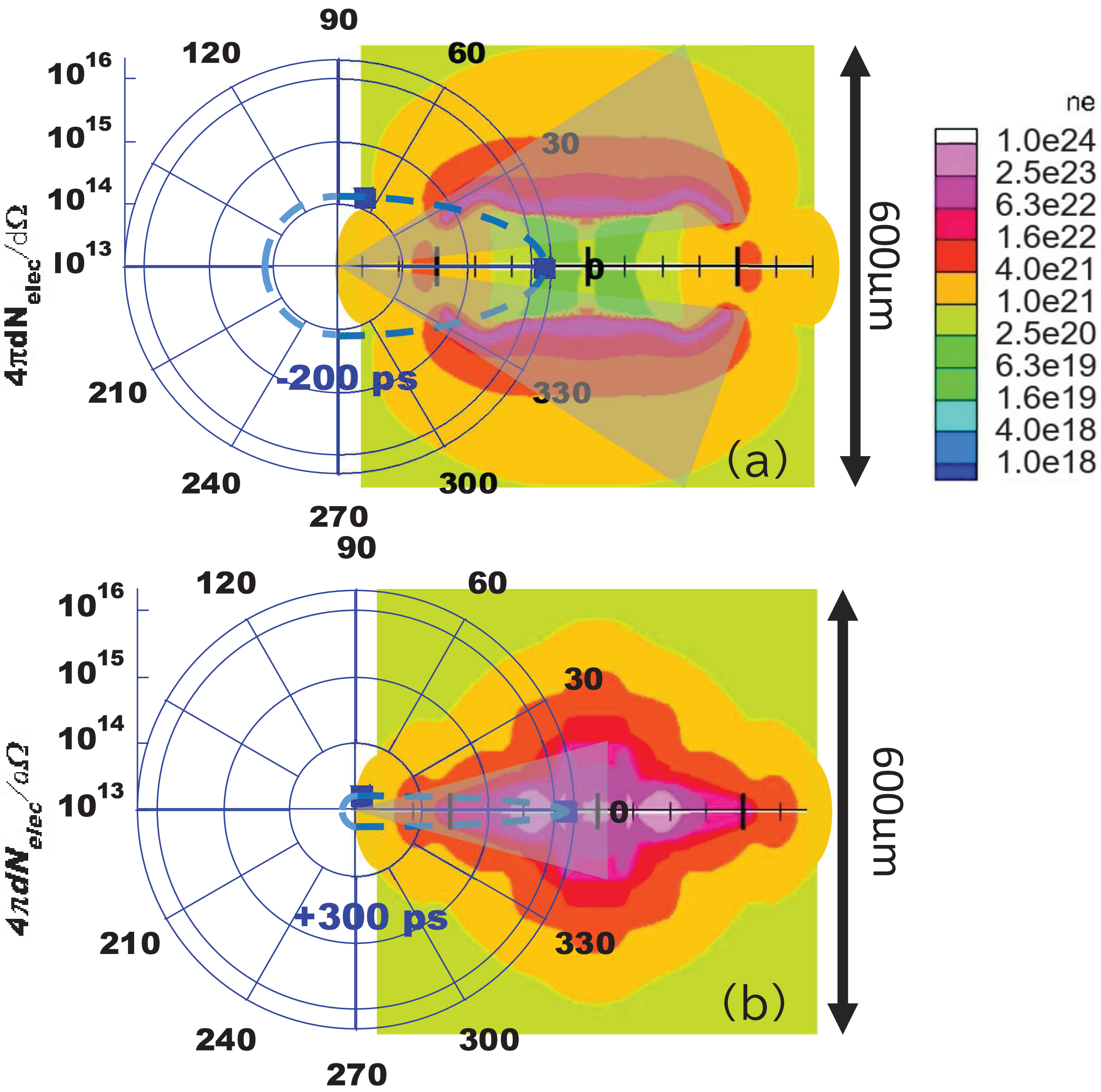

FIG.4. Comparison between simulation (density plot) and ESM results.
The color figures show the shape of the target obtained by simulation at the time of LFEX incidence.
(a) at −200 ps, (b) at +300 ps.
The electron number distributions in left circular plots are overlapped on the 2D simulation density plots in /cm^3. Broken lines and triangle shadows show the rough electron distribution and the electron trajectory which irradiates the targets. The angular distribution of hot electrons shown by the broken line is obtained as follows. This is the number of electrons per unit solid angle. First, the total number of electrons is obtained by dividing the total energy absorbed by the laser by the average electron energy (T_{eff}), The electrons are allocated by the solid angles so that the momentum (originally the momentum brought in by the laser) is preserved.

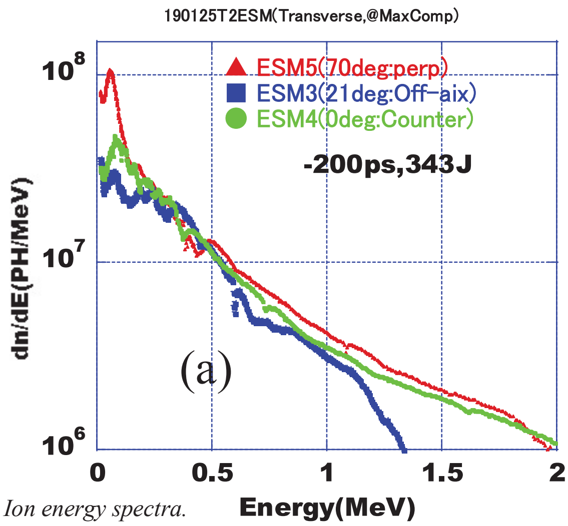

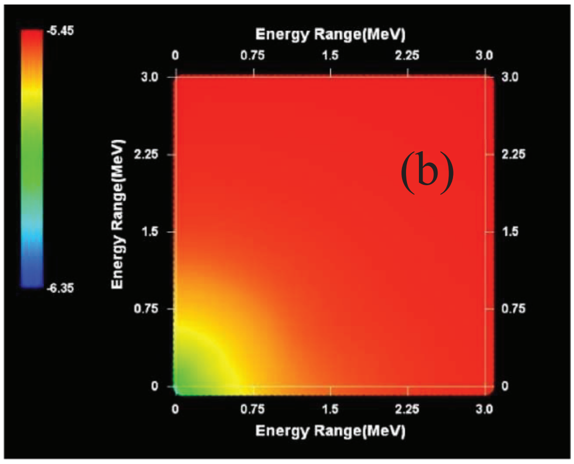

FIG.5. Ion energy spectra.

It can be seen that the ion spectrum in transverse irradiation is nearly isotropic.

(a) Ion spectra,

(b) Contour plot. It is a polar coordinate (contour) of the integrated energy of ions dissipated from the target (mainly TNSA). The z-axis (color) is a logarithmic scale. Since it is a polar coordinate, it will be the same energy if concentric circles are drawn from the origin.

Table I. Electron heating

Config.	Shot(19*)	Delay(ps)	E_L(J)	T_{eff_avg}(MeV)	$\omega/4\pi$	$E_{\rho R}$(MeV)	$N_{elec}(10^{15})$	E_{drag}(J)
Trans.	0125T2	−200	343	1.05	0.082	0.079	1.53	5.5
Trans.	0125T5	+300	309	1.06	0.017	0.079	1.37	2.2
Axial	0124T3	+200	262	2.06	0.413	0.096	0.60	2.3

Table II. Ion heating

Config.	Shot(19*)	ρR(g/cm^2)	l_{Range}(μm)	ρ(g/cm^3)	N_{Dbeam}	T_{ion}(MeV)	σ_{DD}(b)	$N_y/10^8$	E_{drag}(J)
Trans.	0125T2	0.0122	2.25	1.67	11.5×10^{13}	0.46	0.10	2.47	8.5
Trans.	0125T5	0.0122	1.38	1.90	1.64	0.33	0.076	0.268	1.2
Axial	0124T3	0.0160	1.28	2.86	2.35	0.44	0.107	0.397	2.0

Progress in Accelerator Technology and Heavy-Ion Inertial Fusion System Designs

Yoshiyuki Oguri

NAT Research Center, NAT Corporation,
3F, Hitachinaka Techno Center, 38 Shinkocho, Hitachinaka-Shi, Ibaraki, 312-0005, Japan

Kotaro Kondo

Kansai Institute for Photon Science, National Institutes for Quantum Science and Technology,
8-1-7 Umemidai, Kizugawa-Shi, Kyoto, 619-0215, Japan

ABSTRACT

The advantages of heavy-ion beams as a driver of inertial confinement fusion (ICF) are reviewed in terms of beam transport, energy deposition to the target, and driver efficiency in comparison with other types of beam drivers. A new conceptual design study of a direct-drive heavy-ion inertial fusion (HIF) plant based on the induction synchrotron technology is briefly introduced.

Keywords

accelerator, direct-drive scheme, driver efficiency, heavy-ion inertial fusion, induction synchrotron, target gain

1. Introduction

On December 5, 2022, the US National Ignition Facility (NIF) announced that an output fusion energy of 3.15 MJ was obtained for an input laser energy of 2.05 MJ [1], corresponding to a target gain G = 3.15 / 2.05 = 1.54. This result was widely publicized as one step closer to the practical use of nuclear fusion energy. In general, nuclear fusion is deemed meaningless as an energy source, unless the overall gain exceeds 1; however, the energy required to generate the laser energy of 2.05 MJ at NIF was more than 100 times the laser energy [2].

2. Energy Flow in ICF Plants

Figure 1 illustrates the energy flow in an inertial confinement fusion (ICF) plant. In this system, the time-averaged gross and net output electric power, denoted by $P_{\mathrm{e,gross}}$ and $P_{\mathrm{e,net}}$, respectively, are given by

$$P_{\mathrm{e,gross}} = \eta_{\mathrm{thermal}}(P_{\mathrm{fusion}} + P_{\mathrm{driver}}), \qquad (1)$$

$$P_{\mathrm{e,net}} = P_{\mathrm{e,gross}} - P_{\mathrm{input}} = P_{\mathrm{e,gross}} - \frac{P_{\mathrm{driver}}}{\eta_{\mathrm{driver}}}. \qquad (2)$$

In the above formulas, P_{fusion}, P_{input}, and P_{driver} are the time-averaged fusion output power, the input power to

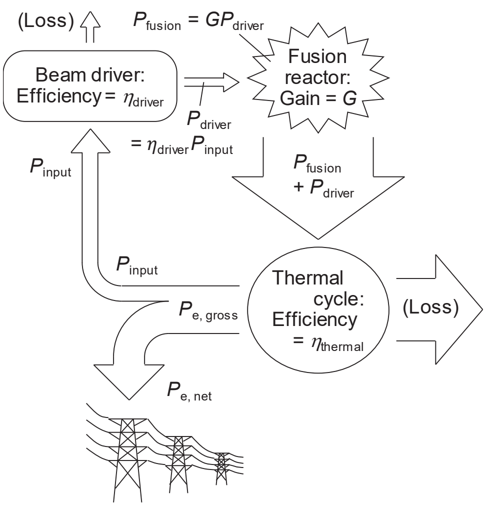

Fig. 1 General energy flow in an inertial confinement fusion plant

the driver, and the driver beam power to the target, respectively, η_{thermal} is the efficiency of the thermal cycle, and η_{driver} is the driver efficiency. Heavy-ion inertial fusion (HIF) uses beams of ions with a mass number >200 and a total kinetic energy around 10 GeV as drivers. Other beams, such as lasers, electron beams, and light-ion beams, have also been investigated as potential drivers. Table 1 lists the efficiencies of pulsed MJ lasers [2] and different types of high-intensity charged-particle accelerators [3–6]. It is shown that η_{driver} strongly depends on the type of the beam driver.

Table 1 η_{driver} of different beam drivers

Driver		η_{driver}
Pulsed MJ laser	Present [2]	0.5%
	Development goal [2]	20%
Electron accelerator	Electrostatic accelerator [3]	60%–80%
	Linac [4]	>50%
Ion accelerator	Electrostatic accelerator [5]	>30%
	Proton cyclotron [6]	≈50%

From the equations above, considering that $P_{\mathrm{fusion}} = GP_{\mathrm{driver}}$ and $P_{\mathrm{driver}} = \eta_{\mathrm{driver}} P_{\mathrm{input}}$, the overall plant efficiency η_{plant} can be calculated by the following equation:

$$\eta_{\mathrm{plant}} \equiv \frac{P_{\mathrm{e,net}}}{P_{\mathrm{fusion}}} = \eta_{\mathrm{thermal}}\left(1+\frac{1}{G}\right) - \frac{1}{\eta_{\mathrm{driver}} G}. \qquad (3)$$

When the target gain is very high, i.e., $G >> 1$, the equation above becomes

$$\eta_{\mathrm{plant}} \approx \eta_{\mathrm{thermal}}, \qquad (4)$$

suggesting that η_{plant} does not depend on the value of η_{driver} any more. This condition is a prerequisite for laser fusion, since η_{driver} of pulsed MJ lasers is so far very small, as shown in Table 1. However, the condition $G >> 1$ is not always easily attained, because G is extremely sensitive to the spherical symmetry of the target implosion [7].

Figure 2 shows the dependence of η_{plant} on η_{driver} for different G values, calculated using Eq. (3). For this calculation, we assumed $\eta_{\mathrm{thermal}} = 40\%$. From this figure, for example, if a value of $\eta_{\mathrm{driver}} = 50\%$ [6] is attained, a target gain $G = 27$ is enough to achieve η_{plant} comparable to that obtained by conventional light

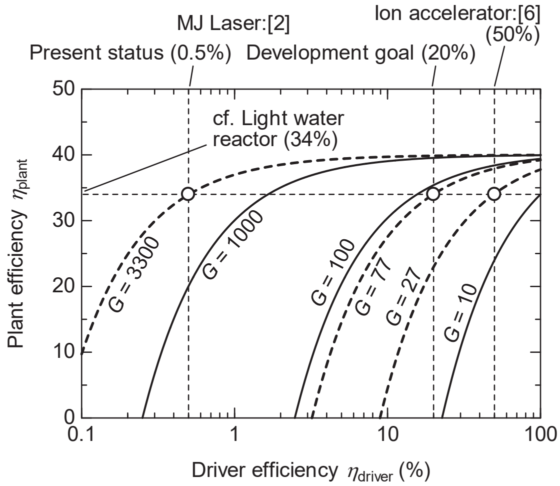

Fig. 2 Dependence of the η_{plant} on η_{driver} for various values of G calculated using Eq. (3)

water reactors [8]. Thus, G and the value of η_{driver} are both essential when designing a realistic inertial fusion plant. In this regard, charged-particle beams are promising as practical drivers because their efficiencies are significantly higher than those obtained by lasers, as shown in Table 1. In addition, particle accelerators can be operated with a repetition rate of ≈10 Hz, whereas existing pulsed MJ lasers can only be operated on a single-shot (≈10^{-4} Hz) basis [2].

3. Brief Review of HIF

3.1 Energy deposition of heavy ions in the target

Figure 3 illustrates the interactions between different driver beams and the target. A laser beam is an electromagnetic wave, which is strongly absorbed by the free electrons in the surface layer of the ionized target. In particular, the energy deposition profile becomes complicated due to selective absorption at the depth where the free electron density becomes critical [9], a value that is determined by the frequency of the light wave. Consequently, the energy transfer to the interior of the target is achieved by thermal conduction. Electrons are charged particles whose energy absorption is volumetric. However, their penetrating power and scattering in the target are both strong. As a result, the specific energy deposition density is small and the range is rather unclear.

In contrast, despite the fact that ions are also charged particles, their stopping power is much higher and

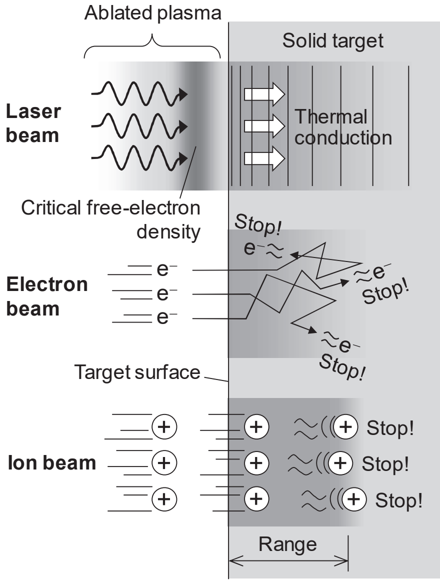

Fig. 3 Interactions between energy drivers and the target

their trajectories in the target are more linear and less scattered compared to those of electrons. Consequently, the specific energy deposition density is large, and the range distribution is well-defined. Compared to light ions, such as H to Li, this feature becomes more pronounced when very heavy ions, such as Pb and Bi, are used.

The fuel target implosion process in HIF is similar to that in ICF based on other drivers. However, a critical advantage of using HIF is that we can apply a thin outermost layer of heavy material ("tamper"), particularly when designing a spherical target for the "direct-drive" scheme [9], which is less mobile and retards the outward motion of ablator plasma.

3.2 Beam transport and focusing

Due to the space-charge repulsive forces between ions, beam divergence during acceleration and transport increases with increasing beam current. Therefore, beam current needs to be minimized. The total beam kinetic energy W imparted to the target is given by

$$W = EN \propto EI_{\mathrm{beam}}\Delta t, \tag{5}$$

where E, N, I_{beam}, and Δt denote the kinetic energy of a single ion, the number of the ions, beam current, and beam pulse duration, respectively. Eq. (5) suggests that the required I_{beam} can be reduced by increasing E. However, if E is too high, the beam can go through ablator layers with a thickness of less than 1 mm, reaching the fuel layer. In this case, undesired preheating of the fuel can occur. As a result, E cannot be increased indefinitely.

Table 2 compares the performances of light-ion and heavy-ion beams, taking the case of applying W = 1 MJ to the target during Δt = 10 ns, as an example. The calculated ranges [10] in an Al ablator are also listed. It is shown that the beam of high-energy heavy-ions, such as 10-GeV ^{209}Bi, is most suitable as an energy driver, because the required energy can be deposited solely to the required depth region with a minimal beam current.

Table 2 Performances of different driver beams when W = 1 MJ and Δt = 10 ns

<table>
<tr><th>Ion species</th><th>Beam energy E</th><th>Beam current I_{beam}</th><th>Range in Al[10]</th></tr>
<tr><td rowspan="2">^{1}H</td><td>9 MeV</td><td>11 MA ☹</td><td>0.5 mm ☺</td></tr>
<tr><td rowspan="3">10 GeV</td><td rowspan="3">10 kA ☺</td><td>21 m ☹</td></tr>
<tr><td>^{56}Fe</td><td>9 mm ☹</td></tr>
<tr><td>^{209}Bi</td><td>0.5 mm ☺</td></tr>
</table>

3.3 Existing HIF plant scenarios

Although HIF has excellent performance in principle, even a dedicated experimental plant has not yet been constructed in practice. The main reason is that an experimental plant can be unacceptably huge in size and significantly expensive. As a result, only a few engineering design studies have been conducted so far. Table 3 shows several specific design scenarios of HIF plants published in literature. In the 1980s, the beam driver designs were mainly based on extending existing high-energy RF (radio frequency) accelerator technologies for particle physics experiments. A simple direct-drive scheme was adopted for the fusion reactor, in which a large number of beams irradiated the target capsule as isotropically as possible from many directions [11–13]. Since the 1990s, induction linacs [14,15] have been introduced as a beam driver, especially in the US. In addition, the indirect drive scheme [9] was proposed to attain the required spherical implosion symmetry with a small number of

Table 3 Design scenarios of HIF plants published in current literature

Name	HIBALL [11]	HIBLIC [12]	HIBALL-II [13]	OSIRIS [14]	HYLIFE-II [15]	MIDF
Publication year	1981	1984	1985	1992	1994	2023
Country	Germany, USA	Japan	Germany, USA	USA	USA	Japan
Target drive scheme	Direct	Direct	Direct	Indirect	Indirect	Direct
Ion species	$^{209}Bi^{2+}$	$^{208}Pb^{+}$	$^{209}Bi^{+}$	$^{131}Xe^{+}$	$^{200}Hg^{+}$	$^{208}Pb^{+}$
Ion energy (GeV)	10	15	10	3.8	10	9
Driver efficiency	0.27	0.25	0.27	0.28	0.35	0.3
Number of reactor chambers	4	10	4	1	1	1
Number of beams*	20	6	20	12	12	100
Input energy to target* (MJ)	5	4	5	5	5	40
Repetition rate† (Hz)	5	1	5	4.6	6	1
Target gain	83	100	87	86.5	70	50
Electric power output (MW)	3768	1500	3784	1000	940	1000

*per target capsule, †per reactor chamber

beams. At the same time, numerical analysis methods on implosion hydrodynamics became more sophisticated. Nevertheless, no breakthrough design scenarios have been published since the 2000s.

4. Massive-Ion-Driven Fusion (MIDF)

In this symposium, we propose a novel conceptual design of a HIF system, “Massive-Ion-Driven Fusion (MIDF).” A schematic system layout and the reaction chamber with the driver beam lines are illustrated in Fig. 4. The main parameters are also included in Table 3. By making full use of the latest induction synchrotron technologies [16], functions, such as beam acceleration, storage, and compression, could be integrated into a stack of rings. Owing to this simplification, the number of beams impinging on one target capsule could be increased up to 100 at a moderate cost. This large number of beams allowed us to revisit the simple direct-drive scheme, where the energy efficiency is higher than that obtained by indirect drive systems. The large number of beams also enables a higher input energy (40 MJ) per target capsule, and therefore, higher output fusion energy per shot, although care must be taken for recovering the required vacuum conditions. In addition, taking the high sensitivity of G to the target implosion symmetry into account, a robust low-G design was employed. Details of this design study can be found in the articles of this symposium proceedings.

References

[1] https://www.llnl.gov/archive/news/lawrence-livermore-national-laboratory-achieves-fusion-ignition (2022).

[2] E.I. Moses, “Ignition and Inertial Confinement Fusion at the National Ignition Facility”, *J. Phys.: Conf. Ser.,* **244**, 012006 (2010).

[3] D. Darsono, “Application of Electron Accelerator for Flue Gas Treatment of Coal Power Plant to Support Green Technology”, *IOP Conf. Ser.: Earth Environ. Sci.,* **456**, 012002 (2020).

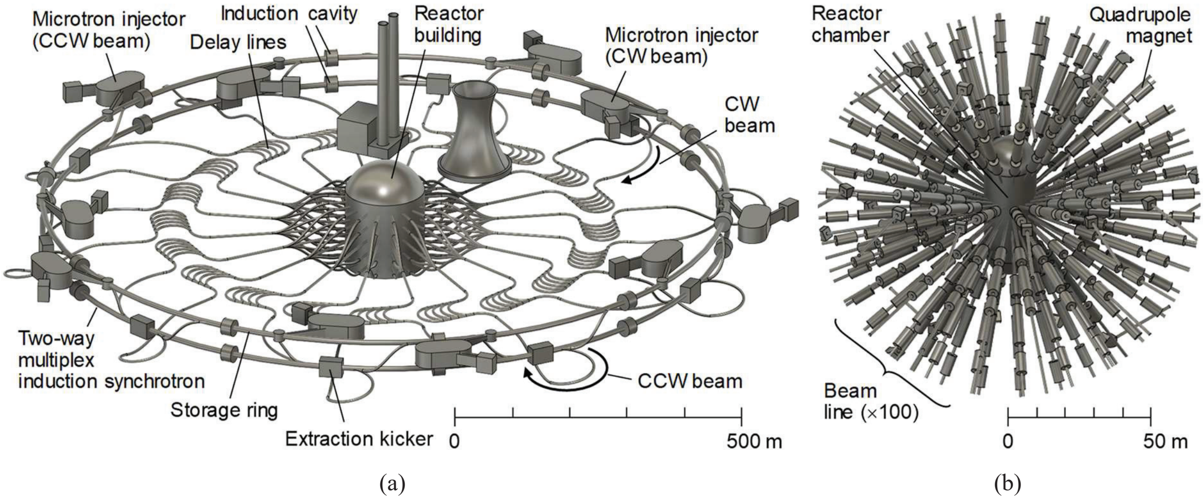

Fig. 4 (a) Schematic layout of MIDF. Both the storage ring and the synchrotron accommodate five CW and five CCW beams in a multi-story beam line. (CW = clockwise, CCW = counter-clockwise) (b) The reactor chamber with the driver beam lines.

[4] V. Dolgashev and S. Tantawi, "Design of High Efficiency High Power Electron Accelerator Systems Based on Normal Conducting RF Technology for Energy and Environmental Applications", Design Study Report, SLAC National Accelerator Laboratory, https://doi.org/10.2172/1441166 (2018).

[5] A. Simonin et al., "Towards a Maintainable and High Efficiency Neutral Beam System for Future Fusion Reactors", *Nucl. Fusion,* **61**, 046003 (2021).

[6] F. Meot et al., "High Power from Fixed-Field Rings in the Accelerator-Driven Sub-Critical Reactor Application", *Phys. Procedia,* **66**, pp. 129–139 (2015).

[7] M.D. Rosen, "The Physics Issues That Determine Inertial Confinement Fusion Target Gain and Driver Requirements: A Tutorial", *Phys. Plasmas,* **6**, pp. 1690–1699 (1999).

[8] K.D. Kok (Editor), "Nuclear Engineering Handbook", 2nd Ed., CRC Press, ISBN: 978-1482215922 (2016).

[9] S. Atzeni and J. Meyer-ter-Vehn, "The Physics of Inertial Fusion: Beam Plasma Interaction, Hydrodynamics, Hot Dense Matter", Oxford University Press, ISBN: 978-0198562641 (2004).

[10] J.F. Ziegler, "SRIM-2013 – The Stopping and Range of Ions in Matter", http://www.srim.org/ (2013).

[11] B. Badger et al., "HIBALL – A Conceptual Heavy Ion Beam Driven Fusion Reactor Study", KfK **3202/1**, UWFDM-450 (1981).

[12] Y. Fujii-e et al., "Heavy Ion Fusion Reactor HIBLIC-I – Conceptual Design of Heavy Ion Fusion Reactor", IPPJ-663, Institute of Plasma Physics, Nagoya Univ. (1984).

[13] B. Badger et al., "HIBALL-II – An Improved Conceptual Heavy Ion Beam Driven Fusion Reactor Study", KfK **3840**, FPA-84-4, UWFDM-625 (1985).

[14] W.R. Meier et al., "OSIRIS and SOMBRERO Inertial Fusion Power Plant Designs, Vol. 1 Executive Summary and Overview", WJSA-92-01, DOE/ER/54100-1 (1992).

[15] R.W. Moir et al., "HYLIFE-II: A Molten-Salt Inertial Fusion Energy Power Plant Design – Final Report", *Fusion Technol.*, **25**, pp. 5–25 (1994).

[16] K. Takayama et al., "Experimental Demonstration of the Induction Synchrotron", *Phys. Rev. Lett.* **98**, 054801 (2007).

Target design for heavy ion beam inertial confinement fusion

Toru Sasaki[1], Kotaro Kondo[2], Takashi Kikuchi[3], and Kazuhiko Horioka[4]

[1]Department of Science of Technology Innovation, Nagaoka University of Technology

[2]National Institutes for Quantum Science and Technology

[3]Department of Nuclear System Safety Engineering, Nagaoka University of Technology

[4]Tokyo Institute of Technology

ABSTRACT

A massive ion beam (MIB) driver has an opportunity to open new inertial confinement fusion (ICF) concepts. In this paper, we described the fuel target design for direct-beam-driven ICF to achieve a fusion output equivalent to 2 GJ, based on the parameters of the MIB driver. The energy gain and the required fuel mass were estimated to achieve a 2 GJ reactor. To achieve the implosion velocity exceeding 10^8 cm/s, we parametrically surveyed the target material considering the average stopping power and their range. The results show that the Niu-Kawata target is almost suitable for using the MIBIF. The beam pattern to use MIBs was also determined to suppress the beam illumination non-uniformity.

Keywords

Key Words　Energy gain, Fuel mass, Target material, Beam illumination nonuniformity

1. Introduction

Ion beam-driven inertial confinement fusion (ICF) is characterized by a long range of energy deposition inside the target. The ion beam enters the fuel target through Coulomb collisions between the ions and the electrons in the fuel target. Finally, there is a point just before the ion beam stops, called the Bragg peak, where energy deposition is maximum. Since the energy deposition process is due to Coulomb collisions, the spatiotemporal energy deposition distribution with respect to the beam entry direction during the implosion process can be easily predicted. For this reason, various fuel target structures such as direct drive [1-3], indirect drive [4], cylindrical targets [5], and X-targets [6] have been investigated in conventional beam-driven ICF, using characteristic energy-imparting processes that are not available in lasers. This has resulted in a variety of required parameters for the ion beam driver.

In a massive ion beam (MIB) [7], 100 beams per fuel target can be controlled, and direct-drive ICF studies are possible. By utilizing the above-mentioned energy transfer inside the target, which is a major feature of ion beam-driven ICF, direct heating of the ablator material, suppression of fluid behavior by tampering, heat retention effect, and uniform heating by circumferential radiation transport are expected. On the other hand, direct-driven fuel targets require uniform compression of the fuel target to achieve the conditions necessary for fuel ignition. Therefore, it is necessary to consider beam pattern and beam irradiation non-uniformity caused by the beam irradiation pattern.

In this paper, we described the fuel target design for direct-driven ICF to achieve a fusion output equivalent to 2 GJ, based on the parameters of the ion beam driver.

2. Energy gain from fuel target

The heating of the fuel target in direct-beam-driven ICF can be regarded as an isobaric model as in laser-driven ICF. Therefore, considering the power balance at the center of the hot spot dE/dt, we obtain

$$\frac{dE}{dt} = W_{dep} - W_m - W_r - W_e, \qquad (1)$$

where W_{dep} is the energy given by the DT fusion reaction products as α particles and neutrons in a unit time, W_m is the pdV work of the hot spot in a unit time, and W_e represents the heat conduction loss of electrons in a unit time. In the direct-drive ICF case, W_m =0 is assumed since the hot spot and the outer fuel are under the same pressure condition. In summary, the areal density product of the hot spot $\rho_H R_H$ must satisfy the following conditions,

$$\rho_H R_H > \left\{ \frac{3A_e (\ln \Lambda)^{-1} T_H^{7/2}}{A_\alpha < \sigma v > f_\alpha - A_B T_H} \right\}, \qquad (2)$$

where, $A_e = 9.5 \times 10^{19}$ erg $s^{-1}cm^{-1}keV^{-7/2}$ is the electron thermal conduction, ln Λ is the Coulomb logarithm, T_H is the temperature of the hot spot, $A_\alpha = 8 \times 10^{40}$ erg/g^2 is the given energy density of 3.5 MeV α particles produced by the fusion reaction, $< \sigma v >$ is the fusion reaction cross section of DT, f_α is the fraction of α particles imparted to the hot spot [8], and $A_B = 3.05 \times 10^{23}$ erg $cm^3 g^{-2} s^{-1} keV^{-1/2}$ is the constant of Bremsstrahlung radiation.

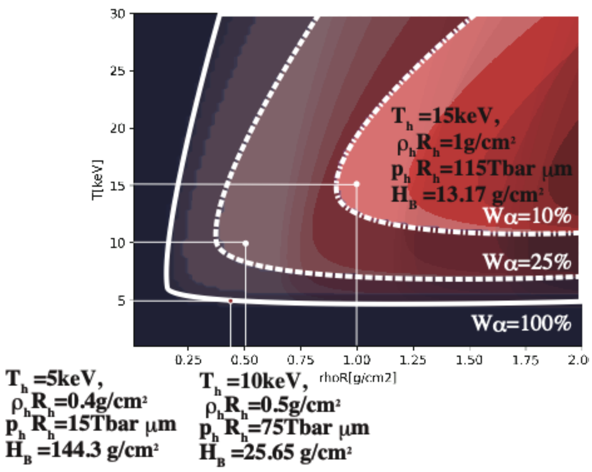

Figure. 1 Self-heating condition on $\rho_H R_H$- T_H diagram

Using eq. (2), we can find the self-heating conditions on the $\rho_H R_H$ of the hot spot and the window of temperature T_H as shown in Fig. 1. Three scenarios are shown in Fig. 1, where the self-heating condition is parameterized by the energy imparted in the fuel by the α particle heating. As shown in Fig. 1, the higher the $\rho_H R_H$ and T_H, the higher the energy density inside the fuel target. To achieve the self-heating condition, the power of the α particle heating must exceed the power loss due to bremsstrahlung, and the hot spot temperature required for this is approximately $T_H \sim 5$ keV. On the other hand, an excessively high hot spot temperature causes power loss due to electron heat conduction. Thus, a larger $\rho_H R_H$ is preferable for the fuel target design.

From Fig. 1, we considered the obtained target gain based on the self-heating conditions. Assuming a spherically symmetric implosion of the fuel target and dividing the heated and compressed region into a hot spot and a cold compressed region around the hot spot, the energy gain of target G can be expressed as follows.

$$G = \frac{4\pi}{3} \frac{q_{DT}}{E_d} \left[\rho_H R_H^3 + \rho_c \left(R_f^3 - R_H^3 \right) \right] \Phi \qquad (3)$$

where, $q_{DT} = 3.37 \times 10^{11}$ J/g is the fusion reaction energy per unit mass of DT fuel, E_d is the energy input by the energy driver, ρ_c is the density of the cold compression area, R_f is the overall fuel radius, and Φ is the burn fraction. Here, the burn fraction Φ is defined as follows.

$$\Phi = \frac{H_H + H_c}{H_B + H_H + H_c}, \qquad (4)$$

where, $H_H = \rho_H R_H$ is the areal density product of the hot spot, $H_c = \rho_c (R_f - R_c)$ is the areal density product of the cold compression area, and $H_B = 8C_s m_f / < \sigma v >$ is the burning parameter. C_s is the sound velocity of the fuel and m_f is the average mass of DT fuel atoms. From eq. (4), the compressible fuel mass M_f can be written as

$$M_f = \frac{4\pi}{3} \left[\rho_H R_H^3 + \rho_c \left(R_f^3 - R_H^3 \right) \right] \qquad (5)$$

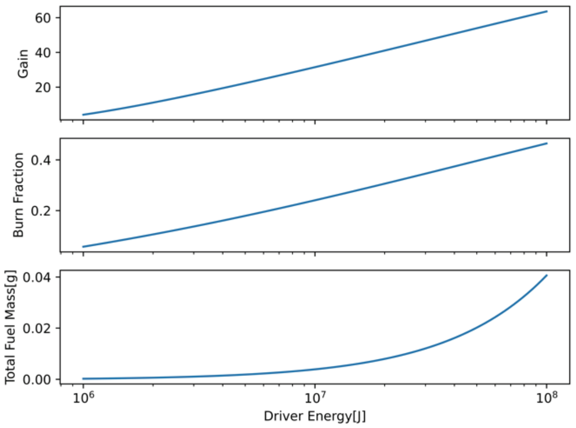

Figure 2 Fuel gain, burn fraction, and total fuel mass as a function of driver energy (Assuming T_h = 10 keV, pR_H = 115 Tbar μm, 2% of coupling efficiency from driver to fuel , and isentrope parameter α=3).

Equations (3)-(5) determine the energy gain, burn fraction, and fuel mass. However, not all of the energy input by the energy driver is used to detonate and heat the fuel target. For this reason, the overall energy conversion efficiency between the fuel and driver is defined as follows.

$$\eta = \frac{E_f}{E_d} \tag{6}$$

where E_f is the internal energy of the fuel target at ignition. Assuming electrons in the fuel are degenerate in the low-temperature compression region, the relationship between pressure and density [8] can be expressed as follows,

$$\rho_c = \left(\alpha A_{\mathrm{deg}}\right)^{-3/5} p^{3/5} \tag{7}$$

where α is the isentrope parameter, A_{deg} is the constant of the Fermi degenerate condition, and the p is the pressure of the compressed core. α=1 indicates that the electrons in DT fuel are completely degenerate. For larger values of α, compression becomes harder and harder as the state moves away from the degenerate state. Using these variables, the fuel target gain, burn fraction, and fuel mass relative to the driver energy are shown in Fig. 2, based on the relationship between the target gain G, burnup rate Φ, and compressible fuel mass M_f given by eqs. (3)-(5) as a function of the driver energy E_d. Note that the calculation assumes T_h = 10 keV, pR_H = 115 Tbar-μm, η= 2 %, degeneracy parameter α=3, and $\rho_H R_H$=0.5 g/cm^2. The results show that a gain of about 50 and a burnup rate of about 30% can be expected when the driver energy is 40 MJ. However, the mass of the DT fuel is approximately 20 mg, which requires a larger target than the fuel targets for heavy-ion beam ICF [3] and laser fusion [8].

3. Implosion process of fuel pellet in MIB ICF

The implosion process of the direct-driven fuel target of the MIB ICF is similar to that of the laser, but since the ion beam penetrates and heats the fuel target, the penetration length of the ion beam must be controlled by the thickness of the ablator and other factors. The ablation surface propagates as a radiative shock wave as in laser-driven ICF [8]. The propagation of the ablation surface is supported by the self-absorption of radiation from the outer material and the energy deposition of the ion beam on the target. The basic mechanism is the same as that of laser-driven ICF. A major difference is that the ion beam penetrates the fuel target and heats a large volume, thereby ablating the target structure and generating a large reaction force. Thus, the mass of the ablator can be increased, compressing a relatively large volume compared to a laser-driven ICF.

It is also desirable to isentropic compress the fuel as much as possible. By placing a tamper around the periphery of the ablator, the generated radiation can be confined like an oven to maintain the pressure driven inside. For this reason, direct drive targets for MIB ICFs that drive implosion by radiation energy in addition to shock waves from ion beams are also being considered.

On the other hand, in the case of the central ignition scheme, the implosion velocity v_{imp} is also important. This velocity determines the stagnation pressure p_{stag} at the center of target. In general, since the stagnation pressure is $p_{\mathrm{stag}} \propto v_{\mathrm{imp}}^3 \alpha^{-9/10}$ [8], it is important to select an ablator to achieve a sufficient implosion velocity (~10^8 cm/s).

The radiation-driven shock wave adiabatically

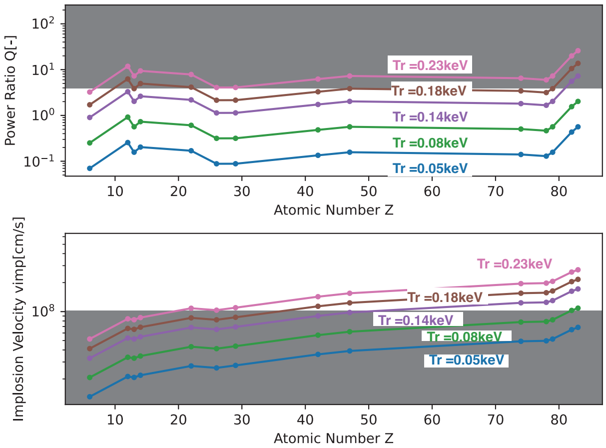

Figure 3 The power ratio between the radiation power P_r and the hydrodynamic power P_h and the implosion velocity v_{imp} as a function of materials. (Assuming the isentrope parameter $\alpha = 3$, and the inflight aspect ratio A_{if}=30).

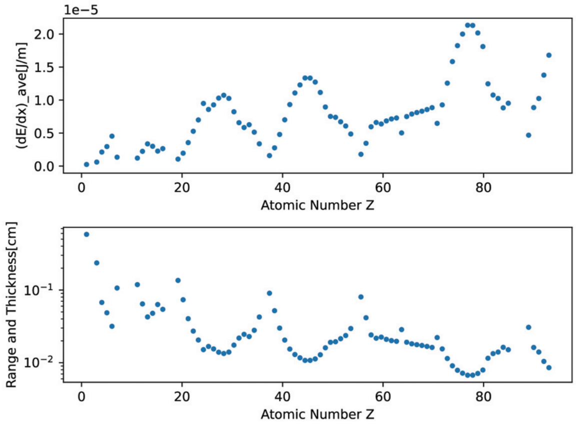

Figure 4 Atomic number dependence on the average stopping power $\overline{dE/dx}$ and the ion beam range.

compresses the DT fuel multiple times to create a dense fuel shell. Here, the intense radiation drives the ablative heat wave, and in the case of subsonic deflagration mode Q, which represents the balance between the power generated by the radiation power P_r and the hydrodynamic power P_h, must be smaller than 4[8] .

$$Q = \frac{P_r}{P_h} = \frac{\sigma_B T_r^4}{\rho C_s^3} < 4 \tag{12}$$

Based on this relationship, the ablator material that can achieve the detonation velocity was examined as shown in Fig. 3. In this analysis, the radiation temperature T_r is assumed to be equal to the ion temperature T_i and the electron temperature T_e. In fact, the time scales of the radiation temperature and electron temperature relaxation are sufficiently short (fs~ps) compared to the hydrodynamic time scale, followed by the electron-ion relaxation (10~100 ps). As for the ionization model, More's model is used, in which takes degenerate ionization into account[9]. From these results, the radiation temperature T_r should be approximately 0.2 keV to satisfy the balance Q between the radiation generated power T_r and the hydrodynamic power P_h less than 4. On the other hand, the ablation pressure, ablation velocity, and implosion velocity generally increase monotonically with atomic number. Based on these results, the implosion velocity $v_{\mathrm{imp}} \sim 10^8$ cm/s required for the central ignition method can be satisfied using Al with atomic number 13, which is used in the conventional Niu-Kawata fuel target [10]. Furthermore, materials with a medium atomic number, such as iron, may be candidates for ablators to obtain a large implosion velocity.

The energy transfer process when the ion beam enters the ablator material is determined from the stopping power of the target material. The stopping power of solid materials for light ions has been measured many times, and Ziegler et al.[11]. In the case of heavy ions, the average ion valence has a large effect on the stopping power because the ions are not completely ionized in the target at an incident energy of several 10 MeV/u. Figure 4 shows the results of the average stopping power $\overline{dE/dx}$ to be given to the ablator material. Melhorn's model [12] was used to calculate the stopping power, and More's ionization model [9] was used for the average ion degree. The results show that $\overline{dE/dx}$ increases with atomic number, but not monotonically. This is because the stopping power is generally proportional to the density of the ablator material. Therefore, materials with relatively high density have a large $\overline{dE/dx}$. On the other hand, since the ion stopping range becomes shorter as $\overline{dE/dx}$ increases, the use of a high-density target is advantageous in increasing the deposition energy density and the radiation temperature T_r.

4. Scenarios and issues of uniform irradiation using MIB

One of the important issues of the direct-driven fuel target of the MIB is the non-uniformity of the beam irradiation [13]. Since the energy imparted by heavy ions to the target is distributed in the beam travel direction, it is necessary to study the degree of non-uniformity based on the energy imparted to the spherical target. Therefore, a method of modeling the degree of non-uniformity of each surface energy imparted based on the total amount of energy imparted in the direction of travel has been proposed [14].

Figure 5 shows the dependence of the beam irradiation non-uniformity on the number of beams, based on beam irradiation patterns simulating regular polyhedral and fullerene geometries, which are considered to achieve near spherical symmetry in implosion [14]. The Kapchinsky-Vladimirsky (KV) or Gauss distribution is assumed for the radial phase space distribution of the ion beam, and the effect of the momentum dispersion in the beam direction assuming a beam temperature of 100 MeV is also investigated. The results show that the beam illumination non-uniformity decreases with the number of irradiated beams. When the momentum dispersion in the beam propagation direction is relatively large, the beam illumination non-uniformity is found to be about 2% even 32 beams.

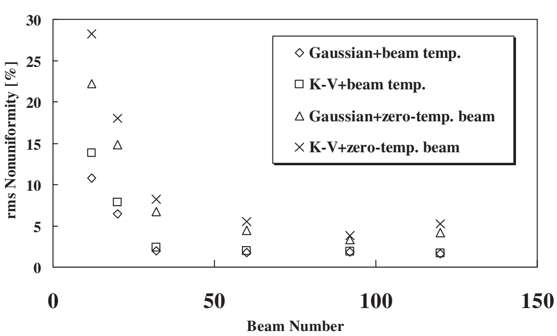

Figure 5 Beam illumination nonuniformity as a function of the number of MIBs [14](Copyright from T. Someya et al, Phys. Rev. ST AB, **7**, 044701 (2004))

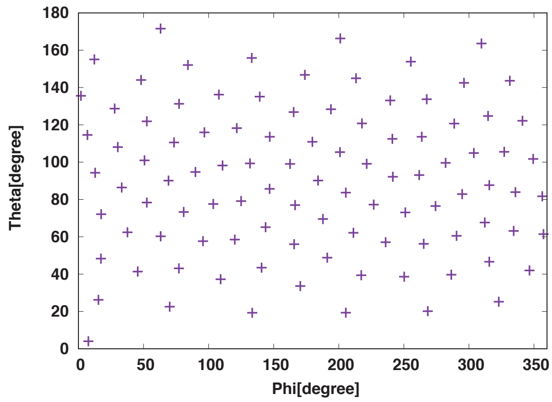

Figure 6 Optimum beam pattern on the target by using 100 MIBs

In addition, increasing the number of beams does not reduce the beam illumination non-uniformity. On the other hand, when the momentum dispersion in the traveling direction is small, the beam illumination non-uniformity becomes relatively large. In addition, the results of the analysis in the paper [14] indicate that the low-frequency mode of the beam illumination may be observed, which may cause Rayleigh-Taylor instability. Therefore, it is important to consider an irradiation pattern that suppresses the beam illumination non-uniformity in the low-frequency mode [15,16].

In the MIB ICF, 100 beams are irradiated to the target. Therefore, it is necessary to optimize the beam illumination pattern. Figure 6 shows the beam illumination pattern when 100 beams are handled based on the method studied by Murakami et al. [17]. Based on the beam illumination pattern obtained by the above method, the beam illumination non-uniformity was evaluated using the method of Kawata et al. [14]. The target structure in this case is a conventional Niu-Kawata target, which is the same structure as in the paper [14]. The beam illumination non-uniformity is 2.28% considering the MIB ICF driver [7] case. Although the MIB ICF driver [7] can handle 100 beams, irradiation from the zenith direction is extremely difficult due to the limitations of the beam transport system. As shown in Fig. 6, irradiation from the zenith direction is not necessary. As an example, Lin et al. proposed the Flower target, in which the density and material thickness are precisely controlled according to the energy delivery profile to the target [18].

4. Conclusions

In this paper, we described the fuel target design for direct-beam-driven ICF to achieve a fusion output equivalent to 2 GJ, based on the parameters of the MIB driver. The energy gain and the required fuel mass were estimated to achieve a 2 GJ reactor. To achieve the implosion velocity exceeding 10^8 cm/s, we parametrically surveyed the target material considering the average stopping power and their range. The results show that the Niu-Kawata target is almost suitable for using the MIBIF. The beam pattern to use MIBs was also determined to suppress the beam illumination non-uniformity.

Compared to conventional direct-driven targets, MIB ICF targets are attractive because the direct irradiation pattern can be studied. 2 GJ-class fusion output energy gains can be achieved, although the mass of the fuel DT is larger. On the other hand, optimization of the fuel target structure and the dynamics of implosion need to be considered, especially hydrodynamic instabilities associated with non-uniform implosion and radiation transport inside the target.

References

[1] K. A. Long and N. A. Tahir, "Range shortening, radiation transport, and Rayleigh-Taylor instability phenomena in ion-beam-driven inertial-fusion-reactor-size targets: Implosion, ignition, and burn phases", Phys. Rev. A, **35** 2631 (1987)

[2] B. G. Logan *et al.*, "Direct drive heavy-ion-beam inertial fusion at high coupling efficiency," Phys. Plasmas, **15**, 072701 (2008)

[3] S. Kawata, "Direct-drive heavy ion beam inertial confinement fusion: a review, toward our future energy source", Advances in Physics: X, **6**, 1873860 (2021)

[4] D. A. Callahan-Miller and M. Tabak, "Increasing the coupling efficiency in a heavy ion, inertial confinement fusion target", Nuclear Fusion, **39**, 883 (1999)

[5] N. A. Tahir *et al.*, "Laboratory planetary science studies using intense heavy ion beams at FAIR: The HEDgeHOB collaboration", NIM A, **606**, 177 (2009)

[6] E. Henestroza *et al.*, "Progress towards a high-gain and robust target design for heavy ion fusion", Phys. Plasmas, **18**, 032702 (2011)

[7] K. Takayama *et al.*, "A massive-ion beam driver for high-energy-density physics and future inertial fusion", Phys. Lett. A, **384**, 126692 (2020)

[8] S. Atzeni and J. Meyer-ter-Vehn, "The Physics of Inertial Fusion: Beam Plasma Interaction, Hydrodynamics, Hot Dense Matter", Oxford University Press (2004)

[9] R. M. More, "Atomic Physics of laser-produced plasmas" in Handbook of Plasma Physics (eds. M. N, Rosenbluth and R. Z. Sagdeev) Vol. 3: Physics of laser plasma (eds. A. M. Rubenchik and S. Witkowski) pp. 63-109 North-Holland, Amsterdam (1991)

[10] K. Niu and S. Kawata, "Proposal of Power Plant by Light Ion Beam Fusion", Fusion Technol., **11**, 365 (1987)

[11] J. F. Ziegler *et al.*, "In The Stopping and Range of Ions in matter", volume 1, (Pergamon, New York, 1985).

[12] T. A. Melhorn, "A finite material temperature model for ion energy deposition in ion-driven inertial confinement fusion target design", J. Appl. Phys, **52**, 6522 (1981)

[13] A. I. Ogoyski *et al.*, "Code OK2—A simulation code of ion-beam illumination on an arbitrary shape and structure target" Comp. Phys. Commn, **157**, 160 (2004)

[14] T. Someya *et al.*, "Heavy-ion beam illumination on a direct-driven pellet in heavy-ion inertial fusion," Phys. Rev. ST AB, **7**, 044701 (2004)

[15] H. Takabe, *et al.*, "Self‐consistent growth rate of the Rayleigh‐Taylor instability in an ablatively accelerating plasma" Phys. Fluids, **28**, 3676 (1985)

[16] D. H. Munro, “Analytic solutions for Rayleigh-Taylor growth rates in smooth density gradients”, Phys. Rev. A, **38**, 1433 (1988)

[17] M. Murakami *et al.*, “Optimization of irradiation configuration in laser fusion utilizing self-organizing electrodynamic system,” Phys. Plasmas, **17**, 082702 (2010)

[18] Z. Lin *et al*, “Reduction of Energy Deposition Non-Uniformity by Adjustment of Pellet Structure for Heavy-Ion-Beam Inertial Confinement Fusion”, PFR, **17**, 2404064 (2022)

Inertial Fusion Energy driven by the Massive Ion-Beam Accelerator : 1Hz Operation of 2 Giga-joule Micro-explosion

Kazuhiko Horioka

Tokyo Institute of Technology, Tokyo 152-8550, Japan

ABSTRACT

A new concept of energetic multi-bunch heavy-ion accelerator enables us to explore robust implosion schemes for the reactor of inertial fusion energy (IFE). The energetic beam driver capable of producing total energy order of magnitude greater than the ordinary inertial fusion drivers is shown to bring an alternative way (a power system driven by 1Hz operation of 2 giga joule micro-explosion) to produce electrical power from hydrogen fuel. Reactor chamber issues are addressed such as the response of the reactor first wall to the micro-explosion of DT fusion. An active evacuation method is proposed to adjust a key concern of the chamber issues; the recovery of the chamber environment after the explosion for the ion beam transport and the target injection.

Keywords

Heavy ion fusion, Inertial fusion energy, Massive beams, Fuel gain, Reactor recovery, Liquid wall, Ablation, Particle management, Active evacuation

1. Introduction

Recently, National Ignition Facility (NIF) at Lawrence Livermore National Laboratory (LLNL) demonstrated a proof of existence of the ignition state of DT fusion in the laboratory by an implosion of spherical pellet in a high-Z radiation cavity (hohlraum) [1,2]. The stage of R&D on the inertial confinement fusion (ICF) seems to move to exploration of a practical way for an electrical power system based on inertial fusion energy (IFE).

Most inertial confinement fusion (ICF) approaches pursue laser driven central hot-spot ignition in which both compression of the fuel to almost 10^3 times of solid density and heating of the target center to the ignition temperature, must be accomplished simultaneously. That is, in the final stage of compression, a localized area of high entropy stagnated region (hot-spot) must be surrounded by much lower entropy fuel. Namely, the high temperature central spark plug and the high density (much lower temperature) fuel must go together in the same fuel. However, the compression and the heating intimately coupled to each other through hydrodynamics and thermodynamics during the implosion. In addition, the spherical fast implosion suffers from various hydrodynamic instabilities which induce mixing and/or eddies in the sensitive region of the fuel core. As a result, the hydrodynamical instabilities degrade the conversion efficiency from kinetic energy to internal energy of the fuel at stagnation. Accordingly, the central spark ignition scheme strongly increases the requirement of high-precision symmetrical drive of the target.

Recent NIF results at LLNL seem to request a more robust, reproducible, and steady implosion scheme against the instability for the practical IFE system. From point view of the power plant system that must operates steadily and repetitively, particularly the energy driver must operate successively at a MW average power level. The 1Hz repetition to generate 1GW electricity from a single target chamber is also a challenge.

Then the critical issues of IFEs are ;

- Assure repetition capability of the reactor system particularly the driver and the chamber
- Explore the implosion rocess for more robust schemes.

From point view of repetition capability, an energy driver system based on an intense heavy ion accelerator has always been considered to be promising for a practical ICF reactor [3]. However, developing a massive, high average power, efficient, and low-cost heavy ion accelerator remains a critical issue for heavy ion inertial fusion (HIF).

The hydrodynamics and the fusion gain of ICF-target are sensitive functions of the irradiation scheme and energy deposition profiles of the driver. While the laser-matter interaction is complex and not predictable, the energy deposition process of energetic ions is completely different from that of intense laser. That is, the laser light is basically cut off at the critical density and the energy deposition process at denser region depends on the plasma behavior. On the other hand, that of energetic heavy ion beams (HIBs) can be almost explained by the Coulomb collision that enables us to predict and control the deposition profile in a target [4].

The merits of the HIBs for the driver include:

- Efficient coupling
- Controlling the energy deposition profile;
- Pre-heat suppression;
- Localized energy deposition;
- Cost-effective system.

Utilizing these advantages, we can extend the area of target structure for steady target gain.

Also, HIBs can penetrate into a dense region and deposit significant energy at the end of the range (at the Bragg peak). This is another advantageous point for the drive of ICF target and allows us to explore various distinctive target structures capable of providing steady fusion yield.

2. Massive Ion Beam Driver

An accelerator system using repetitive induction modulator was proposed as a cost-effective and massive ion beam (MIB) driver in which counter-facing, two-way (forward and backward) multiple beams are accelerated in a compact stacking ring (Two way and multiplex scheme) [5].

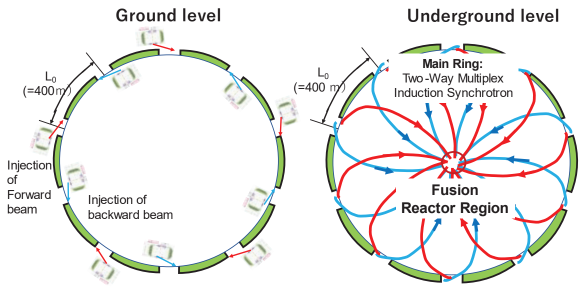

Fig.1 Schematic illustration of main-ring of the massive ion beam accelerator [5].

An illustration of the two-way multiplex induction synchrotron is shown in Fig.1, which makes use of maximum magnetic-flux density and the induction fields by the two way acceleration.

Parameters of the accelerator and the beam are shown in Table 1 [5]. As shown, the accelerator system expected to accelerate 400kJ of massive multiple 9GeV Pb+ ion bunches with high (~ 30%) electrical efficiency via the two-way stacking ring composed of permanent bending magnets.

The main ring has 10-fold symmetry and the fusion reactor will be placed in the center of the ring.

Table 1 Parameters of massive ion-beam accelerator.

Accelerator and Beam Parameters		
Circumference	[m]	4000
Acceleration cycle	[Hz]	1
Ions		$^{208}\mathbf{Pb}^{1+}$
Beam energy	E_f [GeV]	9
Particles from Injector	N_0	$7\mathrm{x}10^{13}$
Number of injector pulses to create 1 superbunch		4
Particles in superbunch	N_S= 4x N_0	$2.8\mathrm{x}10^{14}$
Number of superbunches		10
Forward /backward beams		5/5
Total number of particles	2x5x10 N_S	$2.8\mathrm{x}10^{16}$
Total beam energy	E_b [MJ]	40

energetic ion-beam driver consists of 100 of 400 kJ beam bunches, the total diver energy E_d can be 40 MJ.

3. Possible Schemes available by the Massive Beam Driver for Steady Fusion Yield

3.1 Guideline for steady fusion yield

One of the most important index characterizing the target compression is the isentropic parameter α

$$\alpha = p(\rho, T)/p_{deg}(\rho), \qquad (1)$$

where p_{deg} is the fuel pressure with Fermi-degenerated electrons [6]. Then α (=1~4) indicates entropy of the fuel which largely depends on the history of the compression. Since ICF target requires highest compression for given pressure p, we have to keep α as small as possible during the implosion.

Simplified analytical study indicates that basically the fuel gain G_f is a strong function of the isentropic parameter and the diver energy E_d. That can be analytically derived as follows,

$$G_f \propto (\eta E_d)^{\beta}/\alpha^{\gamma}, \qquad (2)$$

where E_d is the driver energy, η is the coupling (driver to fuel energy) efficiency. The exponents range β = 0.3~0.4 and γ = 0.9~1.2, depending on the implosion scheme. This indicates that keeping the entropy of the fuel as small as possible using an energetic driver which can control its energy deposition profile for the low entropy compression, are of primary importance. That is, regardless of implosion schemes, Eq. (2) indicates a guideline for steady yield of the fusion energy.

3.2 Possible Schemes

The 100 beams enable us to directly drive the target with multiple beams irradiation [7]. A schematic of a direct ion-beam drive target is shown in Fig. 2(a). In case of the MIB drive, a quasi-spherical (barrel shaped) target is planned to use due to geometrical restriction of the accelerator. The upper and the lower regions are planned to be independently irradiated to make hydrodynamical tamper for the compressed core. They are expected also to work as a shock wave (hot-spot) igniter in the compressed fuel. The massive driver of E_b =40 MJ is considered to be advantageous

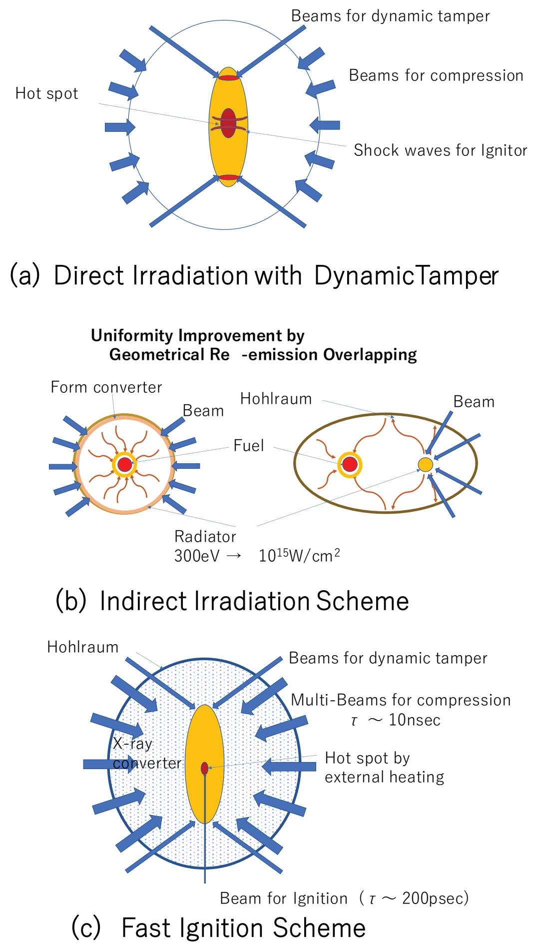

Fig. 2 Examples of irradiation schemes available by the massive ion-beam driver.

to relax the compression requirement and achieve a robust implosion of the fuel. The gain improvement could be achieved by changing the temporal pulse shape as to reduce entropy generation.

The radiative symmetrization is a critical measure in the achievement of highly uniform implosion. Illustrations of indirect-driven targets available by the MIB driver are shown in Fig. 2(b). As illustrated in the figure, MIBs penetrate into the X-ray converter inside the pellet or radiation cavity (hohlraum) in which a form is filled as an X-ray radiation converter [8]. MIBs penetrate through the tamper or hohlraum and the multiple beams heat the form Xray-converter. The indirect drive target relies on smoothing by radiation energy transport in the fuel pellet, and in a casing enclosing the fuel pellet. The outer high-Z layer of Fig. 2 (b) has tamping effect which can increase the

The radiative symmetrization is a critical measure in the achievement of highly uniform implosion. Illustrations of indirect-driven targets available by the MIB driver are shown in Fig.2 (b). As illustrated in the figure, MIBs penetrate into the X-ray converter inside the pellet or radiation cavity (hohlraum) in which a form is filled as a X-ray radiation converter [8]. MIBs penetrate through the tamper or hohlraum and the multiple beams heat the form Xray-converter. The indirect drive target relies on smoothing by radiation energy transport in the fuel pellet, and in a casing enclosing the fuel pellet. The outer high-Z layer of Fig.2 (b) has tamping effect which can increase the hydrodynamic efficiency. The improvement can be achieved also by a beam-driven optically thick capsule that suppress the radiation loss and could increase the fusion yield.

The concept of fast ignition (FI) shown in Fig.2 (c) is to separate the fuel compression process from heating of the central spot. That is, in the FI scheme, the compression can be carefully scheduled to keep the entropy production as small as possible. A tandem acceleration of the target is planned to use to increase the implosion velocity with minimum entropy generation [9]. After the near isentropic compression, the core is ignited by an external energy driver that makes the target hydrodynamically less sensitive to implosion asymmetries. The FI approach has flexibility of target design which relaxes symmetry requirement and allows non-spherical drive.

The delivery of ignition trigger and efficient coupling of an ultra-intense beam pulse are the prise to be paid for FI. Although Petta-watt (PW) laser has been the primarily candidate of the external ignition driver, the core of fuel has a high density in the order of $n / n_c \sim 10^5$. Then the feasibility of external trigger by Peta-watt (PW) laser largely depends on the energy transport from the laser absorption layer (n_c) to the compressed dense fuel core. However, that is not established yet.

Table 2 Expected reactor parameters driven by the massive ion-beam driver.

Reactor Parameters		
Fusion Yield	E_o GJ/Shot	2
Chamber radius	[m]	5
First wall	Liquid	LiPb
Chamber pressure	[Pa]	< 0.1
Fluence to first wall	[J/cm^2]	>10
Cycle	[Hz]	1
Target Gain	E_o / E_b	50
Driver efficiency	η_d [%]	30

Recently a new concept using bunch rotation in a large amplitude detuned RF cavity was proposed as a method to make ultra-short heavy-ion-beam pulse in which a number of bunch trains are stacked by the detuned RF cavities [10]. That extends the area of target structure of HIF from conventional hot-spot ignition to the ion-beam driven FI scheme.

3.3 New Area of Target Design

As illustrated in Fig.2, energetic ion beams can deposit their energy in an internal structure through an outer component such as high-Z radiation cavity and tamper of fuel pellet. In addition, HIB can deposit its energy in a localized dense region and the deposition profile is well-defined.

Utilizing these features, the MIB driver can largely extend the area of target structure and/or irradiation scheme [11]. All of the proposals shown in Fig.2 are new structures of HIF target available and extended by the MIB driver.

Among the various approaches, FI seems to be the most attractive scheme, when intense short pulse beam is developed, to realize robust and reproducible high fusion yield.

Table 2 summarizes the expected plant parameters. We assume modest target gain of 50 for the IFE system driven by the energetic, robust and efficient (η_d ~30%) beam accelerator. Those are supposed to increase the robustness and steadiness of the whole system of the power plant.

4. Response of LiPb First Wall to the GJ-level Micro-explosion and Recovery of the Chamber Environment

The target chamber must survive the GJ-level micro-explosion. When energy fluence to the first wall increases, a renewable liquid wall is an attractive and provably only possible chamber wall option particularly when the wall protection is highly challenging in the case of the HIF reactor with 2GJ / Hz fusion yield. In addition, the ion-beams must propagate without severe scattering through the reactor background gas to the target. Then the propagation limits the background gas density of chamber [12.13].

4.1 Products and by-products induced by the GJ micro-explosion

The target micro-explosion releases its energy in the form of neutrons, photons, and fast ions. When the DT-fuel target is successfully ignited, it produces fusion products with energy gain of 17.6 MeV / event. Accordingly, the number of He particles; N_{He} accompanied by GJ micro-explosion of DT fusion can be estimated to be;

$$N_{He} = 3.55 \times 10^{20} / \text{(GJ) Shot.} \quad (3)$$

Assuming a burn-up of 30%, the total number of particles that must be removed before the next operation to be more than 10^{21} particles except the by-products accompanied by the wall interaction. Although the helium ash management is of critical issue of all of the fusion reactors, all of the particles must be cleared below the density level that does not disturb the ion-beam propagation in the case of HIB reactor.

Table 3 Fractional output energy for typical reactor size targets.

Fusion Products	Laser Direct Drive	Target with High-Z Layer
X-Rays	0.06	0.22
Debris	0.19	0.09
Neutrons	0.75	0.70

The fractional energy yield from typical fusion target is shown in Table 3 [14].

4.2 Response of Liquid First Wall

Most of the X-ray energy accompanied by the explosion is below a few keV. Neutrons tend to penetrate and cause less energy deposition near surface region. When the background gas density is low, the X-rays and target debris ions deposit their energy mainly in the first surface. A renewable liquid layer is attractive chamber wall option particularly when the wall protection is highly challenging such as the HIF reactor.

The reactor first wall is subjected to prompt energy deposition from the X-rays and fast ions composed of target debris, and helium ash produced by the micro-explosion. As most of energy is deposited within 10 μm of the surface, only a thin layer is subjected to high temperature. The neutrons penetrate much deeper in the wall structure. Then the major threats of evaporation to the first wall are the X-rays and the ions. Although a first wall configuration based on a thin Tungsten armor was considered as a laser IFE solid wall chamber [15], survival from the thermo-mechanical stress and melting is considered to be almost impossible [16]. In case of the Laser-IFE, a key concern was the survival of the first solid wall under the X-ray, high speed plasma flux, and He from the fusion micro- explosion. Helium ash management including the He behavior in the first wall material was also critical concern. The response and the recovery of reactor environment after the micro-explosion should be a critical issue for the stable reactor operation of IFEs [17].

A schematic illustration of the reactor wall interaction is shown in Fig.3. For a prompt (less than hydro-time scale) energy deposition, ablation threshold of condensed matters is estimated to be ~ 2J/cm^2 [18]. The ions and X-rays fluences from the 2GJ explosion on the chamber wall with a radius of 5m are estimated to be ~ 80 J/cm^2 and ~ 17 J/cm^2 respectively.

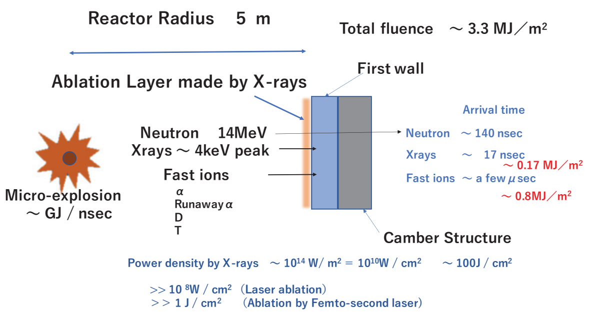

Fig.3 Schematic of the response of liquid wall to the micro-explosion.

Those values are much larger than the ablation threshold and suggest that the first wall inevitably ablates by the X-rays and/or fast ions from the micro-explosion. That is, as any solid wall cannot survive from the explosion, a sacrificial layer of liquid metal is inevitable for the first wall of massive beam IFEs.

The ablated material could generate aerosol in the chamber, which could result in a chamber environment unsuitable for the driver beam propagation and/or fuel target injection.

The energy partitioning, and the ion and photon spectra tend to be similar to those from the typical targets. As shown in Table1, the density limit of

background gas for ballistic propagation of HIBs is estimated to be 0.1 Pa [12,13]. Then the choice of the first surface is the main decision of HIF reactors.

4.3 Active Evacuation of Reactor Chamber

The recovery of chamber environment is critical issue of the HIF-GJ reactor. As shown, the first wall is inevitable of the surface ablation due to the prompt energy fluence of fusion products from the micro-

Table 4 Fluences and arrival times of fusion products from the micro-explosion to the first wall.

Energy and Neutron Fluences (R=5m, E_0=2GJ)		
Fusion products	**Arrival**	**Fluence**
X-rays	17nsec	17J/cm^2
Debris & Fast Ions	A few μ sec	80J/cm^2
Neutrons	140nsec	2x10^{14}/cm^2

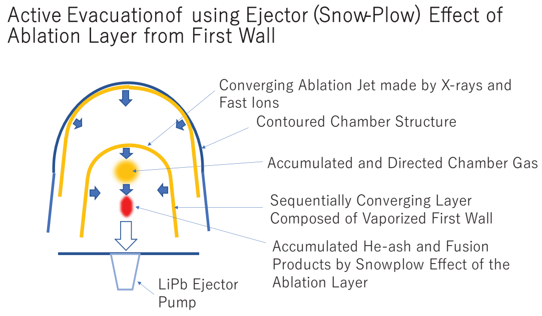

Fig.4 Conceptual sketch of active evacuation using sequentially converging ablation layer from the first wall.

explosion. Table 4 shows the energy and neutron fluences and their arrival times to the first surface from the micro-explosion.

As shown, first come is the X-ray whose energy is below a few keV. The next comes are neutrons and energetic ions from burning fuel. The energetic ions including He-ash should interact nearby the first surface and may remain for more than the repetition period. Without adequate chamber clearing, the fusion products and the ablated materials could result in a chamber environment unsuitable for the beam propagation.

We propose an active evacuation method to remove all of the fusion products, by-products and residual target material. A conceptual sketch of the active evacuation process is shown in Fig.4. As is well known, ablated materials made by explosive boiling expand perpendicular to the surface. As the prompt energy comes from a point source (micro-explosion) far from the first surface, the fluences to the surface is uniform. This means that splashing of the liquid layer due to a localized shock reflection cannot occur easily and the ablation behavior can be controlled by the geometrical structure of the wall.

The rapidly expanding ablated gas is enough dense, therefore, the ablation layer forms a vapor shield that is expected to trap and accumulate the chamber gas. When the wall geometry is properly designed, the directional gas layer will remove the chamber gas together with debris, fast ions, and the target remnant by the snowplow-like active evacuation mechanism

[19]. The accumulated fusion products, target remnants and the wall vapor will be transported to an ejector pump that is followed to a system for the power generation, energy-recovery, LiPb recirculation, and tritium collection.

5. Concluding Remarks

An IFE power system driven by an energetic (massive) heavy ion-beam accelerator was shown. That is based on successive 1Hz/2GJ micro-explosions. The massive multi-bunch ion-beam driver can extend the exploration area of the target structure of ICF. Although, the energetic beam driver is intrinsically advantageous to achieve a more robust implosion scheme of fuel gain, a modest fusion gain (G=50) was expected. The modest value of target gain should increase the steadiness of fusion energy gain.

The electrical conversion (electricity to the beam energy) efficiency of the massive ion accelerator was estimated to be ~ 30%. The efficient accelerator is expected to relieve greatly the criterion of economical assessment as a fusion power system.

In addition to the advantages of HIBs (capability of repetitive operation, high efficiency, robustness and reliability), the massive multiple-beam driver facilitates us to design a practical power plant.

The micro-explosion of 2GJ energy level in the reactor chamber is one of the critical issues of massive ion-beam IFE system particularly recovery of the chamber environment for the beam transport level. To overcome this issue; successive 1Hz operation of the chamber under 2GJ micro-explosion, the author proposed an active evacuation method.

The author would like to point out that the particles (He-ash, Fast ions, DT fuel remnants, Target debris, and Fusion by-products) management and the chamber recovery are common critical issues for all of the fusion reactor systems including magnetically confined fusions [20,21] and high rep-rate laser IFEs. The concept of active evacuation and clearing of reactor chamber could provide a conclusive solution for this critical issue of the fusion reactors.

Acknowledgement

The author would like to express his deepest gratitude to the technical committee members in JSPS for fruitful discussions on the issues of fusion reactor system based on the massive ion-beam driver.

References

[1] A.B.Zylstra et.al., "Record Energetics for an Inertial Fusion Implosion at NIF", *Phys. Rev. Lett.,* **126**, 025001 (2021).

[2] A.B.Zylstra, O.A.Hurricane et.al., "Burning plasma achieved in inertial fusion", *Nature*, **601**, 27 Jan. (2022).

[3] K.Horioka, " Progress in Particle-Beam-Driven Inertial Fusion Research: Activities in Japan " *Matter and Radiation Extremes*, **3**, 12 (2018).

[4] K.Takayama et. al., "A massive-ion beam driver for high-energy-density and future inertial fusion", *Phys. Lett.*, **A 384**, 126692 (2020).

[5] K.Takayama, "Design of the Irradiation Line and Beam Physics Issue at the Final Stage of the Massive Ion ICF Driver", *NIFS-Proc*-**123**, Ed. by J.Hasegawa and T.Ozaki, pp.80-84 (2022).

[6] S.Atzeni and J.Meyer-ter-vhen, "The Physics of Inertial Fusion", *Oxford Univ. Pres*., (2004).

[7] S.Kawata, "Direct-drive heavy ion beam inertial " confinement fusion: a review, toward our future energy source", *Adv. Phys*., **6**, 1, 1873860 (2021).

[8] M.Murakami, "Target Physics of Heavy Ion Inertial Confinement Fusion", *J. Plasma & Fusion Res.*, **77**, 40 (2001).

[9] K.Takayama, "Design of Irradiation Line and Beam Physics Issue at the Final Stage of the Massive Ion ICF", *NIFS-Proc*-**123**, Ed. by J.Hasegawa and T.Ozaki, pp.80-85 (2022).

[10] K.Takayama, Private communication.

[11] K.Horioka, "New area of target structure explored by the massive ion ICF", *NIFS-Proc*-**123**, Ed. by J.Hasegawa and T.Ozaki, pp.72-75 (2022).

[12] K.Horioka and H.Yoneda, "High Power Beam Transport and Design Criterion for Reactor Chambers", *Plasma Fus. Res*., **71**, pp.976-982 (1995).

[13] T.Kikuchi et. al., “Study on Reactor Radius of Heavu-Ion Inertial Fusion”, *NIFS-Proc*-**123**, Ed. by J.Hasegawa and T.Ozaki, pp.85-89 (2022).

[14] Badger et.al., “Preliminary conceptual design of hambersSIRIUS”, *Rep. UWFDM*-**568** (1984).

[15] A.R.Raffray, J.Blanchard, J.Latkowski, et.al., “Progress towards realization of a laser IFE solid wall chamber”, *Fusion Engineering and Design* **81**, pp.1627-1638 (2006).

[16] R.G-Arrabal, A.Rikera, J.M.Perlado, ”Limitations for tungsten as plasma facing material in the diverse scenarios of the Europian inertial confinement fusion facility HiPER: Current status and new approaches”, *Matter and Radiation Extremes*, **5**, 055201 (2020).

[17] M.R.Zaghloul, A.Rene Raffray, “IFE Liquid wall response to the prompt X-ray energy deposition: Investigation of physical processes and assesment of ablated material”, *Fusion Sci. Tech.*, **47**, pp.27-45 (2005).

[18] S.I.Anisimov, B.S.Luk’yanchuk, “Selected problems of laser ablation theory”, Physics-Uspekhi, **45**, p.293 (2002).

[19] K.Adachi, M.Nakajima, K.Horioka, “Control of Taper-pinch Plasma by Geometrical Parameters of Capullary”, *IEEE Trans. Plasma Sci.*, **40**, pp.3308-3312 (2012).

[20] Matsuda, S., et.al., “A Critical Issue Toward Realization of DEMO Fusion Reactor from the Particle Transport Study”, *J. Plasma Fus. Res*., **96**, pp.267-268 (2020).

[21] Motojima, G, “Particle Exhaust in Magnetic Confinement Fusion Plasmas for Particle Control: Past and Future”, *J. Plasma Fusion Res*., **98**, pp.429-438 (2022).

Beam parameters of laser ion source for heavy-ion inertial fusion based on massive-ion beam accelerator

Kazumasa Takahashi

Nagaoka University of Technology, 1603-1 Kamitomioka, Nagaoka, Niigata, 940-2188, Japan

ABSTRACT

A massive-ion beam driver was recently proposed to achieve heavy-ion inertial fusion (HIF). In the driver system, a new accelerator complex was designed to handle 100 heavy-ion beams simultaneously. To realize the scheme, 10 ion sources are employed, and they are required to provide high current ion beams. This study focused on estimating the parameters required for the ion sources when heavy-ions such as Pb^{1+} and Bi^{1+} are used. Additionally, the parameters of the laser ion source, which has been considered a candidate for the ion source used in HIF, were compared with the estimated requirements. The results indicate that laser ion sources have the potential to meet the requirements for the massive-ion beam driver regarding current, pulse duration, and emittance.

Keywords

Laser ion source, Laser ablation, Heavy-ion beam, Heavy-ion inertial fusion, Massive-ion beam driver

1. Introduction

Heavy-ion inertial fusion (HIF) has been expected to be one of the methods to realize power generation by nuclear fusion in future [1-3]. Recently, a new scheme using a massive-ion driver based on induction accelerators has proposed for HIF [4]. In this scheme, the accelerator complex can accelerate not only conventional heavy-ions like Pb and Bi but also cluster ions such as C_{60} and Si_{100}. Furthermore, it enables the operation and simultaneous focusing of 100 beams on the fusion fuel target. The scheme gives us an option for achieving direct drive inertial confinement fusion through uniform beam irradiation on a fuel pellet, which can efficiently induce nuclear fusion.

In the new scheme, 10 ion sources are employed to supply ion beams, and they are essential components for achieving HIF as the same as the other schemes proposed so far. Ion sources are required to provide ion beams with significantly higher current compared to those currently operated in various accelerator facilities. Generally, heavier ions with lower charge-sates are preferred as the HIF driver because they can be focused more tightly on the fuel target for fusion. Moreover, using heavier ions enables to reduce the ion current required for fusion.

To supply such heavy-ion beams in conventional HIF schemes, a laser ion source has been studied as a candidate [5, 6]. It can provide a high current heavy-ion beam from an ablation plasma generated with a pulsed laser irradiation on a solid target. It has been studied since late 1960s for developing ion sources to supply highly charged ions with high current [7-10]. On the other hand, it can also provide low charge-state ions by laser irradiation to a target with low power density. Moreover, techniques for enhancing the current and controlling ion beam characteristics using magnetic fields have been developed [11-16].

The article suggesting the new driver presents beam parameters in the case of using Si_{100} ions [4]. However, the technique to supply cluster ion beams with high current satisfying the requirement of the HIF has not been established. In this study, the beam parameters required for each ion source used in the new accelerator system were estimated based on ions of metal species such as Pb, Bi because providing these ions from a laser ion source has been more established compared to a cluster ion source. The study also discusses the current status achieved with laser ion sources to date to investigate their potential usefulness for the new scheme.

2. Requirement for ion source

The scheme for HIF using the massive-ion beam driver has the capability to focus 100 ion beams on a fuel target with a total energy of 40 MJ. While the energy value was originally calculated based on cluster ion beams, it was noted that there is no problem using Pb or Bi ions instead. The HIF requires singly charged ions because ion beams with lower charged ions are easier to focus on the fuel target due to the smaller space charge generation. The total number of ions required for each fusion is approximately 2.8×10^{16}. This number can be obtained by dividing the beam energy of 40 MJ by the energy of individual ions of 9 GeV = 1.44 nJ, which is typical value to deposit a beam energy into the fuel target in the case of using Pb or Bi ions.

Figure 1 shows the schematic of the permanent magnet stacking ring used for the massive-ion beam driver composed of an induction synchrotron accelerator complex. The ring can stack beams of 100 super bunches, and each super bunch composed of four bunches supplied from an ion source. After staking 100 ion beams, they are transferred to the main accelerator located under the stacking ring. Therefore, the number of ions that should be supplied from a single ion source is 7×10^{13} per pulse. The scheme aims to operate fusion reactions with a frequency of 1 Hz in a fusion reactor, therefore the required frequency of the beam supply is 40 Hz to provide 40 bunches per 1 s.

As injectors for providing ion beams to the stacking ring, induction microtron accelerators are employed as illustrated in Fig. 1. For the injection from the ion source to the induction microtron, one-turn injection using an electrostatic injection kicker will be used. Assuming that the injected beam from the ion source occupies half of the orbit in the microtron, the bunch length of the beam should be 24 m. With an ion injection energy of 1 MeV from the ion source to the microtron, the maximum pulse duration is estimated to be 25 μs based on the ion velocity and beam length. Based on the number of ions per beam bunch (7×10^{13}) and the pulse duration (25 μs), the required beam current supplied from the ion source is calculated to be 450 mA. These obtained values are similar to those aimed in the scenario using linear induction

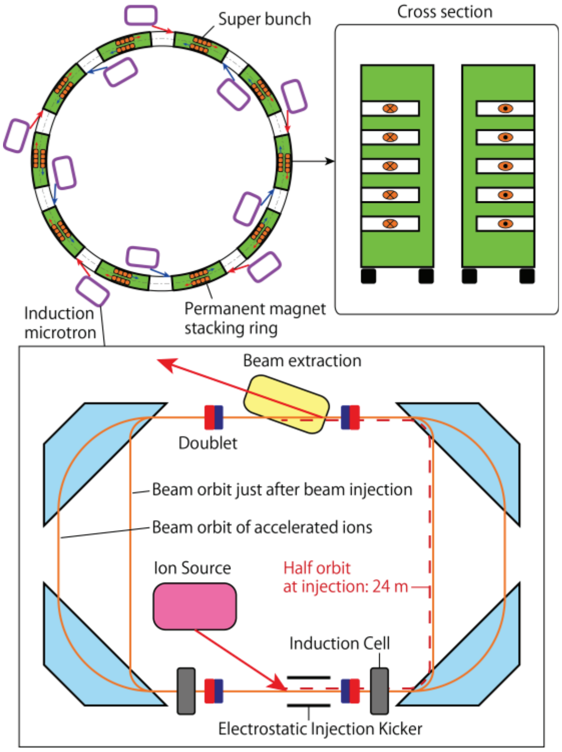

Fig. 1 Schematic view of the stacking ring used for induction synchrotron accelerator complex (top) and a microtron accelerator as the injector of ion beam for the induction synchrotron (bottom). This figure is illustrated based on Ref. [4].

Table 1 Parameters required for ion source

Ion number per pulse	7×10^{13}
Pulse duration	25 μs
Current	450 mA
Normalized RMS emittance	5 mm-mrad
Frequency of beam supply	40 Hz
Ion species	Pb^{1+}, Bi^{1+}

accelerators [17].

Furthermore, the normalized RMS emittance of the supplied beam is required to be about 5 mm-mrad. This value is essential not only for beam focusing onto the fuel target (~several mm) but also for beam loss suppression within the main ring accelerator. The specifications for the ion source requirements are summarized in Table 1.

3. Specification of laser ion source

To satisfy the requirements for ion sources, the use of laser ion sources was considered. Figure 2 shows the schematic of a laser ion source, and Fig. 3 indicates a typical waveform of ion beam current obtained with a laser ion source. A laser ion source has an advantage of supplying ion beams with high current densities extracted from high-density plasma generated by laser ablation from a solid target. Generally, the ion current supplied from the ion source is limited by the Bohm current, in which the ion velocity is determined as a function of the electron temperature in a plasma. However, in the laser ion source, the plasma has a drift velocity v_d in a direction perpendicular to the target surface significantly larger than the thermal ion velocity, allowing the extracted ion beam current density [18]:

$$J_i = Zen_iv_d, \quad (1)$$

where, e represents the elementary charge, Z and n_i are the charge-state and the number density of ions, respectively.

In order to develop a laser ion source, a laser with an energy of about 0.1-1 J and a pulse duration of about 10 ns is commonly used. To supply singly charged ions from a laser ion source, the laser power density on the solid target is controlled to be around 10^8-10^9 W/cm^2, which is slightly above the ablation threshold of metals [19]. The number of supplied ions can be increased by expanding the irradiation area while maintaining the laser power density.

For ion species such as Bi^+ and Au^+, the capability of generation and supply of beams with a pulse width of 20 μs (FWHM), a current density of 100 mA/cm^2 or more, and an emittance ~ 0.1 mm-mrad have already been indicated at the Brookhaven National Laboratory (BNL) in USA using a laser ion source [6]. The results indicated the laser ion sources will satisfy the specifications in Table 1 by adjusting the beam extraction diameter and the plasma transport distance. In addition, the use of a solenoidal magnetic field is effective to confine the ablation plasma during the transport and increase the ion density at the position for beam extraction [11-16].

To satisfy the requirements for the number of supplied particles while keeping the peak current low to suppress the enhancement of space charge effects, a rectangular waveform for the ion current is desirable. Such a beam shape can be obtained by expanding the ablation plasma to a pulse duration longer than 25 μs and then chopping it out. A waveform control by applying a pulsed magnetic field could also be useful to make such a waveform [20, 21].

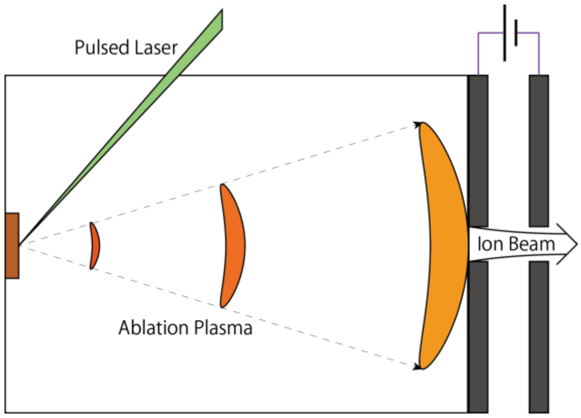

Fig. 2 Schematic of a laser ion source.

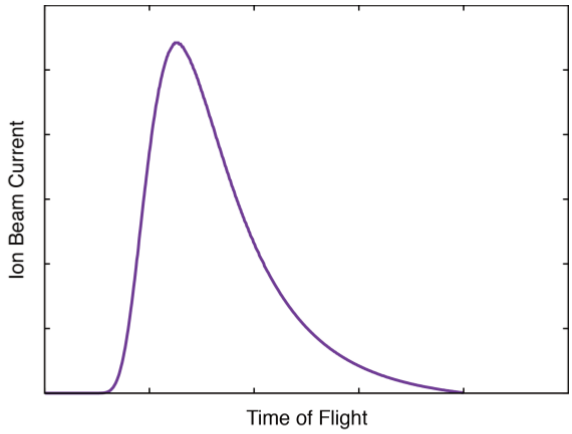

Fig. 3 Typical waveform of ion beam current extracted from a laser ion source.

The proposed driver accelerator system requires 40 Hz operation, but there is currently no operational experience with a laser ion source at this repetition rate. The laser ion source at BNL has been operated at 5 Hz. Although achieving 40 Hz laser operation is possible with commercially available lasers, resolving the issue of the solid target lifetime requires further research and development. An alternative idea is to employ liquid metal for the laser target to develop a laser ion source with a long-life target. The research on this topic is currently underway [22], and future researches are expected.

4. Conclusion

This study aimed to investigate the parameter requirements of the ion source in the new HIF scheme based on the massive-ion beam driver. The parameters of the laser ion source developed to date was also investigated to discuss the feasibility to apply a laser ion source to the beam driver. The required parameters for HIF were estimated based on the case using Bi^{1+} or Pb^{1+} ions. The estimated current and pulse duration are 450 mA and 25 μs, respectively. In addition, the requirements for emittance and frequency are 5 mm-mrad and 40 Hz, respectively. The results indicate that the current, pulse duration, and emittance of the laser ion source obtained so far satisfy the required values. The development of targets in the laser ion source for high-repetition continuous operation should be studied further.

References

[1] R.O. Bangerter *et al.*, Rev. Accel. Sci. Tech. **6**, pp. 85–116 (2013).

[2] I. Hofmann, Matter Radiat. Extremes **3**, pp. 1–11 (2018).

[3] K. Horioka, Matter Radiat. Extremes **3**, pp. 12–27 (2018).

[4] K. Takayama *et al.*, Physics Letters A, **384**, 126692 (2020).

[5] J. Hasegawa *et al.*, Nucl. Instrum. Meth. Phys. Res. B, **161-163**, pp. 1104-1107 (2000).

[6] M. Okamura *et al.*, *Nucl. Instrum. Meth. Phys. Res. A* **733**, pp. 97-102 (2014).

[7] B.Y. Sharkov *et al.*, Matter Radiat. Extremes **1**, pp.28–47 (2016).

[8] I.V. Roudskoy, Laser Part. Beams **14**, pp. 369–384 (1996).

[9] V. Dubenkov *et al.*, Laser Part. Beams **14**, pp.385–392 (1996).

[10] H. Haseroth, H. Hora, Laser Part. Beams **14,** pp. 393–438 (1996).

[11] L.G. Gray *et al.*, J. Appl. Phys. **53,** 6628 (1982).

[12] J. Wołowski *et al.*, Rev. Sci. Instrum. **75**, 1353 (2004).

[13] M.Okamura *et al.*, Rev. Sci. Instrum. **81,** 02A510 (2010).

[14] S. Ikeda *et al.*, Rev. Sci. Instrum. **87**, 02A915 (2016).

[15] S. Ikeda *et al.*, Rev. Sci. Instrum. **87**, 02A912 (2016).

[16] K. Takahashi *et al.*, AIP Conf. Proc. **1525**, 241 (2013).

[17] J. W. Kwan, IEEE Trans. Plasma Sci. **33**, 1901 (2005).

[18] M. Dembinski, P. K. John, J. Appl. Phys. **50**, 6113–6116 (1979).

[19] T. Kanesue *et al.* Proc. EPAC08 (Genoa, Italy) 421 (2008).

[20] K. Takahashi *et al.*, Rev. Sci. Instrum. **91,** 033310 (2020).

[21] M. Sekine *et al.*, Nuclear Instruments and Methods in Physics Research A **795**, pp. 151–155 (2015).

[22] K. Takahashi *et al.*, NIFS-PROC-123, pp. 63–66 (2022).

Evaluation of Beam Loss in Massive Ion Driver Accelerator

Jun Hasegawa

Tokyo Institute of Technology

Ken Takayama

High Energy Accelerator Research Organization (KEK)

ABSTRACT

Possible beam losses in a massive ion driver (MID) accelerator, which has been proposed as an energy driver for heavy-ion inertial fusion, were evaluated. The ionization and recombination reactions of lead or bismuth ions due to collisions with background gas molecules in the beam duct and mutual collisions between ions in the beam bunch were considered. The results show that a pressure of less than 10^{-9} Pa is required to reduce the beam loss due to collisions with background molecules to less than 1%. In the design of 40-MJ MID driver, the beam loss rate due to inter-ion collisions in the main ring was predicted to be ~3.5%, suggesting that severe activation of accelerator components may be induced.

Keywords

Beam Loss, Induction Synchrotron, Charge Exchange, Ion Impact Ionization

1. Introduction

One of the key issues in the acceleration of heavy ion beams is the charge conversion of the accelerated ions due to collisions with residual gas molecules and the resulting beam loss. In conventional high-energy accelerators, ions are generally accelerated to high energy over the shortest distance in a linear accelerator and then injected into a subsequent accelerator such as a synchrotron. On the other hand, the Massive Ion Driver (MID) accelerator [1] proposed as an energy driver for heavy ion inertial fusion (HIF) uses induction microtrons [2] as injectors, which significantly increases the flight distance of the ions due to circumferential acceleration. Obviously, this imposes severe restrictions on the background pressure in the beam duct of the induction microtron.

In addition to beam loss due to collisions with residual gas, beam loss caused by charge conversion of ions due to collisions between ions in beam bunches also becomes a major issue as beam intensity increases. This beam loss process is unavoidable in principle and imposes intrinsic constraints on the beam parameters of the driver accelerator.

The purpose of this study is to evaluate beam losses due to the above two loss mechanisms based on the beam parameters of the MID accelerator and to discuss the feasibility of the MID in terms of activation of the beam duct of the accelerator.

2. Configuration and beam parameters of MID accelerator

The MID accelerator is schematically illustrated in Fig. 1 (see Ref. [1] for details). It consists of 10 induction microtrons, 10 stacked storage rings, and 10 stacked main rings. Each main ring simultaneously accelerates 10 ion bunches and provide them to final beam transport lines to the reactor. Therefore, 100 heavy ion beams are available for heating and compressing a fuel pellet for inertial confinement fusion reactions. This feature is a significant advantage in terms of illumination uniformity of the fuel pellet. The beam parameters of the MID accelerator are

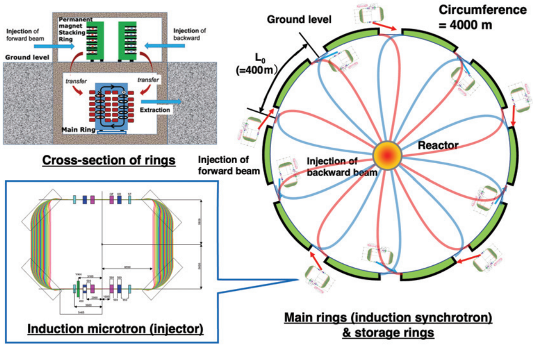

Fig. 1 Configuration of MID accelerator.

Table 1 Beam parameters of MID accelerator.

Circumference	C_0 (m)	4000
Bending magnet field (ramp time 0.5 s)	B (T)	0.05-1.5
Orbital radius	ρ (m)	224.3
Betatron tune	Q_x/Q_y	25.91/25.22
Acceleration cycle	f (Hz)	1
Accelerating voltage per circulation	V_{acc} (MV)	2.6
Accelerated ions (Pb^+/Bi^+)	A	207/209
	Q	1
Energy gain in main rings	E_{inj} (GeV)	0.026
	E_{final} (GeV)	9
Number of ions injected to a storage ring	N_0	6.8×10^{12}-6.8×10^{13}
Number of ions per bunch	N_b ($=4N_0$)	2.7×10^{13}-2.7×10^{14}
Number of beam bunches	N_{beam}	100
Total number of ions	$N=N_b\times N_{beam}$	2.7×10^{15}-2.7×10^{16}
Total beam energy	$E_{tot}=N\times E_{final}$ (MJ)	~4-40 (*)

summarized in Table 1. In the beam loss calculations, 4 MJ and 40 MJ were assumed as the total beam energy.

3. Beam loss due to charge exchange with background residual gas

Figure 2 shows ionization and electron capture cross-sections of $^{208}Pb^+$ ions in H_2 as background residual gas. Here, the ionization cross section σ_{BEM} ($Pb^+ + H_2 \rightarrow Pb^{2+} + H_2 + e$) was calculated using the binary-encounter model (BEM) by Gryzinski *et al* [3]. The bound-electron-capture cross section σ_{CT} ($Pb^+ + H_2 \rightarrow Pb^0 + H_2^+$) was calculated using the Oppenheimer-Brinkmann-Kramers (OBK) theory [4-6]. As shown in

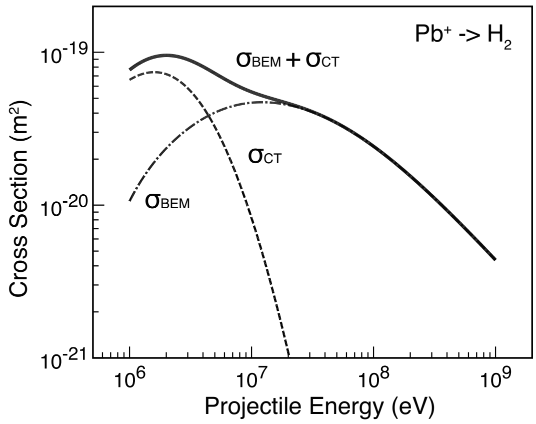

Fig. 2 Ionization and electron capture cross-sections of $^{208}Pb^+$ in H_2.

the figure, bound electron capture is dominant at relatively low projectile energies (<10 MeV), but collisional ionization becomes dominant at higher energies above 10 MeV. Once ions changed their valences, they depart from their stable orbits and eventually collide with the inner wall of the beam duct, where they are lost. Therefore, the cross section of beam loss due to collisions with the background gas is given by the sum of these cross sections (solid line in the figure).

Figure 3 shows the calculated beam loss as a function of the background pressure of the beam duct. The injection energy of ions into the induction microtron is 1 MeV, the extraction energy is 26 MeV, and the acceleration voltage per revolution is 10 kV. The vertical axis is the ratio of the outgoing beam intensity to the incoming beam intensity. One can see

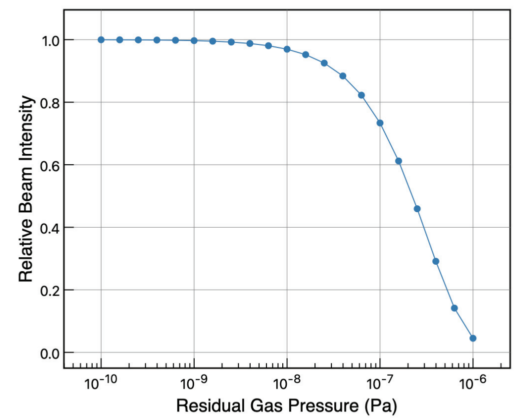

Fig. 3 Dependence of beam loss rate in the injector on background gas pressure.

that a pressure of less than 10^{-9} Pa is required to suppress the beam loss to less than 1 %. Compared to typical proton synchrotrons, the required pressure is one to two orders of magnitude lower, but still possible with existing technology.

3. Beam loss due to mutual ion collisions in a beam bunch

Here, Bi is assumed as the accelerating particle. The charge exchange cross section σ_c ($Bi^+ + Bi^+ \rightarrow Bi^0 + Bi^{2+}$) and the ion impact ionization cross section σ_i ($Bi^+ + Bi^+ \rightarrow Bi^+ + Bi^{2+} + e$) for Bi^+ measured by Budicin *et al.* are shown in Fig. 4 [7]. In charge exchange collision, the charges of both ions involved in the collision change, so that they are deviated from stable orbits and lost. In ion impact ionization, only one of the ions is lost. If we consider the case where the incident and target particles are interchanged, the beam loss cross section is given by $\sigma_L = 2(2\sigma_c + \sigma_i)$. s shown in the figure, the beam loss cross section increases monotonically with energy when the relative energy of ions in the beam center-of-mass system is in the range of ~10-50 keV.

The collision rate between ions in the beam bunch is given by [Ref.] as follows:

$$R(t) = \frac{N^2(t)\langle\sigma_L v\rangle}{2\pi\epsilon_{RMS}(\beta_H(t)\beta_V(t))^{1/2} l_b \gamma}$$

where N is the number of ions in the beam bunch, v is the ion relative velocity, ϵ_{RMS} is the normalized RMS emittance, $\beta_H(t)$ and $\beta_V(t)$ are the horizontal

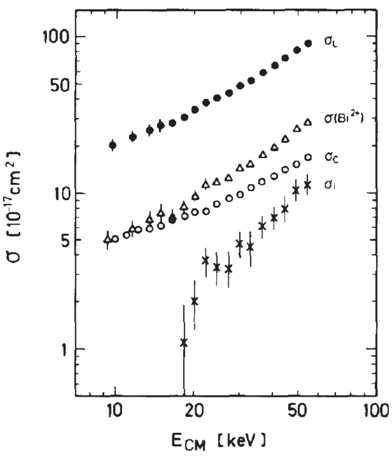

Fig. 4 Charge transfer and ion impact ionization cross sections between Bi (reproduced from [7]).

Table 2 Beam parameters used for beam loss calculation.

	Storage ring	Main ring
ϵ_{RMS} (m)	10^{-6}	10^{-6}
E_{kin} (GeV)	0.026 → 0.026	0.026 → 9
$\beta(t)$	0.016	0.016 → 0.29
Q_H	25.9	25.9
N	2.7×10^{13}~2.7×10^{14}	2.7×10^{13}~2.7×10^{14}
$\bar{\beta}_H, \bar{\beta}_V$ (m)	22	22
l_b (m)	350	350 → 17.5 (after bunching)

Table 3 Calculated beam loss rates.

Number of ions per bunch	Storage ring	Main ring	Bunching process
2.7×10^{13}	2.3×10^{-5}	3.6×10^{-3}	2.1×10^{-4}
2.7×10^{14}	2.3×10^{-4}	3.5×10^{-2}	2.1×10^{-5}

and vertical beta functions, l_b is the bunch length, and γ is the Lorentz factor. The reaction rate coefficient $\langle\sigma_L v\rangle$ is obtained assuming that the relative velocity distribution of ions is given by the Maxwellian distribution with temperature kT_{tr}, where kT_{tr} is the transverse beam temperature given by

$$kT_{tr} = E_{kin}\epsilon_{RMS}Q_H/\bar{R},$$

where E_{kin} is the beam energy, Q_H is the betatron tune, and $\bar{R}$ is the mean radius of the ring. The values used in the calculations for the storage and main rings are summarized in Table 2. The beam emittance affects the transverse temperature, which in turn significantly changes the rate coefficient. Here the normalized RMS emittance is assumed to be 10^{-6} m. The number of particles per bunch is assumed to be 2.7×10^{13} and 2.7×10^{14} for 4 MJ and 40 MJ scale driver accelerators, respectively. The beta function actually varies within the ring, but was estimated using the average value.

Using the values in Table 2, the total beam losses, which is defined as the ratio of the number of particles lost due to charge conversion to the number of incident particles, were calculated for the storage and acceleration processes in the rings and the final beam bunching process in the main ring. Table 3 summarizes the results. The beam loss during orbital acceleration in the main ring is more than one order of magnitude larger than the others, reaching a maximum of about 3.5%. This is because the number of beam revolutions in the main ring is about 3500, which is relatively large compared to others, and the reaction rate increases with beam energy due to the increase in lateral temperature. This result indicates that most of the beam loss due to in-beam ion collisions occurs in the main ring.

Considering that 10 super bunches are accelerated simultaneously in the main ring, the beam loss power per unit length in the main ring (the average power imparted by the beam particles to the beam duct wall divided by the circumference) is about 0.21 W/m for a 4 MJ driver and about 20 W/m for a 40 MJ driver. In general, high-energy accelerators (mainly proton synchrotrons) require a beam loss power of less than 1 W/m to ensure machine maintenance. The former falls within this standard, but the latter greatly exceeds. Since the activation mechanism of the beam duct and surrounding structures is different for protons from those for heavy particles such as Bi and it also depends on the particle energy, it is somewhat crude to simply apply the same criteria to the MID accelerator. But it is quite sure that in the case of 40 MJ drivers, the activation level around the main ring can be quite severe from a viewpoint of machine maintenance. This study estimated the beam loss due to intra-beam ion collisions for Bi^+ ions because the cross-sectional area data are available. Since the atomic number of Pb is very close to Bi, it is thought that the results are almost the same for Pb beams.

4. Concluding remarks

In designing a new concept of a heavy-ion inertial confinement fusion reactor based on circular induction accelerators, possible beam losses in the driver accelerator were evaluated. In the injectors (induction-accelerated microtrons), where the beam is relatively low-energy, the vacuum requirements are more stringent than before because of the large number of revolutions and the long flight distance (~20 km). A vacuum of $\sim 10^{-9}$ Pa is required to limit beam loss to less than 1%. On the other hand, the beam loss due to charge transfer and collisional ionization caused by mutual collisions between accelerated ions in the beam bunch is more pronounced during beam acceleration in the main ring of the driver accelerator. In the case of the 40 MJ driver, the beam loss was found to reach 3.5%. The average beam load on the beam duct wall is expected to be about 20 W/m, which is much higher than the upper limit of 1 W/m for the beam load in conventional proton accelerators. More detailed studies of duct wall activation by energetic heavy ions and development of maintenance techniques under high-dose environments will be required.

References

[1] K. Takayama *et al*., “A massive-ion beam driver for high-energy-density physics and future inertial fusion”, *Phys. Rev. A*, **384**, 126692 (2020).

[2] K. Takayama *et al.*, “Racetrack-shape fixed field induction accelerator for giant cluster ions”, *Phys. Rev. ST Accel. Beams*, **18**, 050101 (2015).

[3] M. Gryzinski, “Two-Particle Collisions. I. General Relations for Collisions in the Laboratory System”, *Phys. Rev. A*, **138**, 305 (1965); “Two-Particle Collisions. II. Coulomb Collisions in the Laboratory System of Coordinates”, *ibid*., **138**, 322 (1965); “Classical Theory of Atomic Collisions. I. Theory of Inelastic Collisions”, *ibid*., **138**, 336 (1965).

[4] J. R. Oppenheimer, “On the Quantum Theory of the Capture of Electrons”, *Phys. Rev.*, **31**, 349 (1928).

[5] H. C. Brinkmann and H. A. Kramers, “Zur Theorie der Einfangung von Elektronen durch α-Teilchen”, *Proc. Kon. Ned. Akad. Wet.* **33**, 973 (1930).

[6] J. K. M. Eichler and F. T. Chan, “Approach to electron capture into arbitrary principal shells of energetic projectiles”, *Phys. Rev. A*, **20**, 104 (1979); J. K. M. Eichler, A. Tsuji, and T. Ishihara, “Eikonal theory of charge exchange between arbitrary hydrogenic states of target and projectile”, *ibid.*, **23**, 2833 (1981).

[7] D. Budicin *et al.,* “Beam loss in heavy-ion fusion accelerators due to charge exchange scattering”, *Nuov Cim A*, **106**, 1621–1630 (1993).

Outline for Issues and Status of Reactor and Peripheral Equipment Systems

Takashi Kikuchi

Nagaoka University of Technology

ABSTRACT

A reactor design concept for heavy–ion inertial fusion is to follow a laser fusion reactor design. The reactor and the peripheral equipments are almost same as the laser fusion reactor. The issues and status for the reactor and the peripheral equipment systems are summarized in comparison to the laser fusion system. Also the unique and common points for the reactor design in heavy–ion inertial fusion are discussed.

Keywords

Reactor Wall, Blanket, Liquid Loop, Vacuum Vessel, Exhaust System, Target Manufacturing, Target Injection, Final Focus, Steam Cycle, Intermediate Heat Exchanger, Facility, Maintenance

1 Introduction

The reactor design concept for heavy–ion inertial fusion (HIF) is to follow the laser driven inertial confinement fusion (ICF) reactor design [1,2]. The fuel target structure for HIF is different from one for the laser fusion because of the difference in the energy deposition processes into materials for ions and for photons. Of course, the energy driver for HIF is quite different device from one for the laser fusion. However the reactor and the peripheral equipments are same as the laser fusion system. The issues and status for the reactor and the equipment systems are summarized in comparison to the laser fusion system.

2 Unique and Common Points for Reactor Design of Heavy–Ion Inertial Fusion Compared with Other Nuclear Fusion Reactor Systems

HIF is an ICF method that uses intense heavy–ion beams as an energy driver. Therefore, the reactor system has many similarities and common issues with laser fusion reactors. In addition, because the energy output from ICF occurs in an extremely short period of time, it is characterized by an instantaneous high load on the reactor wall [1, 2]. On the other hand, it can also be a common parameter with he high load on the reactor wall at edge–localized mode and disruption in magnetic confinement fusion (MCF) systems. Issues considering as reactor and peripheral equipment components are as follows.

- First wall
- Blanket
- Fuel recovery system
- Liquid loop system
- Intermediate heat exchanger
- Vacuum vessel
- Fuel target production
- Target injection
- Beam final focus and transport
- Power generation equipment

- Engineering safety equipment
- Vacuum system
- Maintenance

For the first wall, a solid wall is mainstream in MCF reactors. Although there are also reactor designs with solid walls in ICF reactors, reactor designs using liquid metal are mainstream. It is the same for HIF reactors.

To name a few issues unique to HIF reactors, a higher degree of vacuum is required than in laser fusion reactors to propagate the heavy–ion beams within the reactor [3]. For this reason, it is necessary to be careful about beam instability and quality degradation inside the reactor, and the vacuum pump system is required to have the ability to maintain a low pressure inside the reactor [4].

For the fuel system, the basic concept of fuel target production and target injection system is the same as that of laser fusion. However, the fuel target structure and materials are unique to HIF, so they cannot be exactly the same.

As an engineering safety equipment, HIF requires a heavy ion accelerator to generate an intense heavy–ion beam, and its large site area is a disadvantage. Radio–activations in the reactor and the fuel system are common issues not only in HIF but also in nuclear fusion power generation systems. Although the dose and radioactivity are expected to be low, the site of heavy–ion accelerator is wide area. The radio–activation of particle accelerator will be a particular and unique concern. On the other hand, not only other types of nuclear fusion power generation systems but also other existing various power plants as well, the site area is not determined solely by the power generation section. Consequently a comprehensive study is required.

3 Summary for Issues and Status of System Components

HIF is a type of inertial confinement system and is a reactor system that uses intense heavy–ion beams as an energy driver. It has the advantage of allowing flexible design of fuel targets by utilizing the characteristic energy deposition process in the interaction between heavy ions and target materials [5]. The reactor system has similarities and common issues with laser fusion reactors, such as a device to absorb the pulsed fusion output released in an extremely short period of time. On the other hand, since the heavy–ion beam is used as an energy driver, there are unique issues that do not arise with laser fusion reactors. In this study, we will examine characteristic and unique problems regarding HIF reactor systems.

The component, element, problem, analogy, and status are summarized in Table 1 for the reactor chamber issues, in Table 2 for issues in the reactor related to ion beam and the fuel system, in Table 3 for issues in the power generation equipment, engineering safety, and maintenance systems, respectively.

The "analogy" means the analogy to the issue for laser driven ICF [6, 7]. The "same" is that the laser fusion reactor has the same issue. On the other hand, the "different" is that the issue has different condition in comparison to the laser fusion reactor, and the "unique" is that the issue is unique characteristics in this reactor system. In the reactor chamber issue as shown in Table 1, the exhaust system for HIF is different from the laser fusion reactor due to the higher level of the vacuum condition. In the issues for the reactor related to the ion beam and the fuel system as shown in Table 2, the final focus component in this reactor is a unique feature due to the use of heavy–ion beams as the energy driver. In the issues for the power generation equipment, the engineering safety, and the maintenance systems as shown in Table 3, the radio–activation of particle accelerator is a unique problem in the HIF system.

Since HIF has many things in common with laser fusion, many of the items studied for laser fusion reactors can be applied. For this reason, the following issues can be considered that are unique to HIF reactors within the scope of treating them as reactor systems.

- Beam transport in reactor chamber
- Vacuum system
- Beam port protection
- Radio–activation of particle accelerator

Table 1: Reactor chamber issues

Component	Element	Problem	Analogy	Status
Reactor Wall	first wall, liquid metal wall, structural material	weakening, tritium capture, liquid flow stability, radioactivity	same	not yet
Blanket	blanket material, coolant, radiation shield, tritium breeder, energy multiplication	material property data under irradiation, optimization for coolant condition, heat removal from liquid wall, wettability data	same	good
Liquid Loop	fuel cycle, tritium recovery, isotope separation, heat exchanger, circulation pump, purification equipment	tritium confinement in high temperature, reasonable separation method, proof–of–principle for hydrogen isotope separation with tritium, continuous circulation operation, liquid metal pump, purification	same	good
Vacuum Vessel	vessel structure, vessel material	estimation by building a real scale model	same	no problem
Exhaust System	vacuum pump, exhaust gas purification equipment	liquid metal diffusion pump, isotope separation	different	not yet

Table 2: Issues for reactor related to ion beam and fuel system

Component	Element	Problem	Analogy	Status
Target Manufacturing	initial tritium loading, target production, fuel layer formation, production quantity	tritium recovery, tritium purification, lower density material, surface coating, assembly, inspection technology	almost same	not yet
Target Injection	transfer, injection, tracking, shutter	lower temperature, injection device, tracking method, reactor system design	same	under consideration
Final Focus	beam window, beam propagation	magnetic coil protection for radiation shield, vacuum level, beam instability, beam quality degradation	unique	under consideration

Table 3: Issues for power generation equipment, engineering safety, and maintenance systems

Component	Element	Problem	Analogy	Status
Steam Cycle	2nd loop, steam generator, turbine power generator	nothing special	same	done
Intermediate Heat Exchanger	heat exchanger	tube material for intermediate heat exchangers, corrosion testing of liquid metal, liquid metal–water reaction	same	almost done
Facility	reactor building, particle accelerator	radio–activation in reactor, radio–activation in particle accelerator	unique	under consideration
Maintenance			same	under consideration

First, since the heavy–ion beam is transported into the reactor toward the fuel pellet, care must be taken to avoid degradation of beam quality due to collisions with residual gas. For this reason, a higher degree of vacuum is required within the reactor than in a laser fusion reactor, and the vacuum pump system is required to have the ability to maintain a lower pressure within the reactor [4]. However, if the pressure inside the reactor chamber is lowered too much, the liquid metal used to protect the reactor walls will evaporate [8]. For this reason, it must be set higher than the vapor pressure of the liquid metal.

In order to protect the beam port and the final optical system from alpha particles produced by nuclear fusion reactions, a method is being considered that installs a coil at the tip of the beam port and uses the coil's magnetic field to protect it [9]. When applying a similar system to an HIF reactor, it is necessary to start up the magnetic field after the heavy–ion beam passes through the port so that the beam trajectory is not affected by the magnetic field protecting the beam port.

Reactor activation and fuel radioactivity are common issues not only in HIF but also in nuclear fusion power generation. On the other hand, although the dose and radioactivity are expected to be low, the activation of heavy ion accelerators, which will be installed over a wide site area, is a particular concern. There is an activation problem caused by the particle loss that occurs during transport of heavy–ion beams with high currents and hits the walls of the vacuum chamber of the particle accelerator. We are evaluating radioactive isotopes generated by the assumed activation of a vacuum vessel [10] and the possibility of activation with respect to the kinetic energy of heavy ions using reaction cross sections [11]. It has been shown that there are no problems in the low kinetic energy region of the particle accelerator complex.

4 Conclusion

Since the reactor and the peripheral equipments were almost same as the laser fusion reactor, the reactor design concept for HIF is to follow the laser fusion reactor design. The issues and status for the reactor and the peripheral equipment systems were summarized in comparison to the laser fusion system. Also the unique and common points for the reactor design in HIF were discussed. It was indicated that the beam transport in the reactor chamber, the vacuum system, the beam port protection, the radio–activation of particle accelerator were unique points and developing issues in HIF reactor design.

References

[1] S. ATZENI and J. MEYER-TER-VEHN, *The Physics of Inertial Fusion: Beam Plasma Interaction, Hydrodynamics, Hot Dense Matter* (Oxford Univ., N.Y., 2004).

[2] S. PFALZNER, *An Introduction to Inertial Confinement Fusion (Series in Plasma Physics)* (CRC Press, 2006).

[3] A.B. LANGDON, *Particle Accelerators* **37-38**, pp.175∼180 (1992).

[4] T. KIKUCHI, Y. UCHIDA, M. NAKAMURA, Y. KAJIMURA, and K. HORIOKA, *NIFS–PROC* **123**, pp.85∼89 (2023).

[5] T. SASAKI, *in this proceedings.*

[6] *Conceptual Design for Fast Ignition Laser Fusion Power Plant* (ILE, Osaka Univ. and IFE Forum, 2006) (in Japanese).

[7] Y. MORI, *et. al.*, *J. Plasma Fusion Res.* **97**, pp.352∼364 (2021) (in Japanese).

[8] D. MARTELLI, A. VENTURINI, and M. UTILI, *Fusion Eng. Design* **138**, pp.183∼195 (2019).

[9] Y. KAJIMURA, *et al.*, *J. Plasma Fusion Res. Series* **8**, 1248 (2009).

[10] S. FUJITA, *et al.*, *Plasma Fusion Res.* **16**, 2404022 (2021).

[11] S. FUJITA, *et al.*, *High Energy Density Phys.* **37**, 100848 (2020).

Characteristics of reactor in heavy ion inertial fusion compared with magnetic confinement fusion

Yuki Uchida

National Institute of Technology, Nagaoka College, Japan

ABSTRACT

An energy balance irradiating to the reactor wall and candidate materials were investigated in a massive-ion beam inertial confinement fusion (MIBICF) and compared with those in magnetic confinement fusion systems. We describe that liquid walls were adopted in inertial confinement systems (laser and MIBICF systems) since the instantaneous load is severe. However it is a problem that the handling of the ceiling and beam port areas, which are difficult to cover with liquid. Then, damages to solid walls that have been investigated in magnetic confinement fusion systems are explained. The damage to those solids will also be an issue for some of the heavy ion fusion reactor walls.

Keywords

Massive Ion Beam Inertial Confinement Fusion, Liquid Wall, Dry Wall

1. Introduction

In 2020, a new massive-ion beam inertial confinement fusion (MIBICF) system was proposed by K. Takayama *et al.* [1], and a committee was established to study the conceptual design of this system. The design of the reactor system requires the determination of the wall material in contact with the plasma and an understanding of severe irradiation damage. In this study, we compared MIBICF with magnetic confinement fusion systems which have been studied historically, focusing on the reactor wall. Parameters irradiated to the reactor wall in each confinement method were scrutinized, and candidate reactor wall materials were compared.

2. Energy balance

2.1 Magnetic confinement fusion

For comparison with the inertial confinement fusion, the energy balance in the magnetic confinement fusion is described. Figure 1 shows the energy balance of the plasma in a typical DEMO reactor [2-6]. A total of ~500 MW of power is transported in the form of particles and X-rays. The divertor is one of the key components, and the heat flux is not expected to exceed 10 MW/m^2 for a water-cooled system in the DEMO reactor with a ratio between the major radius R and the minor radius a, R/a = 5.8/1.45. The heat load to the reactor wall is estimated to be 1 MW/m^2 in total for radiation losses and ripple losses. The structure of the divertor is a combination of tungsten, copper, and a cooled tube made of ferrite steel like ITER. CFC (Carbon Fiber Composite) was not used for the plasma

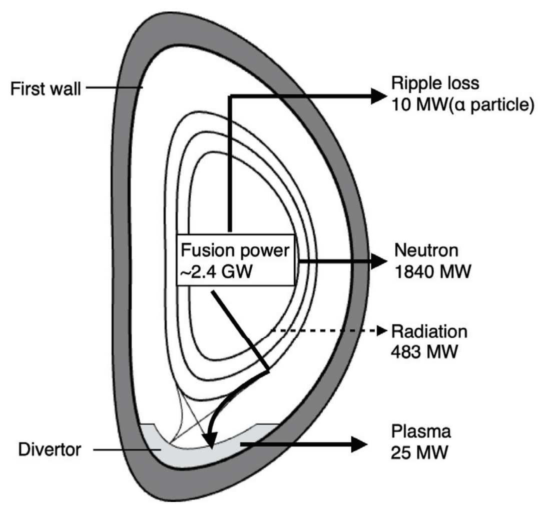

Fig. 1 Energy balance of plasma in a typical Demo reactor [2].

Table 1 Comparison of energy balance for each confinement system. Parameters of HiPER reactor denote the laser based inertial confinement fusion [7], MIBICF denotes massive ion beam inertial confinement fusion, and DEMO denotes magnetic confinement fusion [1].

	HiPER reactor			MIBICF			DEMO (Magnetic confinement)			
Parameter	Ion	X-ray	Neutron	Ion	X-ray	Neutron	Energetic ion	Plasma	X-ray	Neutron
Fragment [%]	Burn:12.7 Debris: 14.4	1.4	70.8	5	25	70	0.4	1	21	80
Power [MW]	Burn: 200 Debris: 200	20	1000	150	750	2100	10	25	483	1840
Peak power[MW]	Burn: 30×10^7 Debris: 10×10^7	2×10^{10}	2×10^9	2.5×10^8	7.5×10^{12}	3.5×10^{10}	-			
Power per unit area [MW/m^2]	Burn: 0.4 Debris: 0.4	0.04	2	1.3	6.6	18.6	-			
Total power [MW]	1540			3000			2300			

facing component (divertor and first wall) to decrease tritium retention. Thus, ferrite steel, or covered ferrite steel by tungsten layer is a candidate of plasma facing material. Tungsten armor is desirable in terms of erosion resistance and protection of the reactor wall, but there are concerns about high Z contamination to the plasma and decreasing tritium breeding ratio (TBR).

2.2 Inertial confinement fusion

Fig. 2 shows energy balance of HiPER reactor [7] as laser based inertial fusion and MIBICF reactor and Table 1 shows comparison of energy balance for each confinement system. In the HiPER reactor, it is assumed that the chamber radius is 6.5 m, the shot energy (power of nuclear fusion reaction) is 154 MJ, the repetition frequency is 10 Hz, and in the MIBICF reactor, the chamber radius is 3 m, the shot energy is 3 GJ, the repetition frequency is 1 Hz. Neutrons, which account for about 70% of the fusion reaction power, are incident on the reactor wall in both a laser and a MIBICF system, but the energy deposited to the reactor wall is relatively small compared with charged particle, neutral and X-ray because of the long range of the neutrons.

The main energy depositor to the surface of the reactor wall is X-rays, which account for about 25% of the total power. α-particles are mainly used to heat the fuel, but a part of these that escapes from the fuel or is decreased energy by giving to the fuel, was irradiated to the reactor wall. Heavy ions of 5% were irradiated to the reactor wall as D, T as fuel, Bi by using a driver, and Pb as a candidate material for tamper, and so on.

These loads occur in an extremely short time (ns - μs) and the reactor wall is exposed to extremely high heat loads. Therefore, any material is instantly evaporated and ablated. Therefore, as in laser fusion, a liquid metal is used to absorb the energy applied to the surface. So, the damage to the reactor wall due to the high heat load can be negligible virtually. On the other hand, provision is required for ablation at the tip of the beam port, and neutral metal vapor evaporates from the liquid reactor wall.

In magnetic confinement fusion, a part of the solid wall so called dry wall e.g. divertor was also evaporated and ablated due to the heat load of plasmas. For this reason, a detached divertor is employed, in which a gas (e.g., hydrogen or argon) is injected into

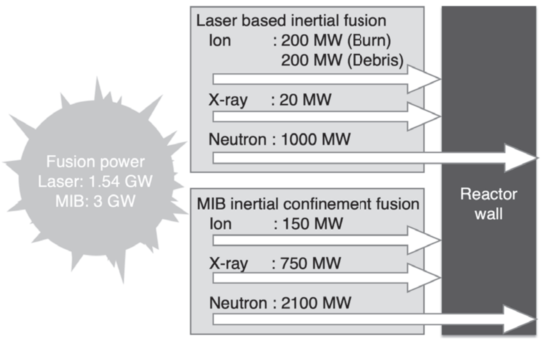

Fig. 2 Energy balance in laser based inertial fusion and MIBICF. Where the parameter of laser fusion was referred to HiPER reactor with 6.5 m of chamber radius, 154 MJ of energy per a shot, and 10 Hz of repetition frequency[7]. The parameter of MIBICF was assumed to 3 m of chamber radius, 3 GJ of energy per a shot, and 1 Hz of repetition frequency.

the divertor region to release the thermal energy of the plasma. On the other hand, in the inertial confinement, it is permitted to ablate the reactor wall, so there is no need to reduce the inflow energy in front of the wall. The different point between the laser fusion system and the MIB fusion system is the pressure inside the chamber. The pressure is required less than 100 Pa [8] in the laser fusion system, while 0.01~0.1 Pa [9] in the MIB system.

3. Reactor wall

3.1 Liquid wall

LiPb liquid wall was adopted as the plasma facing material in the MIB system. A free-fall LiPb was flowed along the reactor wall and circulated it. If a single surface flow is used from the top to the bottom of the reactor, the LiPb experiences multiple shots before it falls and the temperature increases. To solve this problem, a cascade method, the LiPb liquid metal is poured into a module with a bucket-like structure, and another module receives the overflow LiPb from the poured module, has been devised [10].

The reactor can be operated repeatedly at high pulse heat loads because the liquid wall are recovered by recondensation at the liquid surface and flow even if damaged by ablation. Therefore, some issues can be overcame for the solid wall including wear damage by ablation and sputtering, creating cracks and changing texture by heat load, generating bubbles and fuzzy nanostructure (fuzz) by gas ion, displacement damages, swelling, etc.[11]. There is no need to consider neutron irradiation damage with respect to the breeder material, because it is a liquid, and it is possible to continuously recover tritium and adjust its composition during operation. So, it is possible to produce more tritium fuel than the amount consumed in the core plasma by the neutron multiplication effect of the (n,2n) reaction of Pb.

3.2 Solid wall (dry wall)

It is difficult to cover the ceiling of the reactor chamber with a liquid wall since free fall of liquid metal is used. Provisions have been proposed to increase the distance between the ceiling and the fuel, and condense LiPb vapor by making the solid wall cooler [11]. Similarly, the surface of the beam port, which is installed protruding from the wall, is exposed from the liquid wall. Applying a magnetic field is considered to protect the beam port from charged particles. The effect of irradiation to the components where it is difficult to protect by liquid wall can be reduced to use SiC/SiC structural materials or tungsten. SiC has the following characteristics: low Z material, high melting point (~2000K), and resistance to degradation by neutrons (thermal conductivity and mechanical strength are not reduced) [12].

4. Summary

The energy balance of the DEMO (magnetic confinement fusion), the HiPER (inertial confinement fusion) and the MIBICF reactor were compared. Unlike magnetic confinement fusion, inertial confinement fusion requires the use of a liquid wall because fusion power is generated in an extremely short period of time. However, a large heat load is expected to be applied to the solids at the ceiling and beam ports, where it is difficult to cover with liquid. The knowledge of solid walls obtained in magnetic confinement fusion study may be applied to the MIBICF reactor.

References

[1] K. Takayama, *et al*., "A massive-ion beam driver for high-energy-density physics and future inertial fusion", *Phys. Rev. A* **384** 126692 (2020).

[2] S. Konishi, *et al*. "DEMO plant design beyond ITER" *Fusion Eng. Des.* **63** 11-17 (2002).

[3] S. Suzuki, *et al.*, "Plasma-Facing High-Heat-Flux Components: Walls to Withstand High Heat Flux from Fusion Plasmas" (in Japanese), *Journal of Atomic Energy Sciety of Japan* **47** 266–271 (2005).

[4] D. Garoz, *et al.*, "Modelling the thermomechanical behaviour of the tungsten first wall in HiPER laser fusion scenarios", *Nucl. Fusion* **56** 126014 (2016).

[5] S. Pestchanyi, "Simulation of Heat Flux to the DEMO First Wall Due to Filamentary Transport in the Far SOL", *IEEE Trans. Plasma Sci.* **46** 1393–1397, (2018).

[6] A. Nishimura, "Several Considerations on Construction

Site of Fusion DEMO", *Plasma Fusion Res.* **13** 3405023 (2018).

[7] Y. Ueda, *et al.*, "PSI issues at plasma facing surfaces of blankets in fusion reactors", *J. Nucl. Mater.* **313–316**, 32–41 (2003).

[8] W.R. MEIER, "Fusion technology aspects of laser inertial fusion energy (LIFE) ", *Fusion Eng. Design* **89** 2489–2492 (2014).

[9] T. Kikuchi, *et al.*, "*Study on Reactor Radius of Heavy-Ion Inertial Fusion*", *NIFS-PROC*, In Press.

[10] Y. Kozaki, *et al.,* "Conceptual design of the Fast Ignition Laser Fusion Power Plant (KOYO-Fast)" (in Japanese), *J. Plasma Fusion Res.* 82, 817-835 (2006).

[11] T. Norimatsu, *et al.*,"Conceptual Design and Issues of the Laser Inertial Fusion Test (LIFT) Reactor – Targets and Chamber Systems", *Nucl. Fusion* **57**, 116040 (2017).

[12] K. Katoh, "Status and Prospects of SiC-Based Ceramic Composites for Fusion and Advanced Fission Applications" (in Japanese), *J. Plasma Fusion Res.* **80**, 18-23(2004).

Kinetic Energy Distribution of Fuel Pellet Materials After Ignition for Heavy–Ion Inertial Fusion Reactor

Takashi Kikuchi

Nagaoka University of Technology

ABSTRACT

Expansion dynamics of a fuel pellet after ignition in a reactor chamber was investigated for a direct–drive fuel target in heavy–ion inertial fusion (HIF). During the expansion process, the state of the fuel target changed from a fluid system to a free–molecular flow. The behavior of the target materials as a free–molecular flow was analyzed using results obtained from fluid model calculations. As a result, the kinetic energy distributions of ions occurred from the fuel pellet were calculated as a single particle motion for the free–molecular flow. The kinetic energy distributions for each ion species were compared with the results in references for a direct–drive laser fusion fuel target and an indirect–driven HIF fuel target.

Keywords

Heavy–Ion Inertial Fusion, Fuel Pellet Material, Expansion Dynamics, Knudsen Number, Fluid System, Free–Molecular Flow, Kinetic Energy

1 Introduction

After a fuel pellet in the center of a reactor chamber is ignited by irradiation of heavy–ion beams, a Deuterium (D) and Tritium (T) mixed fuel is expected to be burned in a target implosion process for a heavy–ion inertial fusion (HIF) scheme [1, 2]. The explosion wave pushes the fuel and structural materials of the target pellet, and impacts the inner wall of reactor chamber. These are absorbed in the reactor wall, and the generated heat is converted into electrical energy using a power generation system.

The output energy from the fuel pellet is released as neutrons and alpha particles generated by the DT reactions, X–rays and fast ions produced as the burn products propagate outward. For this reason, the radiations are also a damage factor impacting the reactor wall, and the estimation is key issue to design the HIF reactor. As a result, the expansion dynamics of the fuel pellet after the ignition in a reactor chamber should be studied for the HIF power generation plant.

In this study, the expansion dynamics of the fuel pellet after the ignition was investigated in a reactor chamber for a direct–drive HIF fuel target. During the expansion process, the state of the fuel target changes from fluid to free–molecular flow. Because not only the numerical model but also the physical model changes, it is important to find the points of change. The changing point is evaluated by the Knudsen number. The behavior of the target materials as a free–molecular flow is analyzed using information obtained from fluid model calculations. As a result, the kinetic energy distribution of ions occurred from the fuel pellet are calculated as a single particle motion for the free–molecular flow. The obtained kinetic energy distribution for each ion species in the direct–drive HIF fuel target was compared with information in references for a direct–drive laser fusion fuel target and an indirect–driven HIF fuel target.

2 Calculation Method

We developed a numerical calculation code, which is based on a one–dimensional Lagrangian fluid system in spherical coordinate as follows [3].

$$\frac{dM}{dt} = 0, \quad (1)$$

$$\frac{D\,u}{Dt} = -\frac{1}{\rho}\frac{\partial P + q}{\partial\,r}, \quad (2)$$

$$\rho\,c_v\frac{DT}{Dt} = -\frac{P+q}{r^2}\frac{\partial\,r^2u}{\partial\,r} + \frac{1}{r^2}\frac{\partial}{\partial\,r}\left(r^2\kappa\frac{\partial\,T}{\partial\,r}\right), \quad (3)$$

$$P = \frac{k_B}{m}\rho T, \quad (4)$$

where M is the mass at each cell, u is the radial velocity of fluid, ρ is the mass density, P is the pressure, q is the artificial viscosity, c_v is the specific heat, T is the temperature, κ is the thermal conductivity, k_B is the Boltzmann constant, and $D/D\,t = \partial/\partial\,t + u\;\partial/\partial\,r$ is the Lagrangian derivative, respectively. The above mass conservation (continuous) equation, momentum (Navier–Stokes) equation, energy (temperature) equation with thermal conduction, and ideal gas equation–of–state were numerically solved according to the initial condition as shown in Table 1 [4]. The composition ratio of LiPb is 95 % for Li and 5 % for Pb.

Table 1: Initial condition at each fuel pellet material for expansion phase in direct–drive HIF fuel target [4].

Layer	Species	Region [mm]	Density [g/cc]	Temperature [K]
Fuel	DT	0∼0.161	243	2.0×10^9
Pusher	LiPb	0.161∼0.218	243	1.0×10^8
Ablator	LiPb	0.218∼3.45	0.35	2.0×10^7
Tamper	Pb	3.45∼5.29	0.57	1.5×10^6

The role of layer, material species, region width, density, and temperature at the stagnation phase were for a direct–drive HIF fuel target [4].

The outer region (background gas in the chamber) of the fuel pellet was assumed as the temperature of 1500 K and the pressure of 0.1 Pa [5].

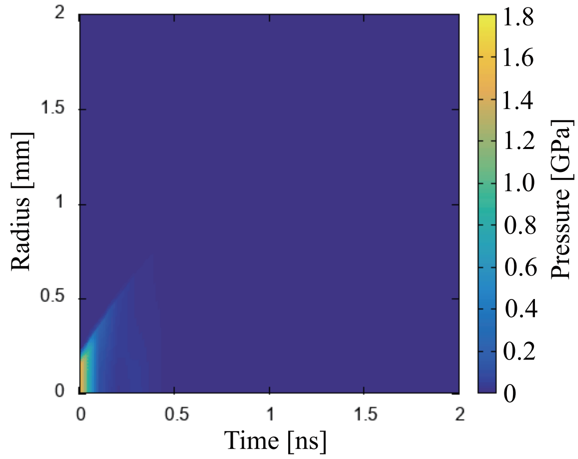

Figure 1: History of pressure distribution in expansion phase after ignition.

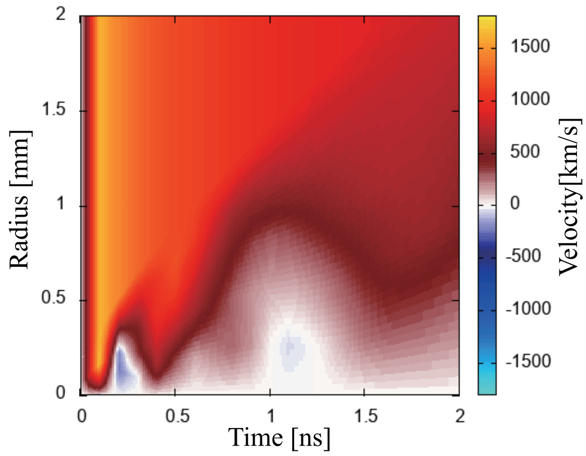

Figure 2: History of velocity distribution in expansion phase after ignition.

3 Calculation Result

Figures 1 and 2 show the histories of the pressure and the velocity for the fuel pellet during the expansion after the implosion and ignition by obtaining the numerical simulation, respectively. At the initial condition, the fuel density and temperature have extremely high values due to the implosion process and the nuclear fusion reactions. For this reason, the fuel layer was rapidly expanded toward the chamber wall due to the high pressure around the center as shown in Fig. 1. The fuel velocity outward from the center of the target became high due to the extremely high pressure near the center. However the temperature of the outer layer of the

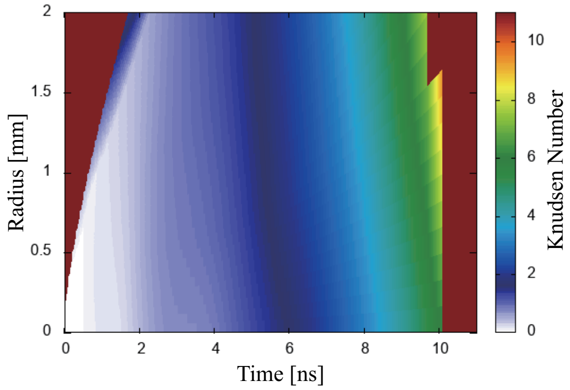

Figure 3: Knudsen number in expansion phase after ignition.

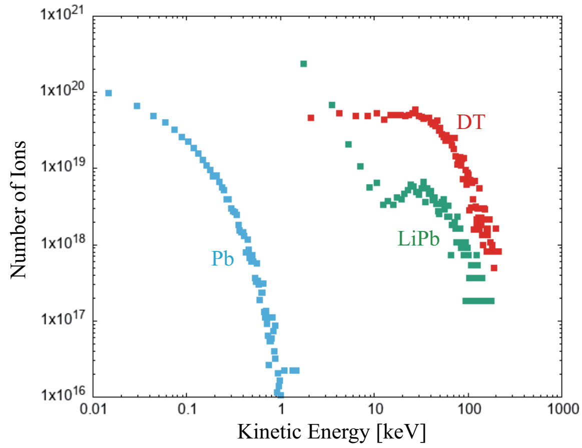

Figure 4: Numbers of DT, LiPb, and Pb as a function of kinetic energy at 15 ns after ignition.

fuel target was lower than that near the center of the fuel, and the tamper was composed of heavy ion Pb. As a result, the expansion velocity for the outer layer was slower than that near the center of the target. Consequently, the expansion of the fuel layer was reflected by the tamper as shown in Fig. 2.

Figure 3 shows the history of the Knudsen number for the fuel pellet during the expansion after the implosion and ignition. The Knudsen number was evaluated with the parameters obtained by the numerical simulation. The Knudsen number Kn, which was defined by the ratio of the mean free path and the characteristic length [6], was evaluated at each calculation cell by

$$Kn = \frac{k_B T}{\sqrt{2}\,\sigma\, PL}, \tag{5}$$

where σ is the cross–section $(= 10^{-25}\ \mathrm{m}^2)$ of the particle and L is the characteristic length, respectively. In this study, the characteristic length L was defined by the each cell size at each time, because the cell size was automatically rearranged at each time step in the Lagrangian system. As a result, it was evaluated that the Knudsen number exceeded unity after 2 ns for the entire fuel pellet [3]. In the history of Knudsen number during the expansion, it was implied that the fuel pellet material changed to transitional flow after 2 ns. When $Kn \geq 10$, the material state was expected as a free molecular flow. We considered that the state of fuel pellet material was changed to the free molecular flow after 10 ns in the entire region.

The macro–particles, which were representative particle including some ions, were generated at each calculation cell when the Knudsen number exceeded 10. The calculation results of fluid system were applied to the macro–particle generation. The macro–particle had the velocity based on the Maxwell distribution according with the temperature at each calculation cell given by the calculation result of fluid system. Figure 4 shows the numbers of DT, LiPb, and Pb as a function of kinetic energy at 15 ns after ignition. The fuel DT ions had the kinetic energy in range of 2 $\sim$ 200 keV, and the main kinetic energy was expected as several–ten keV. The ablator and pusher LiPb ions also had the kinetic energy in range of 2 $\sim$ 200 keV, while the number of ions was smaller than that for DT ions. The kinetic energy of tamper Pb ions was expected as less than 1 keV, and the main kinetic energy was expected as less than 0.1 keV. From the viewpoint of the kinetic energy and the number of ions, it was considered that the fuel DT ions are most effective particles for the wall damage of the reactor chamber.

Figure 5 shows the kinetic energy of ions as a function of radius at 15 ns after ignition at each species. The fuel DT ions traveled the furthest toward the reactor wall compared to LiPb and Pb ions, because the fuel DT ion has the lighter mass with the higher kinetic energy. On the other hand, the tamper Pb ions were at almost original position, because of the heavier mass with the lower kinetic energy. It was indicated that the arrival time at the chamber wall was different for each ion species.

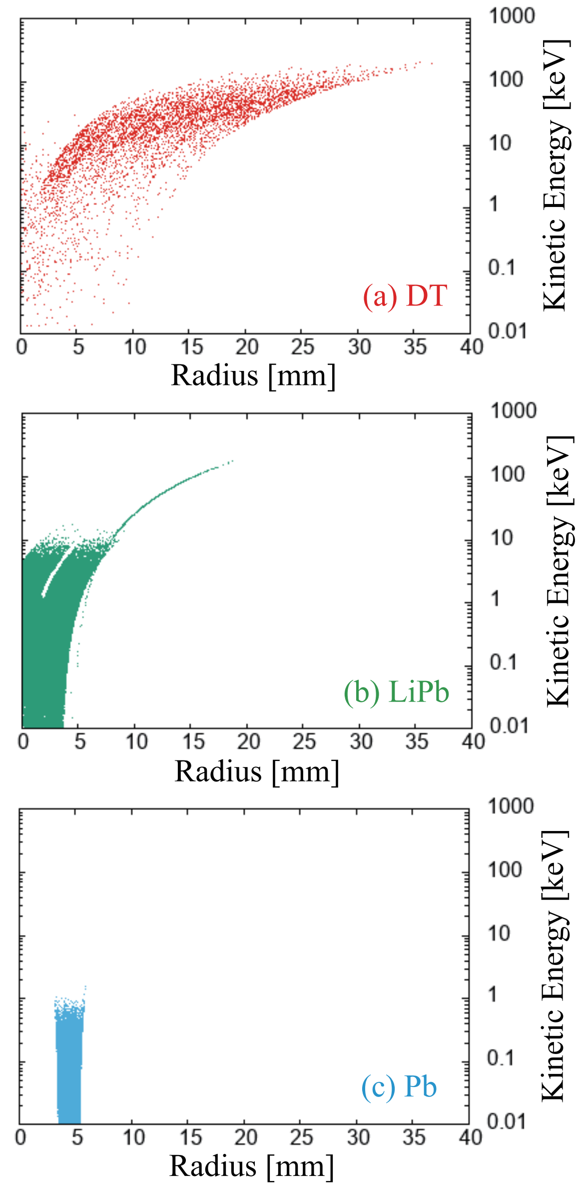

Figure 5: Kinetic energy of ions as a function of radius at 15 ns after ignition, (a) for DT, (b) for LiPb, and (c) for Pb, respectively.

4 Discussion

In the direct–drive laser fusion target, the debris ion spectra indicated that the DT ions had the kinetic energy of 1 $\sim$ 700 keV, and the number of ions was largest at the kinetic energy of 100 keV [7, 8]. The heavier (Au) ions had the kinetic energy of several–10 MeV, while the number of ions was small [7,8]. The ion species depended on the target structural material, while it was considered that the ion spectra depended on the target structure related to the energy driver from the viewpoint of comparison to the results obtained by Fig. 4 (for the direct–drive HIF target).

In the indirect–driven HIF target, the debris ion spectra indicated that the DT ions had the kinetic energy of 1 $\sim$ 10 keV, and the number of ions was larger with the low kinetic energy [9]. The heavier ions such as Gd and Au had the kinetic energy of 80 $\sim$ 700 keV [9]. The ion species depended on the target structural material, while it was considered that the ion spectra depended on the target structure related with the beam illumination scheme from the viewpoint of comparison to the results obtained by Fig. 4 (for the direct–drive HIF target).

Consequently, it was found that the ion species and the kinetic energy should be evaluated by the detailed calculation at each target design. It was implied that the fusion output load to the chamber wall depended on the fuel pellet structure.

5 Conclusion

The expansion dynamics of fuel pellet after the ignition in the reactor chamber was investigated for the direct–drive HIF fuel target. The state of the fuel target changed from a fluid approximation model to a free–molecular flow model during the expansion process. The behavior of the target materials as the free–molecular flow was analyzed using results obtained from the fluid model calculation. As a result, the kinetic energy distributions of ions occurred from the fuel pellet were calculated as the single particle motion for the free–

molecular flow. It was indicated that the arrival time at the chamber wall was different for each ion species. The kinetic energy distributions for each ion species were compared with the results in references for a direct–drive laser fusion fuel target and an indirect–driven HIF fuel target. Consequently, it was found that the ion species and the kinetic energy should be evaluated by the detailed calculation at each target design. It was implied that the fusion output load to the chamber wall depended on the fuel pellet structure.

In this study, the radiation generation and transport were ignored in the numerical simulation. However the ratio of X ray energy (25 %) in the indirect–driven HIF target was lager than that (1.4 %) for the direct–drive target [9]. Consequently, the generation of X ray should be considered in the HIF target.

Acknowledgment

The author would like to thank the committee member of "Design Committee for Novel Heavy–Ion Inertial Fusion System of Japan" for the useful discussions.

References

[1] S. ATZENI and J. MEYER-TER-VEHN, *The Physics of Inertial Fusion: Beam Plasma Interaction, Hydrodynamics, Hot Dense Matter* (Oxford Univ., N.Y., 2004).

[2] S. PFALZNER, *An Introduction to Inertial Confinement Fusion (Series in Plasma Physics)* (CRC Press, 2006).

[3] W. HOU, K. TAKAHASHI, T. SASAKI, T. KIKUCHI, *Proc. 42nd JSST Annual International Conference on Simulation Technology (JSST2023)*, P12 (2023).

[4] B. BADGER, *HIBALL—A Conceptual Heavy Ion Beam Driven Fusion Reactor Study*, KfK 3202 and UWFDM-450 (1981).

[5] T. KIKUCHI, K. TAKAHASHI, T. SASAKI, and M. KOGA, *to be published in NIFS-PROC.*

[6] A.S. RICHARDSON, *NRL Plasma Formulary* Supported by The Office of Naval Research, (Naval Research Laboratory, Washington, DC, 2019).

[7] A.R. RAFFRAY, L. EL-GUEBALY, G. FEDERICI, D. HAYNES, F. NAJMABADI, D. PETTI, and ARIES-IFE TEAM, *Fusion Sci. Tech.* **46**, pp.417∼437 (2004).

[8] A.R. RAFFRAY and THE HAPL TEAM, *J. Nuclear Materials* **347**, pp.178∼191 (2005).

[9] A.R. RAFFRAY, S.I. ABDEL-KHALIK, D. HAYNES, F. NAJMABADI, P. SHARPE, M. YODA, M. ZAGHLOUL, and ARIES-IFE TEAM, *Fusion Sci. Tech.* **46**, pp.438∼450 (2004).

Study of Reactor Radius Based on Beam Transport Criteria

Takashi Kikuchi

Nagaoka University of Technology

ABSTRACT

A reactor radius for a heavy–ion inertial fusion system was discussed from viewpoint of a vacuum system. The gas pressure in the reactor is limited by an allowable level of heavy–ion beam transport condition to a fuel target. The gas pressure in the reactor increases by contaminations generated due to nuclear fusion reactions and hydrogen isotopes as a residual fuel. For this reason, the gas pressure is needed to decrease to the allowable level of heavy–ion beam transport condition to the target using a vacuum pump. The pumping speed depended on the reactor radius, and the reactor radius was determined by the reasonable pumping speed.

Keywords

Reactor Chamber, Reactor Radius, Pumping Speed, Heavy–Ion Beam Transport, Residual Gas Pressure

1 Introduction

The fuel pellet is placed in the reactor chamber of heavy–ion inertial fusion (HIF), and is illuminated by the heavy-ion beams. The reactor has various functions such as the recovery of nuclear fusion output, beam transport environment, radiation shielding, tritium breeding, remnant gas exhaust, collection of pellet structural material, and so on [1]. For this reason, the radius of reactor chamber is limited to the various components and factors as follows:

- First wall: the nuclear fusion output deposits to the inner wall of reactor. For the liquid wall, the surface of liquid wall is ablated due to the fusion output. The liquid thickness should be evaluated due to the ablation. For the solid wall, the surface of solid wall should be protected from the fatal damage such as crack and blister formations. The irradiation effect of fusion output at the wall depends on the fluence and the flux. The fluence and the flux are determined by the inner surface area of the reactor. For this reason, the reactor radius is related to the first wall problem.
- Vacuum vessel: the various reactor structures were designed, and are categorized by the spherical or the cylindrical configurations as shown in Figs. 1 and 2, which are designs of the Laser Fusion Experimental Reactor LIFT [2]. The vacuum vessel should be resisted from the load of nuclear fusion output at each shot. The vacuum vessel stiffness is determined by the reactor size, configuration, structural material, and so on. Consequently the reactor radius is important parameter from the viewpoint of the chamber stiffness because the smaller radius of reactor chamber causes the serious stress to the vacuum vessel.
- Target injection: the fuel pellet should be precisely injected into the reactor, and should be placed at the designated position in the chamber at each shot. It is difficult to control precisely the target pellet track in the longer transport distance with the higher pressure of background gas. For this reason, the ra-

dius of reactor chamber is one of factors for the target pellet injection.

- Beam transport: heavy–ion beams are injected into the reactor chamber, and are focusing to the fuel pellet. During this process, the heavy–ion beams should be transported in the reactor without the beam loss. One of factors for the beam loss is collision between the beam ion and the background gas particle in the chamber. The radius of reactor is a key issue because the beam loss is proportional to the transport distance.

- Power generation equipment: the working fluid is operated as coolant to recovery the nuclear fusion output energy. The higher temperature of working fluid is suitable for higher conversion efficiency from the thermal energy to the electrical energy. The temperature of working fluid increases due to the absorption of nuclear fusion output, and it is depends on the energy density of nuclear fusion output at the reactor wall. Consequently the temperature of working fluid depends on the reactor radius, and also the thermal efficiency of the power plant is determined by the radius of reactor.

- Engineering safety equipment: the neutron flux generated by the nuclear fusion reactions produces the radio–activation in the material of reactor wall. The neutron flux and fluence at the inner wall depends on the reactor radius. The smaller radius of reactor causes the higher activation due to the higher fluence and flux of neutron. The radius of the reactor is important from the viewpoint of radio–activation, because dense activation area determines the lifetime of the reactor.

- Electromagnet protection: the nuclear fusion output damages the electromagnets for the final beam focusing to the fuel pellet. The electromagnets are placed at near reactor outside. For this reason, the radiation shield is crucial issue. Especially the neutron shield is achieved by the long distance between the electromagnet and the output source (fuel pellet). Consequently the radius of reactor chamber is related to the electromagnet protection.

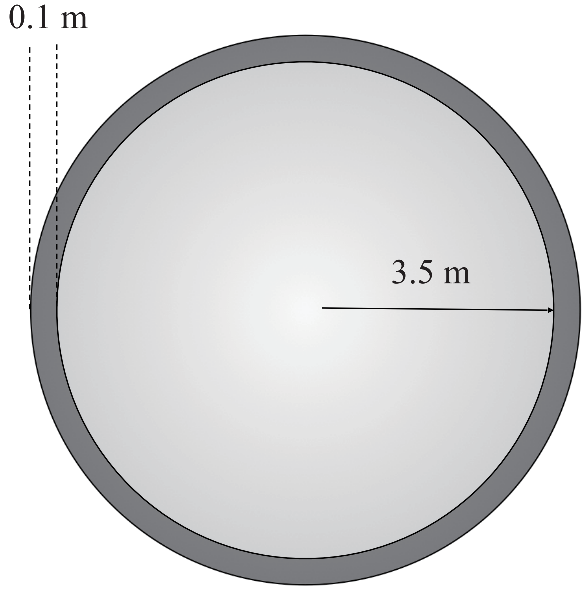

Figure 1: Schematic diagram of reactor for LIFT–II [2]. The structure type is a spherical configuration of the radius of 3.5 m with the wall thickness of 0.1 m. The chamber volume is given by $4\pi(3.5)^3/3 = 180$ m^3, and the mass of chamber is estimated by 1.25×10^5 kg for the mass density of 7.87×10^3 kg/m^3 (Stainless Steel).

- Vacuum system: the volume of the reactor chamber is limited by the pumping speed and the ultimate vacuum level. The cases for the larger reactor chamber size and the higher ultimate vacuum level (lower gas pressure in the reactor chamber) require the larger exhaust speed of the vacuum pump. Consequently the radius of reactor chamber is related to the vacuum system.

As a result, the radius of reactor chamber is the most important parameter to construct the HIF power plant system.

2 Gas Pressure in Reactor Limited by Beam Transport Condition

The gas pressure in the reactor is limited by the allowable level of heavy–ion beam transport to a

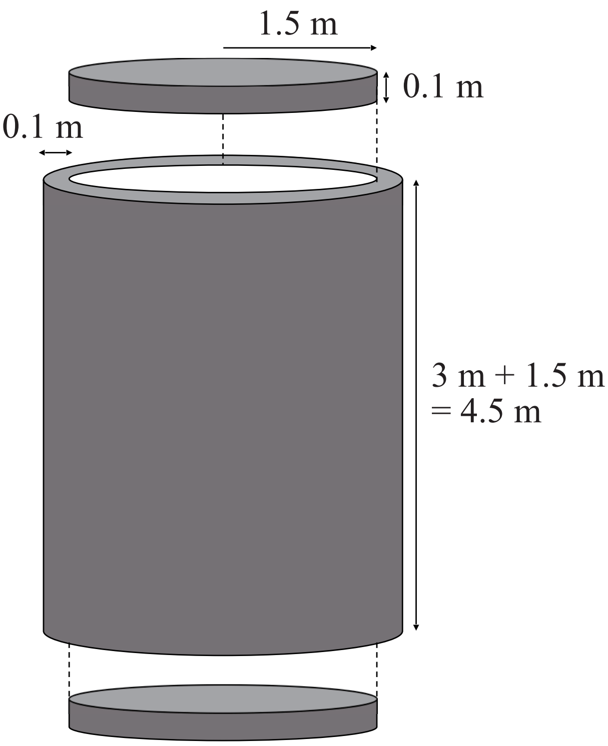

Figure 2: Schematic diagram of reactor for LIFT–III [2]. The structure type is a cylindrical configuration of the radius of 1.5 m with the wall thickness of 0.1 m and the height of 4.5 m. The chamber volume is given by $\pi(1.5)^2 \times 4.5 = 31.8$ m^3, and the mass of chamber is estimated by 4.56×10^4 kg for the mass density of 7.87×10^3 kg/m^3 (Stainless Steel).

fuel target. On the other hand, the gas pressure in the reactor increases by contaminations generated due to nuclear fusion reactions and hydrogen isotopes as a residual fuel. Consequently, the gas pressure should be decreased to the allowable level of heavy–ion beam transport to the target using a vacuum pump.

In the reactor design for laser driven inertial confinement fusion (ICF), the gas pressure is required less than 100 Pa [3], and is required by 1 Pa for fast ignition scheme [2]. In the case of HIF reactor, the gas pressure is determined by the modes of heavy–ion beam propagation in the reactor chamber [4]. The mode of vacuum transport (ballistic transport) is assumed in this design, because of avoiding the various instabilities for heavy–ion beam propagation through the gas environment. Therefore the gas pressure is required in ranges of 0.01∼0.1 Pa [5] for the case of HIF.

For this reason, the pumping speed and the ultimate vacuum are unique parameters for HIF system in comparisons with the laser driven ICF system. The pressure requirement in the reactor chamber and the pumping speed determine the reactor radius for the HIF system.

3 Relation between Reactor Radius and Pumping Speed

The allowable gas pressure in the reactor is estimated due to the limitation by the collisional ionization of the beam ion in the heavy–ion beam transport [4]. The allowable gas pressure for the heavy–ion beam transport is written by

$$P_t = \frac{1}{\sigma R} k_B T, \tag{1}$$

where σ is the collisional ionization cross section (e.g., 7×10^{-20} m^2 for Pb [4]), R is the reactor radius (standoff), k_B is the Boltzmann constant, and T is the gas temperature (300 K), in the case of strong stripping ($n\sigma R = 1$ where n is the number of density for gas). In this HIF reactor, it has been proposed to protect the reactor wall by flowing liquid metal LiPb. The heavy–ion beam transport was estimated by the collisions between the beam ion and Pb, because Pb has the largest collisional cross section.

The gas pressure in the reactor increase after the fuel pellet implosion, because the DT nuclear reaction creates He and the residual fuel (DT) diffuses in the reactor chamber. Li and Pb contained in the liquid metal re-adhere mainly to the liquid metal for protection of the reactor wall. For this reason, the main work of the vacuum pump is to pump out He and residual fuel (DT) gases. The increase of gas pressure is estimated by

$$P_f = \frac{3N_f}{4\pi R^3} k_B T, \tag{2}$$

where N_f is the number of diffused gas particles (D, T, and He) per shot and $V_R = 4\pi R^3/3$ is the reactor volume. In this study, the number of gas particles (D, T, and He) per shot was assumed by 3.3×10^{22} for the burn fraction of 0.3 [1] and the fusion output of 2 GJ per shot [6].

The pumping (exhaust) speed S for a vacuum pump is estimated by

$$S = -\frac{V_R \Delta P}{P \Delta t}, \qquad (3)$$

where the pressure difference $\Delta P = P_b - P_a$ and the time interval Δt for shot–by–shot. Here P_b and P_a indicate the gas pressure before and after the shot. In this study, the gas pressure P_b before the shot is assumed by the allowable gas pressure P_t for the heavy–ion beam transport ($P_b = P_t$). For this reason, the gas pressure P_a after the shot is increased from P_b by the pressure increase P_f due to the gas particles (D, T, and He), and is written by

$$P_a = P_b + \frac{3N_f}{4\pi R^3} k_B T, \qquad (4)$$

and $P = (P_a + P_b)/2$ is roughly evaluated in this study. Consequently, the pumping speed is calculated by

$$S = \frac{8\pi\sigma N_f R^3}{8\pi R^2 + 3\,\sigma N_f} \frac{1}{\Delta t}, \qquad (5)$$

where σ is assumed by 7×10^{-20} m^2 for Pb [4], 2×10^{-21} m^2 for Li [4], and 2.5×10^{-21} m^2 for He [7], respectively.

The required pumping speed per reactor can be reduced using multi reactor design. In the case of 10 reactors, the required pumping speed is decreased by 10 at each reactor.

The pumping speed of 10 m^3/s is assumed as the design parameter in case of KOYO-F [2]. The pumping speed up to 6.2 m^3/s is required by the HYLIFE-II [5]. For this reason, the reactor radius of $3 \sim 5$ m is suitable for the HIF system with 10 reactors [8].

4 Conclusion

The reactor radius was discussed from the viewpoint of vacuum system in the reactor. The gas pressure in the reactor was limited by the allowable level of heavy–ion beam transport condition to the fuel target, and increased by the contaminations generated due to the nuclear fusion reactions and the hydrogen isotopes as the residual fuel. The gas pressure should be decreased to the allowable level of heavy–ion beam transport to the target using the vacuum pump. For this reason, the reactor radius was determined by the reasonable pumping speed.

The pumping speed was estimated as a function of reactor radius [8]. The vapor pressure for LiPb is 0.01∼0.1 Pa [9]. The radius of 10 m is one of limitation for the reactor radius from the viewpoint of vapor pressure for LiPb [8]. Consequently, it was found that the reactor radius of 5 m is suitable for the HIF system on 1 Hz operation [6] with 10 reactors from the viewpoint of vacuum system.

Acknowledgment

The author would like to thank the Working Group 2 members (Prof. Kazuhiko HORIOKA, Prof. Yoshihiro KAJIMURA, Dr. Makoto NAKAMURA, and Prof. Yuki UCHIDA) and the committee member of "Design Committee for Novel Heavy–Ion Inertial Fusion System of Japan" for the useful discussions.

References

[1] S. PFALZNER, *An Introduction to Inertial Confinement Fusion (Series in Plasma Physics)* (CRC Press, 2006).

[2] *Conceptual Design for Fast Ignition Laser Fusion Power Plant*, (ILE, Osaka Univ. and IFE Forum, 2006) (in Japanese).

[3] W.R. MEIER, *Fusion Eng. Design* **89**, pp.2489∼2492 (2014).

[4] A.B. LANGDON, *Particle Accelerators* **37-38**, pp.175∼180 (1992).

[5] R.W. MOIR, *Fusion Tech.* **25**, pp.5∼25 (1994).

[6] K. TAKAYAMA, T. ADACHI, T. KAWAKUBO, K. OKAMURA, Y. YURI, J. HASEGAWA, K. HORIOKA, T. KIKUCHI, T. SASAKI, K. TAKAHASHI, *Phys. Lett.* **A384**, pp.126692-1∼126692-11 (2020).

[7] J. HASEGAWA, *private communication*

[8] T. KIKUCHI, Y. UCHIDA, M. NAKAMURA, Y. KAJIMURA, and K. HORIOKA, *NIFS–PROC* **123**, pp.85∼89 (2023).

[9] D. MARTELLI, A. VENTURINI, and M. UTILI, *Fusion Eng. Design* **138**, pp.183∼195 (2019).

Study on Target Injection Velocity into Reactor for Heavy–ion Inertial Fusion

Takashi Kikuchi

Nagaoka University of Technology

ABSTRACT

An estimation model of required injection velocity was investigated from the viewpoint of melting of solid fuel and heat conduction during a reactor chamber. The estimation showed that the fuel target for heavy–ion inertial fusion requires lower injection velocity, and has an advantage for an operation of power plant system.

Keywords

Heavy–Ion Inertial Fusion, Fuel Pellet Injection, Injection Velocity, Reactor Chamber, Thermal Conduction Equation

1 Introduction

A fuel target for heavy–ion inertial fusion (HIF) consists of solid–state deuterium (D) and tritium (T) as a fuel for nuclear fusion reactions and other structural materials. The fuel pellet is repeatedly injected into the reactor chamber with several Hz, and is illuminated by several intense heavy–ion beams. Therefore, the position of fuel pellet should be controlled accurately at the designated one at each shot [1–3]. However, it is difficult to control the injection into the designated position in the reactor at each shot with higher injection velocity.

The fuel pellet is heated by the thermal conduction from the background gas in the reactor chamber. The lower injection velocity of the fuel pellet causes the melting of solid fuel, because the long time flight with the lower injection velocity gives the time for melting the low–temperature solid fuel.

It is expected that the heat conduction in the fuel pellet depends on the several factors such as the gas temperature in the reactor chamber, the fuel pellet structure, the structural material of fuel pellet, and so on. From the viewpoint of the melting of the solid DT fuel, the injection velocity was investigated in this study with the several conditions.

2 Injection Velocity for Conventional Design in ICF reactor

This system assumes a fuel pellet with spherical symmetry or a sphere–like shape. Compared to laser fusion, especially a fuel pellet for fast ignition scheme such as KOYO–F, the target of this system is thought to have a relaxed condition from the standpoint of attitude control [4]. Furthermore, as the gas pressure inside the reactor is lower in the HIF system [5], it is assumed that the displacement of the fuel target due to the airflow of residual gas in the reactor is less. The methods using gas guns and electromagnetic acceleration are being considered in order to achieve an incident velocity of 100 m/s in laser fusion reactors [1].

The injection velocity of several 100 m/s is required due to the limitations of solid–state fuel melting due to heat conduction and radiant heat from residual gas in the reactor chamber when the fuel pellet passes through the reactor chamber [2, 3, 6–8]. In the HIBALL–II target delivery parameters, the target velocity of 200 m/s was used for sufficient to prevent detrimental heating of the target [6]. Schmatov et al. estimated the injection velocity for container-covered targets and targets with cone to be from 400 and 600 m/s [7]. Valmianski et al. estimated the injection velocity from 200 to 1000 m/s in the method to throw a screen in front of a fuel pellet [2]. Norimatsu et al. estimated the injection velocity of 200 m/s for central and fast ignition targets [3]. Tsuji assumed the injection velocity of 100 m/s with the reactor radius of 5 m [8].

3 Estimation Model of Required Injection Velocity due to Heat Conduction

In this system using the heavy–ion beams, the fuel pellet has a multilayer structure, and the fuel placed in the inner layer of the pellet is less susceptible to thermal effects from the reactor environment.

The thermal diffusion equation for temperature T in s layer was obtained by

$$\rho_s c_s \frac{\partial T}{\partial t} = \nabla \cdot (\kappa_s \nabla T), \tag{1}$$

where ρ is the density, c is the specific heat, κ is the thermal conductivity, respectively. The time–dependent one–dimensional thermal diffusion equation was rewritten by

$$\rho_s c_s \frac{\partial T}{\partial t} = \kappa_s \frac{\partial^2 T}{\partial x^2}. \tag{2}$$

Here the diffusion coefficient was defined by

$$D_s \equiv \frac{\kappa_s}{\rho_s c_s}. \tag{3}$$

The heat propagation velocity v_h in the fuel pellet was assumed by

$$v_h \sim \frac{D_s}{\Delta R_s}, \tag{4}$$

where ΔR_s is the thickness of s layer in the fuel pellet. For this reason, the heat propagation time τ in outer layer of the fuel pellet was estimated by

$$\tau = \frac{\Delta R_s}{v_h}. \tag{5}$$

As a result, the injection velocity v_{inj} was required by

$$v_{inj} = \frac{R_r}{\tau} = \frac{R_r v_h}{\Delta R_s} = \frac{R_r D_s}{(\Delta R_s)^2} = \frac{R_r \kappa_s}{\rho_s c_s (\Delta R_s)^2}, \tag{6}$$

where R_r is the reactor radius.

4 Estimation of Required Injection Velocity

As discussed in previous section, the required injection velocities were estimated in the fuel pellets for two conditions. The reactor radius was assumed by $R_r = 3$ m in this section. However, according to Eq. (6), the required injection velocity is simply proportional to the reactor radius. For this reason, the following estimations will be able to recalculate easily at each reactor radius.

The fuel pellet for LIFT consist of DT gas, DT solid (fuel), CH foam layers, respectively [9]. The CH layer thickness was $\Delta R_{\mathrm{CH}} = 27\mu$m. The physical properties of CH as a low density polyethylene were the thermal conductivity $\kappa_{\mathrm{CH}} = 0.33$ W/K-m, the specific heat $c_{\mathrm{CH}} = 2300$ J/kg-K, and the mass density $\rho_{\mathrm{CH}} = 910$ kg/m^3, respectively. Consequently, the required injection velocity was estimated by $v_{inj} = 648$ m/s for the LIFT design parameter.

On the other hand, the fuel pellet for HIF scheme was assumed in Fig. 1 of Ref. [10]. The fuel pellet consist of DT gas, DT solid (fuel), Al pusher, Al foam, Al ablator, and Pb tamper layers. The Al layer thickness was $\Delta R_{\mathrm{Al}} = 1.54$ mm. The physical properties of Al were the thermal conductivity $\kappa_{\mathrm{Al}} = 100$ W/K-m, the specific heat $c_{\mathrm{Al}} = 904$ J/kg-K, and the mass density $\rho_{\mathrm{Al}} = 2699$ kg/m^3, respectively. Consequently, the required injection velocity was estimated by $v_{inj} = 51.8$ m/s for the HIF fuel pellet design.

In the previous study [11], the temperature distribution history was calculated numerically using a thermal conduction equation for the fuel pellet heated by the background gas in the ICF reactor chamber. The injection velocity of 545 m/s was required for the reactor chamber radius of 3 m for the LIFT design parameter. It was estimated that the solid fuel will be not melted during 100 ms for the HIF fuel pellet design. For this reason, it was estimated that the injection velocity less than 30 m/s is required for the reactor chamber radius of 3 m for the HIF fuel pellet design. Consequently, the simple estimation in this study corresponded to the detailed results with the thermal conduction equation.

5 Conclusion

In this study, the estimation model of required injection velocity was investigated from the viewpoint of the melting of the solid DT fuel and the heat conduction. The estimations showed the required injection velocity $v_{inj} = 648$ m/s for the LIFT design parameter and $v_{inj} = 51.8$ m/s for the HIF fuel pellet design.

The target structure for the direct-driven HIF has the tamper and the foam layers owing to the stopping power of heavy-ion beams in the target material. For this reason, the lower injection velocity is required for the target pellet in HIF, because the heat conduction is interfered by the layers. This is one of advantages for the operation of ICF power plant in HIF system.

Acknowledgment

The author would like to thank Prof. Ryusuke TSUJI and Prof. Mayuko KOGA for useful information of injection velocity of target pellet.

References

[1] M. KOGA, S. UCHINO, E. MAEDA, K. YAMANOI, and A. IWAMOTO, *Plasma Fusion Res.* **17**, pp.2404052-1∼2404052-4 (2022).

[2] E.I. VALMIANSKI, R.W. PETZOLDT, and N.B. ALEXANDER, *Fusion Sci. Tech.* **43**, pp.334∼338 (2003).

[3] T. NORIMATSU, K. NAGAI, T. TAKEDA, K. MIMA, and T. YAMANAKA, *Fusion Sci. Tech.* **43**, pp.339∼345 (2003).

[4] *Conceptual Design for Fast Ignition Laser Fusion Power Plant*, p.64 (ILE, Osaka Univ. and IFE Forum, 2006) (in Japanese).

[5] T. KIKUCHI, Y. UCHIDA, M. NAKAMURA, Y. KAJIMURA, K. HORIOKA, *NIFS-PROC* **123**, pp.85∼89 (2023).

[6] B. BADGER et al., *HIBALL-II - An Improved Conceptual Heavy Ion. Beam Driven Fusion Reactor Study*, pp.25∼27 (UWFDM-625, also KfK-3840, FPA-84-4, 1984).

[7] M.L. SHMATOV, R.W. PETZOLDT, E.I. VALMIANSKI, *Fusion Sci. Tech.* **43**, pp.312∼320 (2003).

[8] R. TSUJI, *Plasma Fusion Res.* **14**, pp.3405164-1∼3405164-7 (2019).

[9] *Committee Report of Conceptual Design for Experimental Reactor of Laser Fusion with Fast Ignition*, p.48 (ILE, Osaka Univ. and IFE Forum, 2015) (in Japanese).

[10] N. WATANABE, K. TAKAHASHI, T. SASAKI, and T. KIKUCHI, *Plasma Fusion Res.* **17**, pp.2404086-1∼2404086-4 (2022).

[11] T. KIKUCHI, K. TAKAHASHI, T. SASAKI, and M. KOGA, *NIFS-PROC* **125**, pp.50∼55 (2023).

Publication List of NIFS-PROC. Series

NIFS-PROC-112 Edited by E. Kikutani (KEK) and S. Kubo (NIFS)
Proceedings of the meeting on Archives in Fields of Natural Sciences in FY 2017
Oct. 18, 2018 (Written in Japanses)

NIFS-PROC-113 Edited by Koichi Takaki and Tetsuo Ozaki
Pulsed Power and High-Density Plasma and its Applications
Feb. 6, 2019

NIFS-PROC-114 Edited by Daiji Kato, Ling Zhang, and Xiaobin Ding
The 7th Japan-China-Korea Joint Seminar on Atomic and Molecular Processes in Plasma (AMPP2018)
May 10, 2019

NIFS-PROC-115 CFQS Team
National Institute for Fusion Science, National Institutes of Natural Sciences
Institute of Fusion Science, School of Physical Science and Technology, Southwest Jiaotong University
Hefei Keye Electro Physical Equipment Manufacturing Co. Ltd.
NIFS-SWJTU JOINT PROJECT FOR CFQS -PHYSICS AND ENGINEERING DESIGN-
VER. 2.1 2019. SEP.
Nov. 8, 2019

NIFS-PROC-116 Satoshi Ohdachi, Editor of the Post-CUP Workshop proceeding
Collected papers at the 2019 Post-CUP Workshop & JSPS-CAS Bilateral Joint Research Projects Workshop,
24th-26th July, 2019, Nagoya, Japan
Feb. 21, 2020

NIFS-PROC-117 Edited by E. Kikutani (KEK) and S. Kubo (NIFS)
Proceedings of the meetings on Archives in Fields of Natural Sciences in FY2018
June. 9, 2020 (Written in Japanses)

NIFS-PROC-118 Edited by Tetsuo Ozaki and Sunao Katsuki
New Development of Beam Physics and the Application by New Generation Plused Power Technology
June. 29, 2020

NIFS-PROC-119 CFQS Team
National Institute for Fusion Science, National Institutes of Natural Sciences
Institute of Fusion Science, School of Physical Science and Technology, Southwest Jiaotong University
Hefei Keye Electro Physical Equipment Manufacturing Co. Ltd.
NIFS-SWJTU JOINT PROJECT FOR CFQS -PHYSICS AND ENGINEERING DESIGN-
VER. 3.1 2020. NOV.
Jan. 25, 2021

NIFS-PROC-120 Edited by Izumi Tsutsui (KEK) and Shin Kubo (NIFS)
Proceedings of the meetings on Archives in Fields of Natural Sciences in FY2019
Feb. 25, 2021

NIFS-PROC-121 Edited by Hiroaki Ito and Tetsuo Ozak
Frontier of Advanced Pulsed Power Technology and its Application to Plasma and Particle Beam
Nov. 08, 2021

NIFS-PROC-122 CFQS Team
National Institute for Fusion Science, National Institutes of Natural Sciences
Institute of Fusion Science, School of Physical Science and Technology, Southwest Jiaotong University
Hefei Keye Electro Physical Equipment Manufacturing Co. Ltd.
NIFS-SWJTU JOINT PROJECT FOR CFQS -PHYSICS AND ENGINEERING DESIGN-
VER. 4.1 2022. JAN.
Feb. 10, 2022

NIFS-PROC-123 Edited by Jun Hasegawa and Tetsuo Ozaki
Resent Developments of Pulsed Power Technology and Plasma Application Research
Feb. 5, 2023

NIFS-PROC-124 Edited by Weihua Jiang
Frontiers of Pulse Power Technology Development
Feb. 5, 2023

NIFS-PROC-125 Edited by Koichi Takaki and Tetsuo Ozaki
Recent trends in technologies of pulse power, high-density plasma and particle beams
July 1, 2023

NIFS-PROC-126 CFQS Team
National Institute for Fusion Science, National Institutes of Natural Sciences
Institute of Fusion Science, School of Physical Science and Technology, Southwest Jiaotong University
Hefei Keye Electro Physical Equipment Manufacturing Co. Ltd.
NIFS-SWJTU JOINT PROJECT FOR CFQS ~PHYSICS AND ENGINEERING DESIGN~
VER. 5.1 2023. AUG.
Feb. 8, 2024

NIFS-PROC-127 Edited by Jun Hasegawa and Tetsuo Ozaki
Conceptual Design of a Heavy Ion Inertial Fusion Reactor Based on Circular Induction Accelerators
May 29, 2024